Activation of NO/cGMP signaling as a potential therapy for metabolic dysfunction-associated steatotic liver disease

Dissertation

der Mathematisch-Naturwissenschaftlichen Fakultät

der Eberhard Karls Universität Tübingen

zur Erlangung des Grades eines

Doktors der Naturwissenschaften

(Dr. rer. nat)

vorgelegt von

Krithika Rajeeth

aus Vijayawada

Tübingen

2024

Gedruckt mit Genehmigung der Mathematisch-Naturwissenschaftlichen Fakultät der Eberhard Karls Universität Tübingen.

Tag der mündlichen Qualifikation:	19.03.2024
Dekan:	Prof. Dr. Thilo Stehle
1. Berichterstatter:	Prof. Dr. Robert Feil
2. Berichterstatter:	Prof. Dr. Andreas Friebe

Zusammenfassung

Eine der Hauptursachen für durch Lebererkrankungen verursachte Sterblichkeit ist die metabolische disfunktion-assozierte steatotische lebererkrankung (MASLD), die durch übermäßige Kalorienzufuhr in Verbindung mit einem bewegungsarmen Lebensstil verursacht werden kann. Die MASLD umfasst ein Spektrum chronischer Lebererkrankungen, das mit einer Fettleber beginnt und im Laufe der Zeit zu einer metabolische disfunktion-assozierte steatohepatitis (MASH), einer Zirrhose und schließlich zu einem hepatozellulären Karzinom fortschreitet. Das Fortschreiten von MASLD zu MASH beginnt mit der Anhäufung von Lipiden in der Leber (Steatose), gefolgt von der Aktivierung verschiedener leberansässiger Zellen, einschließlich der hepatischen Stellatzellen (HSC). Der Übergang der HSCs von einem ''ruhenden'' zu einem ''aktivierten'' Phänotyp ist ein Schlüsselfaktor bei der Entwicklung von MASH. MASH tritt häufig zusammen mit kardiovaskulären Erkrankungen auf, welche von der Atherosklerose herrühren könnten. Zusätzlich zu den Risikofaktoren, die sowohl Atherosklerose als auch MASH beeinflussen, gibt es bereits Hinweise, dass der 3',5'-zyklische Guanosinmonophosphat (cGMP)-Stoffwechselweg einen Einfluss auf beide Krankheiten haben kann.

Die Bildung des sekundären Botenstoffes cGMP durch die Stickstoffmonooxid (NO)-sensitive Guanylylzyklase (NO-GC) ist ein zentraler physiologischer Mechanismus im kardiovaskulären System. Die Bedeutung des NO/NO-GC/cGMP-Signalweges spiegelt sich in der erfolgreichen Behandlung von Erkrankungen wie Herzversagen oder Lungenhochdruck mithilfe von Substanzen, die diesen Signalweg modulieren, wider. Im hepatischen System wurde der NO/NO-GC/cGMP-Signalweg in HSCs beschrieben. Die Pathogenese von Lebererkrankungen wie MASH wird mit einer verminderten Bioverfügbarkeit von NO und einem erhöhten oxidativen Stress in Verbindung gebracht. Oxidativer Stress kann die Oxidation der Häm-Gruppe der NO-GC zufolge haben, wodurch das Enzym nicht mehr durch NO stimuliert werden kann. Im Gegensatz zu NO kann die vor Kurzem entwickelte Klasse der NO-GC Aktivatoren die oxidierte, Häm-freie, NO-GC binden und somit möglicherweise cGMP-Spiegel in erkrankten Lebern erhöhen. Ziel der vorliegenden Studie war es, die Rolle und pharmakologische Relevanz des NO/NO-GC/cGMP-Signalweges bei MASH zu ermitteln, wobei der Schwerpunkt

auf HSCs lag. Insbesondere wurde untersucht, ob ein neuartiger NO-GC-Aktivator von Bayer das Fortschreiten der Krankheit beeinflussen könnte.

Um diese Fragen zu ergründen, wurde ein MASH/Atherosklerose Komorbiditäts-Mausmodell etabliert, indem Apolipoprotein E Knockoutmäuse mit einer fettreichen Diät (HFD; von hieran HFD-Mäuse genannt) gefüttert wurden. Die Kerneigenschaften von MASH, einschließlich der Aktivierung von HSCs, wurden mithilfe histologischer Techniken in HFD- und Kontrollmäusen untersucht. Die Expression zentraler Komponenten des cGMP-Signalweges (NO-GC und cGMP-abhängige Proteinkinase Typ I, cGKI) und weiterer Markerproteine für HSCs (Desmin, α-SMA und SM22) wurde in Lysaten und Schnitten von Lebergewebe mittels Western Blot und Immunfluoreszenzfärbung untersucht. cGMP wurde in Echtzeit in primären HSCs aus Mäusen unter Zuhilfenahme eines Förster-Resonanzenergietransfer-basierten cGMP Biosensors visualisiert. Dabei wurde die räumliche und zeitliche Dynamik von cGMP-Signalen in Antwort auf NO und einem neuen NO-GC Aktivator in primären HSCs an Tag 2 und Tag 8 in Kultur beobachtet. HFD Mäuse wurden mit dem neuen NO-GC Aktivator behandelt (HFD ergänzt mit aktivator), um seinen Effekt auf die Entwicklung von MASH zu untersuchen. Zusätzlich zur Histologie und zu Immunfluoreszenzfärbungen, wurden die Lebern von mit Aktivator behandelten Mäusen einer biochemischen und RNA-Expressionsanalyse unterzogen.

HFD-Mäuse haben MASH in Kombination mit der Komorbidität Atherosklerose entwickelt. Im Gegensatz zu Kontrollmäusen wiesen Sie eine Gewichtszunahme und Hepatomegalie zusammen mit dem gesamten Spektrum an Charakteristika für MASH, einschließlich Steatose, Ballooning, Entzündung und Fibrose auf. Die Entwicklung der Fibrose war mit einer Aktivierung von HSCs, gekennzeichnet durch Ausbreitung und erhöhter Expression von α-SMA und SM22, in MASH Lebern verbunden. NO-GC und cGKI waren robust in HSCs, unabhängig von ihrem Aktivierungszustand, exprimiert. Übereinstimmend mit unseren Befunden *in vivo*, haben sowohl Tag 2 als auch Tag 8 HSCs in Kultur cGMP in Antwort auf NO oder den NO-GC Aktivator gebildet. Besonders bemerkenswert war, dass die Behandlung von HFD-Mäusen mit dem NO-GC Aktivator den MASH Phänotyp verbessert hat. Dies zeigte sich an verringertem Ballooning von Hepatozyten, verringerter hepatischer Fibrose und einem Trend zu reduzierten Leberenzym-Leveln (AST und ALT) und Entzündungsmarkern, wie eine histochemische Analyse (Mac-2 und F4/80) und RT-PCR (TNFa, IL6, IL1A, IFNG, CCL2 und CXCL10) zeigten.

Insgesamt deuten unsere Ergebnisse daraufhin, dass in HSCs der Leber ein funktionierender NO/NO-GC/cGMP-Signalweg existiert und dass seine Komponenten NO-GC und cGKI als HSC-Marker dienen könnten. Interessanterweise könnte die pharmakologische Aktivierung dieses Signalweges eine neue Strategie für die Behandlung von MASH darstellen.

Summary

Metabolic dysfunction-associated steatotic liver disease (MASLD) is the primary cause of liver-related illness and mortality caused by caloric excess and a sedentary lifestyle. MASLD encompasses a spectrum of chronic liver diseases that begins with hepatic steatosis and over time progresses to a more malignant form termed metabolic dysfunction-associated steatohepatitis (MASH), cirrhosis, and ultimately hepatocellular carcinoma. The progression from MASLD to MASH starts with the hepatic accumulation of lipids (steatosis) and is followed by the activation of several liver resident cells, including hepatic stellate cells (HSCs). Transition of HSCs from a ''quiescent'' to an ''activated'' phenotype is a key driver in the development of MASH. MASH is often associated with cardiovascular disease, which may have its origin in atherosclerosis. In addition to the risk factors that influence both atherosclerosis and MASH, it has been reported that the 3',5'-cyclic guanosine monophosphate (cGMP) pathway may have an impact on both diseases.

The generation of the second messenger cGMP via nitric oxide (NO)-sensitive guanylyl cyclase (NO-GC) is central to regulating cardiovascular physiology. The significance of the NO/NO-GC/cGMP pathway is reflected by the successful clinical use of drugs that modulate this pathway to treat diseases like heart failure and pulmonary hypertension. Within the hepatic system, the NO/NO-GC/cGMP pathway has been described in HSCs. The pathogenesis of liver diseases like MASH is associated with the reduced bioavailability of NO and an increased oxidative stress. Oxidative stress can lead oxidation of NO-GC's heme group, rendering the enzyme unresponsive to NO. In contrast to NO, the recently developed class of NO-GC activators can bind the oxidized heme-free NO-GC and can thereby potentially increase hepatic cGMP levels under disease conditions. The present study aimed to identify the role and pharmacological relevance of the NO/NO-GC/cGMP pathway in MASH, with a focus on HSCs. In particular, we explored whether a novel NO-GC activator tool compound from Bayer might affect the disease progression.

To address these questions, a MASH/atherosclerosis comorbidity mouse model was established by feeding apolipoprotein E knockout mice a high-fat diet (HFD; hereafter referred to as HFD mice). The key features of MASH, including the activation of HSCs, were analysed in HFD and control mice using histological techniques. The expression of central components of

the cGMP pathway (NO-GC and cGMP dependent protein kinase type I, cGKI) and HSC markers (desmin, α-SMA, and SM22) was analysed in liver tissue lysates and sections via western blot and immunofluorescence staining respectively. cGMP was visualized in real-time in primary murine HSCs using a Förster/fluorescence resonance energy transfer-based cGMP biosensor. Thereby, the spatiotemporal dynamics of cGMP signals in response to NO and a novel NO-GC activator were monitored in primary HSCs on day 2 and day 8 in culture. HFD mice were treated with the novel NO-GC activator (HFD supplemented with activator) to study its effect on MASH development. In addition to histology and immunofluorescence staining, the livers from activator treated mice were subjected to biochemical and RNA expression analysis.

HFD mice successfully developed MASH together with its comorbidity atherosclerosis. They showed weight gain and hepatomegaly together with the full spectrum of characteristics of MASH, including steatosis, ballooning, inflammation, and fibrosis as opposed to control mice. The development of fibrosis was associated with the activation of HSCs within the MASH livers marked by their expansion and increased expression of α-SMA and SM22. NO-GC and cGKI exhibited robust expression in HSCs independent of their activation state. In line with our *in vivo* findings, both day 2 and day 8 HSCs in culture showed cGMP generation in response to NO or the NO-GC activator. Most strikingly, treatment of HFD mice with the NO-GC activator improved the MASH phenotype as reflected by reduced hepatocyte ballooning and hepatic fibrosis, and a trend towards reduced liver enzyme levels (AST and ALT) and inflammation markers analysed via histochemistry (Mac-2 and F4/80) and RT-PCR (TNFa, IL6, IL1A, IFNG, CCL2, and CXCL10).

Taken together, these results imply that a functional NO/NO-GC/cGMP signalling pathway exists in HSCs in the liver and its components NO-GC and cGKI can be proposed as markers for HSCs. Importantly, the pharmacological activation of this pathway might provide a new strategy for the treatment of MASH.

List of abbreviations

α-SMA	α-smooth muscle actin
ABC	Avidin biotin complex
ACTA2	Actin alpha 2
ALT	Alanine aminotransferase
a.u.	arbitrary unit
ANP	Atrial natriuretic peptide
ApoE	Apolipoprotein E
APS	Ammonium persulfate
AST	Aspartate transferase
BDL	Bile duct ligation
BNP	B-type natriuretic peptide
BSA	Bovine serum albumin
BW	Body weight
CAG	Cytomegalovirus immediate early enhancer/chicken β actin/rabbit β-globin
cAMP	3',5'-cyclic adenosine monophosphate
Cat-#	Catalogue number
CCD	Charged-coupled device
CCl_4	Carbon tetrachloride
CD-HFD	Choline-deficient high-fat diet
CFP	Cyan fluorescent protein
cGi500	cGMP indicator with an EC_{50} of 500nM
cGK	cGMP-dependent protein kinase
cGMP	3',5'-cyclic guanosine monophosphate
CNP	C-type natriuretic peptide
Cre	Cyclization recombination
DAB	3'3'-diaminobenzidene
DEA/NO	Diethylammonium (Z)-1-(N,N-diethylamino)diazen-1-ium-1,2-diolate
DMEM	Dulbecco's modified Eagle medium
DMSO	Dimethyl sulfoxide
DNA	Deoxyribonucleic acid
ECM	Extracellular matrix
ECL	Enhanced chemiluminescence
EDTA	Ethylenediamine tetraacetate
EGTA	Ethylene glycol tetraacetic acid
eNOS	Endothelial NOS
FCS	Fetal calf serum
FOV	Field of view
FRET	Förster resonance energy transfer
GAPDH	Glyceraldehyde 3-phosphate dehydrogenase
GBSS/A	Gey's balanced salt solution A
GBSS/B	Gey's balanced salt solution B
GC	Guanylyl cyclase
GMP	Guanosine monophosphate
GTP	Guanosine triphosphate

HCC	Hepatocellular carcinoma
Hepes	4-(2-hydroxyethyl)-1-piperazineethanesulfonic acid
HFD	High-fat diet
HRP	Horseradish peroxidase
HSCs	Hepatic stellate cells
IB	Imaging buffer
IF	Immunofluorescence
IHC	Immunohistochemistry
iNOS	Inducible NOS
KCs	Kupffer cells
Lrat	Lecithin retinol acyltransferase
loxP	locus of crossing-over [X] of P1
LSECs	Liver sinusoidal endothelial cells
MASLD	Metabolic dysfunction-associated steatotic liver disease
MASH	Metabolic dysfunction-associated steatohepatitis
NAFLD	Non-alcoholic fatty liver disease
NASH	Non-alcoholic steatohepatitis
NDS	Normal donkey serum
NGS	Normal goat serum
nNOS	neuronal NOS
NO	Nitric oxide
NO-GC	NO-sensitive guanylyl cyclase
NOS	Nitric oxide synthase
pAb	primary antibody
PBS	Phosphate-buffered saline
PCR	Polymerase chain reaction
PDE	Phosphodiesterase
PDMS	Polydimethylsiloxan
pGC	Particulate guanylyl cyclase
PKG	Protein kinase G
PMSF	Phenylmethylsulfonylfluoride
PVDF	Polyvinylidene fluoride
RNA	Ribonucleic acid
ROI	Region of interest
Rosa26	Reverse orientation splice acceptor clone 26
sAb	secondary antibody
SDS	Sodium dodecyl sulphate
SEM	Standard error of the mean
TAE	Tris-acetate-EDTA
TAA	Thioacetamide
TBE	Tris-borate-EDTA
TBS	Tris-buffered saline
TBS-T	TBS-Tween
TEMED	N,N,N’,N’-Tetramethylethylendiamin
Tris	Tris(hydroxymethyl)-aminomethane
YFP	Yellow fluorescent protein

Table of Contents

1 Introduction

1.1 The cGMP signalling pathway

3', 5'- cyclic guanosine monophosphate (cGMP) is an intracellular second messenger crucial to many physiological processes **(Figure 1)** [1]. In the peripheral blood vessels, cGMP regulates vascular tone via vascular smooth muscle cell (VSMC) relaxation [2]. It can enhance the growth and survival of various cell types including VSMCs [3] and melanoma cells [4]. Within the hepatic system, cGMP regulates sinusoidal tone, consequently influencing intrahepatic portal pressure and fibrosis [5-7].

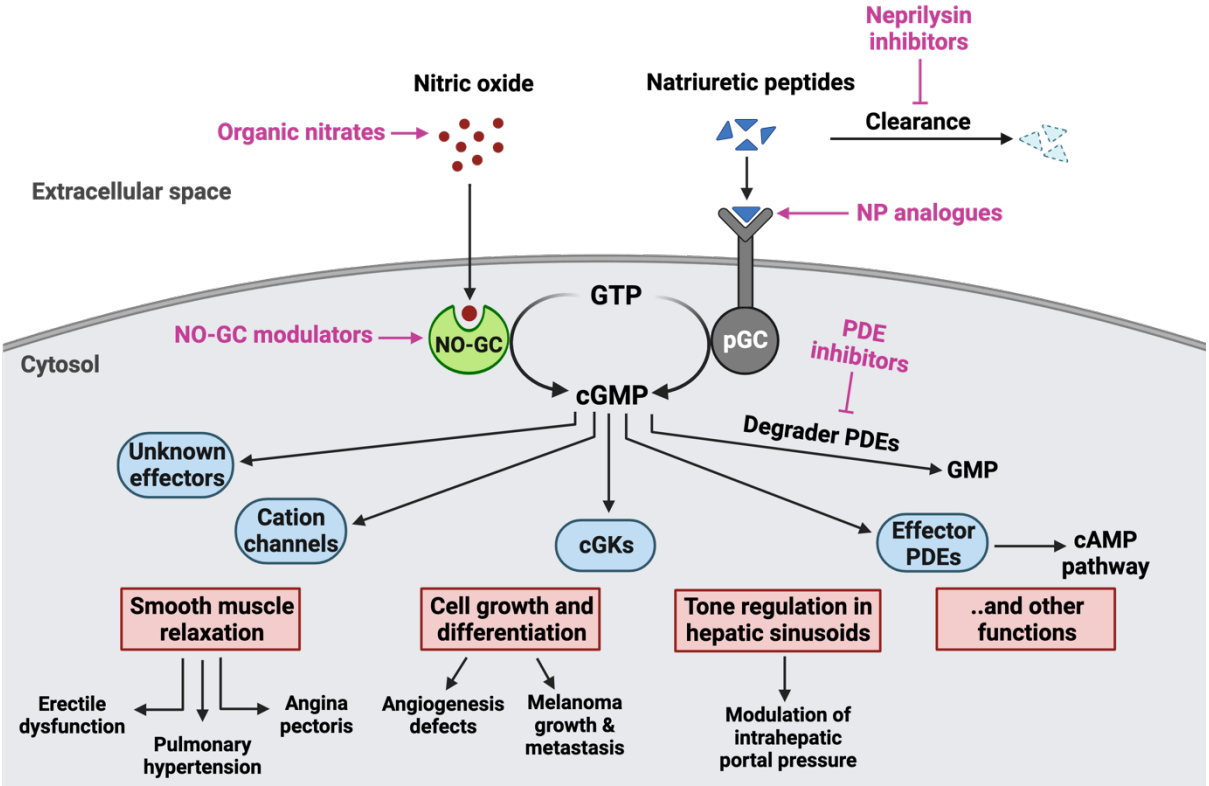

Figure 1: The cGMP signalling pathway. The intracellular second messenger cGMP is generated from guanosine triphosphate by two types of enzymes, the nitric oxide sensitive soluble guanylyl cyclases (green) and the particulate guanylyl cyclases (grey). cGMP in turn activates cGMP-dependent protein kinases, cGMP-gated ion channels, and PDEs (blue). These effector proteins mediate the downstream effects of cGMP. Degrader PDEs inactivate cGMP by catabolising it to 5' GMP. Some of the physiological effects (red) of cGMP include smooth muscle relaxation, cell growth and differentiation, and hepatic tone regulation. Any dysfunction in these cGMP mediated physiological effects leads to several diseases, for which several cGMP modulating drugs have been developed (pink text) (adapted from[8]). NP- natriuretic peptide; NO-GC- NO-sensitive guanylyl cyclase; pGC- particulate guanylyl cyclase; GTP- guanosine triphosphate; cGMP- cyclic guanosine monophosphate; cAMP- cyclic adenosine monophosphate; cGK- cGMP-dependent protein kinase; PDE- phosphodiesterase. The figure is created using Biorender.com.

Given the significance of cGMP in regulating a multitude of functions, any dysfunction in this pathway is recognized as the underlying pathophysiological cause of many cardiovascular and non-cardiovascular diseases. Therefore, during the last decade, cGMP emerged as a novel drug target for the treatment of several diseases [9]. For instance, treatments for pulmonary arterial hypertension (PAH) involve stimulation of the cGMP generator NO-GC and the inhibition the degrader PDEs. This leads to elevation in cGMP levels, resulting in vasodilation and suppression of VSMC proliferation [10]. It is now well established that the effectiveness of cGMP modulating drugs extend beyond cardiovascular disease settings to other organs [11]. These include renal fibrosis [12], hepatic fibrosis [13-15], and cancer [16].

1.1.1 Generators of cGMP and their ligands- structure, function, and regulation

cGMP is generated by two distinct classes of guanylyl cyclase enzymes: (1) the soluble NO-sensitive GC (NO-GC) and (2) the membrane-spanning particulate GCs (pGCs) which catalyse the conversion of guanosine triphosphate (GTP) to cyclic guanosine monophosphate (cGMP). The transmembrane pGCs are activated by natriuretic peptides (NPs) while the soluble NO-GC is primarily activated by nitric oxide (NO) [17].

NO-GC, also known as sGC exists as heterodimers consisting of two homologous subunits, α and β [17, 18]. In mammals, two functional isoforms of NO-GC are known to exist namely NO-GC1 ($\alpha1\beta1$) and NO-GC2 ($\alpha2\beta1$) [19] in which, the $\beta1$ subunit acts as the dimerizing partner for both α subunits. A $\beta2$ subunit was identified through homology analysis; however, it is regarded as a pseudogene due to the absence of catalytic activity and extremely low gene expression. Both isoforms of NO-GC are activated by NO, but they differ in their subcellular and tissue localization. While NO-GC1 is ubiquitously distributed and abundantly expressed in the cardiovascular system, NO-GC2 is mainly expressed in the brain [20].

Both subunits of NO-GC are structurally composed of four distinct domains each: an N-terminal heme nitric oxide/oxygen binding domain (H-NOX), a PAS-like (Per/Arnt/Sim) domain, a coiled-coil (CC) domain, and a catalytic (CAT) domain [18]. While each subunit has a H-NOX domain, only the H-NOX domain of the β subunit binds a heme cofactor, with direct ligation facilitated through a conserved histidine 105 residue [21, 22]. The CAT domain located at the C-terminal provides the active site. Binding of the endogenous NO induces a rotation of the β H-NOX and the PAS domains. This leads to a straightening of the CC domains, which, in turn,

moves the CAT domain into an active form, allowing it to convert GTP to cGMP [23]. However, during oxidative stress, the heme in NO-GC is susceptible to oxidation (from Fe^{2+} to Fe^{3+}). This results in a reduced affinity between NO-GC and NO, leading to a heme-free state, the apo-NO-GC. The apo-NO-GC can no longer react to NO and produce cGMP resulting in an impaired NO/NO-GC/cGMP signalling [24]. An impaired NO/NO-GC/cGMP signalling is associated with the progression of cardiovascular and renal diseases [25]. Therefore, a variety of NO-GC modulating drugs have been discovered to enhance cGMP production [26].

Nitric oxide (NO) is a gaseous molecule which modulates a variety of physiological functions. In vivo, NO is synthesized by nitric oxide synthase (NOS), which catalyses a 5-electron oxidation of L-arginine in the presence of molecular oxygen and NADPH to produce NO and citrulline [27]. There are three different isoforms of NOS: the endothelial NOS (eNOS), the neuronal NOS (nNOS), and the inducible NOS (iNOS). NO produced by the endothelial cells diffuses into the bloodstream and the nearby VSMCs to inhibit platelet aggregation and induce vasorelaxation. nNOS is found in neuronal cells and plays a role in long-term potentiation process involved in memory formation. Lastly, the iNOS is mainly found in macrophages and microglia and is associated with immune response. The enzymatic activity of eNOS and nNOS is regulated by calcium/calmodulin, whereas iNOS functions independently of calcium levels [17, 28].

In contrast to the soluble GC, the membrane-bound pGCs are activated by natriuretic peptides. Members of the pGC subfamily are homodimers and consist of an extracellular ligand-binding domain, a transmembrane domain, and an intracellular region containing the catalytic domain. Mammals express seven membrane-spanning forms of pGCs termed GC-A through GC-G however, specific ligands have been identified only for three of them. There are three types of NP ligands: atrial (A-type) NP, brain (B-type) NP, and C-type NP [29]. GC-A generates cGMP in response to ANP and BNP. GC-A is expressed in the kidney, vasculature, endothelium, heart and in the central nervous system where it regulates natriuresis, vascular remodelling, blood pressure and sympathetic activity [30]. GC-B is activated by CNP in a paracrine manner and is abundantly expressed in the nervous system, bone, and ovaries. Its main functions include dorsal root ganglion bifurcation, endochondral ossification, and oocyte maturation [17]. GC-C is stimulated by the endogenous peptide ligands guanylin and uroguanylin and is also a target for heat stable enterotoxins. It is expressed in the apical

membrane of intestinal epithelial cells where it mediates electrolyte and water transport and epithelial cell growth and differentiation [17, 30]. Lastly, there is the clearance receptor NPR-C which is responsible for clearing the circulating NP via receptor mediated internalization and degradation in the absence of ligand. It is expressed in adrenal glands, brain, kidney, and VSMCs [29].

1.1.2 Effectors and degraders of cGMP

The physiological effects of cGMP are regulated via three classes of cGMP effector proteins: cyclic nucleotide-gated ion channels (CNGs), cGMP-dependent protein kinases (cGKs), and cGMP-regulated phosphodiesterases (PDEs) **(Figure 1)**. CNGs are nonselective cation channels first discovered in the retinal photoreceptors of vertebrates [31]. They are opened by the direct binding of intracellular cyclic nucleotides- cAMP and cGMP allowing Na^+, K^+, and Ca^{2+} to flow into the cell [32]. Mammalian CNG channels are tetramers comprised of six homologous members, which are classified as A and B subunits. Both A and B subunits share similar membrane topology characterized by six transmembrane segments (S1-S6), a reentrant pore (P) loop and cytosolic N- and C-termini [33]. The activation process of CNG channels involves three domains: (1) the channel gate located at the distal end of S6, (2) the cyclic nucleotide binding domain (CNBD) at the C-terminal, and (3) the C-linker domain which couples nucleotide binding to the channel gate. CNG channels are mainly expressed in rods and cones where they regulate phototransduction via cGMP [34] and in olfactory neurons where they mediate sensory transduction using cAMP. Gene knockout studies and mutations in human CNG channel genes have shown to affect vision and olfaction [35].

The cGKs, also known as protein kinase G (PKG) are serine/threonine kinases with wide distribution in eukaryotes. They are composed of three functional domains: an NH_2 terminal domain, a regulatory domain, and a catalytic domain. The regulatory domain has two allosteric cGMP binding sites, whereas the catalytic domain contains the MgATP and peptide-binding pockets. The NH_2 terminus contains leucine/isoleucine zipper which is required for (1) homodimerization, (2) inhibition of catalytic centre in the absence of bound cGMP, (3) affinity and cooperation of cGMP binding sites A and B, and (4) intracellular localization of the enzymes [36]. In mammals, two cGK genes, *prkg1* and *prkg2* encode cGKI and cGKII [37]. The N-terminal domain of cGKI is encoded by two alternative exons that generate the isoforms

cGKIα and cGKIβ. These isozymes differ in cGMP dependence, substrate specificity, and tissue distribution. cGKI is cytosolic and is highly expressed in the cardiovascular, nervous, and the renal system. Like NO-GC, cGKI regulates vascular tone, inhibition of platelet activation, gastrointestinal motility, and synaptic plasticity. The isozyme Iα is found in lung, heart, DRG, and cerebellum while Iβ is expressed in platelets, hippocampal and olfactory neurons. Unlike cGKI, cGKII is anchored at the plasma membrane via myristoylation of the N-terminal. It is expressed in several brain nuclei, kidney, chondrocytes, and lungs [37].

PDEs are a family of related phosphohydrolases that specifically catalyse the hydrolysis of 3' cyclic phosphate bonds of cGMP and cAMP [38]. They are controlled by various biochemical mechanisms like phosphorylation/dephosphorylation, allosteric binding of cGMP or cAMP, binding of Ca^{2+}/calmodulin, and various protein-protein interactions. Many PDEs function to modulate ''clouds'' of cyclic nucleotide in the cell i.e., to prevent this cloud from spreading to inappropriate areas of the cell [38]. There are 11 different families of PDEs ranging from PDE1 to PDE11, usually named with a number which signifies the gene family followed by a suffix letter denoting the gene. These are further sub-classified based on their substrate preferences (cGMP or cAMP) and the different regulatory domains within each family of enzyme [39]. PDEs 4, 7, 8 hydrolyze cAMP, whereas PDEs 5, 6, 9 are cGMP specific. All other PDEs (1, 2, 3, 10, and 11) have dual specificity, hydrolyzing both cAMP and cGMP. PDEs play an important role in the CNS and the cardiovascular system where they regulate learning and memory, VSMC contraction and relaxation, and platelet aggregation. Given the large number of PDE subtypes, their role in different physiological functions is complex and several PDE inhibitors are used for therapeutic intervention in a variety of disorders [38].

1.1.3 Pharmacological modulation of cGMP

As described in the previous sections, the cGMP signalling pathway plays a central role in a wide range of physiological processes. Owing to this significance, components of the cGMP pathway have become important biological targets for treating several diseases. The upcoming paragraphs will describe the clinical significance of these drugs in detail.

The most famous cGMP-targeting drug is sildenafil, launched by Pfizer in 1998 under the trade name Viagra®. Sildenafil is a selective PDE5 inhibitor used to treat erectile dysfunction (ED). It is administered orally and has a mean terminal half-life of 3-5 hours. During a sexual stimulus,

inhibition of PDE5 results in smooth muscle relaxation within the sinusoids of corpus cavernosum and penile arteries [40]. The effect of sildenafil extends beyond erectile dysfunction to pulmonary arterial hypertension (PAH) where it suppresses inflammation and prevents pulmonary artery remodelling. Although ED and PAH are currently the two therapeutic indications of sildenafil, many studies have been performed to investigate its effects in gastrointestinal, liver, lung, and kidney diseases [41].

Within the cGMP signalling system, natriuretic peptides (NPs) have also emerged as therapeutic agents due to their beneficial physiological effects. Drugs related to NP/pGC/cGMP signalling act by inhibiting the degradation of NPs. One such compound is sacubitril, an inhibitor of NP-degrading enzyme neprilysin (NEP) [42]. The consequence of NEP inhibition is an increase in circulating NPs and in turn the cGMP levels. In chronic heart failure, the inverse relationship between NP/pGC/cGMP and angiotensin II signalling is compromised, resulting in simultaneous activation of both pathways thereby affecting cardiac contractility. To circumvent this problem, the combination drug sacubitril/valsartan [43] has been approved for the treatment of heart failure which simultaneously augments the NP system and inhibits angiotensin II [44].

NO-GC facilitates the pharmacological modulation of NO/cGMP signalling pathway. Given its central role in regulating various bodily functions, the NO/NO-GC/cGMP pathway is considered an effective treatment option for several cardiovascular diseases and beyond. Several NO-releasing compounds such as isosorbide mononitrate and dinitrate and glycerol trinitrate are used to treat angina pectoris. However, these traditional NO-liberating compounds have major disadvantages such as small therapeutic window and reaction with ROS under oxidative stress resulting in endothelial and tissue damage [45]. To overcome these drawbacks, two distinct compound classes have been discovered which act in a NO-independent manner. This topic will be discussed in detail in the following section.

1.1.4 NO-GC stimulators and activators

Two distinct compound classes that are capable of activating NO-GC independent of NO were discovered at Bayer namely, NO-GC stimulators and activators [46]. Both compound classes act via different mechanisms to induce cGMP generation **(Figure 2)**. Prior to the discovery of stimulators and activators, direct NO-independent stimulation of NO-GC was demonstrated

with a synthetic benzylindazole compound called YC-1 [47]. Consequently, the structure of YC-1 formed the basis for the development of several NO-GC stimulators. The activity of NO-GC stimulators at the heme-containing enzyme is independent of NO but is enhanced in the presence of NO. Besides acting independently of NO, the stimulators are also able to stabilize NO-NO-GC binding thereby sensitizing the enzyme to low levels of NO [26, 45].

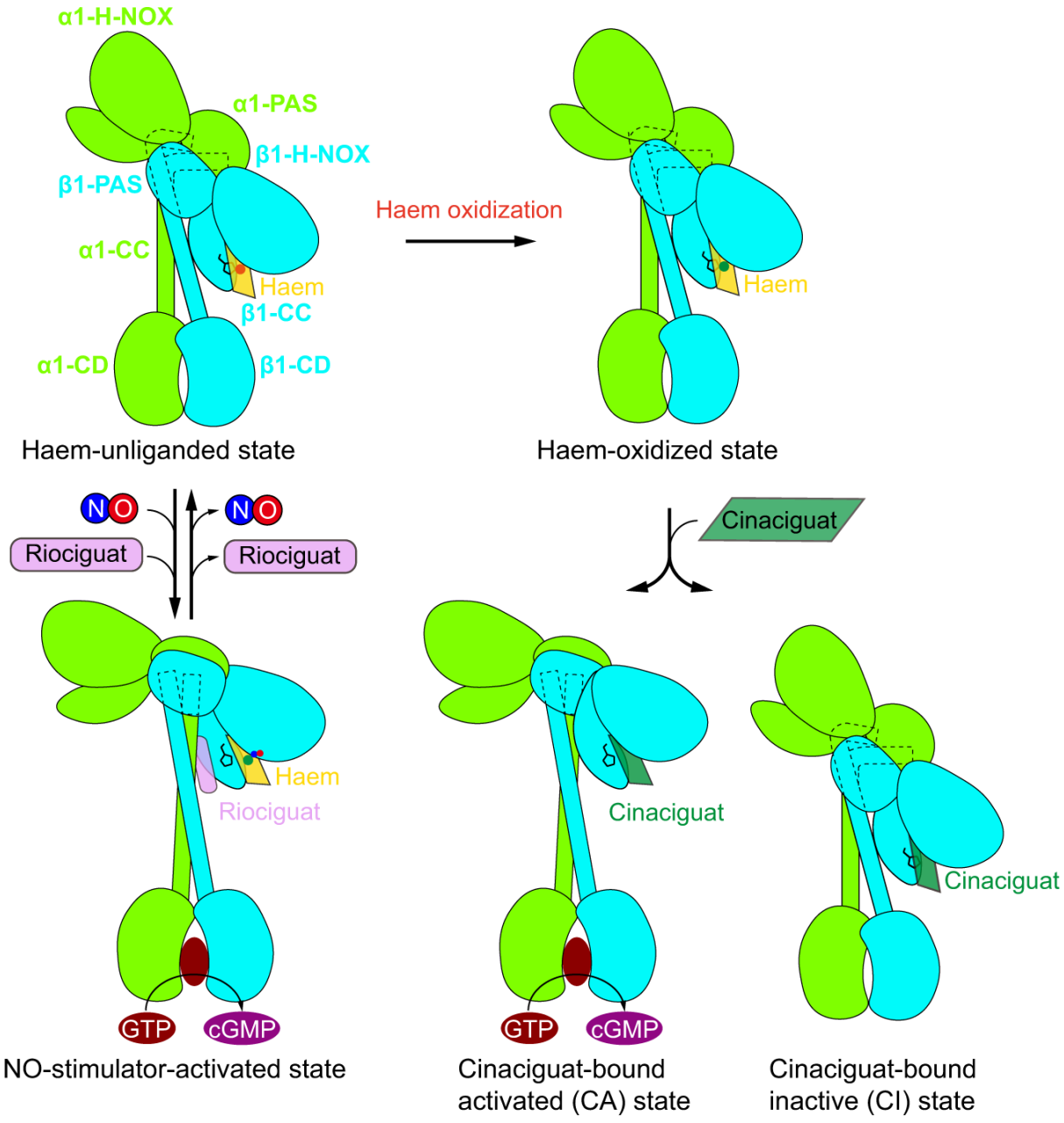

Figure 2: Mechanism of action of NO-GC stimulators and activators. In its native, heme-containing state, endogenous NO binds to and activates NO-GC. NO-GC stimulators like riociguat directly stimulate this native form of the enzyme, thereby increasing its catalytic activity. Oxidative stress oxidises NO-GC, leading to loss of the heme group, rendering the enzyme dysfunctional. Heme-free NO-GC is unable to bind and respond to NO. NO-GC activators like cinaciguat fill this void as they specifically activate the oxidised and heme-free NO-GC. The figure is taken from Liu et al. 2021 [48].

However, as mentioned in section **1.1.1**, under oxidative stress conditions the heme group in NO-GC is prone to oxidation. Heme oxidation results in a reduced affinity between NO and NO-GC, leading to a heme-free state, the apo-NO-GC. The oxidized and heme-free NO-GC can no longer respond to NO or NO-GC stimulators. This is where the NO-GC activators come into play. This novel class of compounds specifically activate the dysfunctional, oxidized, and heme-free NO-GC. They bind inside the heme pocket of the β1 H-NOX domain and replace the Fe^{3+}-heme of oxidized NO-GC, resulting in cGMP generation [48].

Together, NO-GC stimulators and activators provide a broad therapeutic potential for many pathological conditions. These NO-GC modulators have therapeutic applications in cardiovascular, kidney, liver, and lung diseases [49]. Consequently, in the year 2013, the first NO-GC stimulator riociguat was approved for the treatment of pulmonary hypertension due to its vasorelaxation properties. Additional preclinical and clinical studies are ongoing for the treatment of cardiometabolic diseases, chronic kidney disease, liver fibrosis, and cirrhosis. In diseases like fibrosis and cirrhosis associated with oxidative stress, NO-GC activators might prove beneficial due to their ability to activate oxidized and heme-free NO-GC. In conclusion, the discovery of NO-GC stimulators and activators represents a milestone in the field of NO/NO-GC/cGMP pharmacology due to their unique mode of action and a broad therapeutic potential.

1.1.5 cGMP imaging using fluorescent biosensors

To investigate the role of cGMP in (patho-)physiology, it is important to understand when, where, and how much cGMP is being produced in a given cell, tissue, or organ. Conventional methods such as antibody-based assays are widely used to measure cGMP levels at a specific time point in cells or in whole organs. Since these assays are performed with homogenized cell or tissue samples, they have relatively low spatial and temporal resolution. To overcome these limitations, genetically encoded cGMP biosensors have been developed that allow for monitoring cGMP signals in a native healthy environment as well as in disease conditions. Besides providing a single cell resolution, it allows to visualize acute cGMP levels in response to different ligand and drug applications between cells within the same culture in real-time [50].

Most of the cGMP biosensors are based on the principle of Förster/fluorescence resonance energy transfer (FRET). FRET is a physical process dependent on distance, by which energy is transferred between two fluorophores without radiation by the means of dipole-dipole coupling [51]. It consists of a FRET donor fluorophore, a FRET acceptor fluorophore, and a linker region containing two cGMP-binding sites derived from either cGKs or PDEs. FRET is based on the proximity-dependent (~2-6 nm) energy transfer from the excited donor to the acceptor fluorophore. The percentage of energy transferred between these two fluorophores is called FRET efficiency. Binding of cGMP results in a conformational change of the sensor protein thereby altering the FRET efficiency **(Figure 3)** [50].

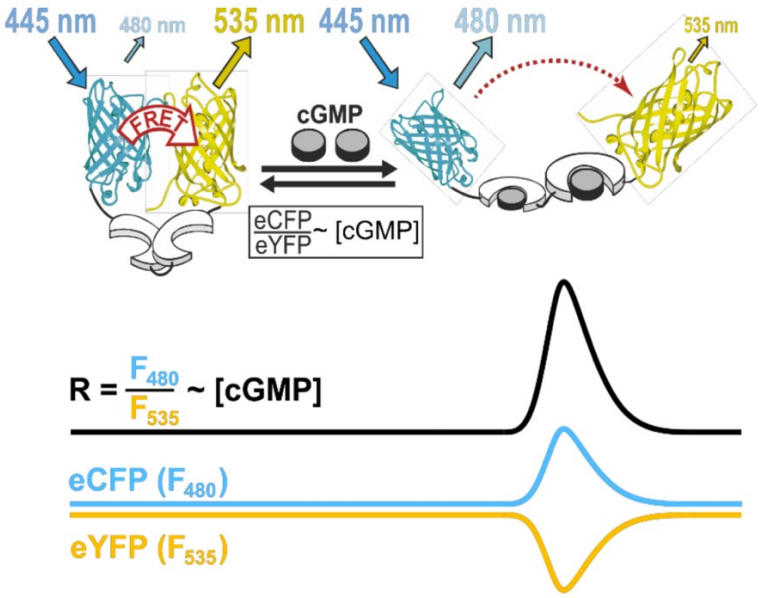

Figure 3: Working principle of FRET-based cGMP biosensor cGi500. cGi500 consists of tandem cGMP-binding sites of the bovine cGKI flanked by CFP and YFP. In the absence of cGMP, FRET occurs from CFP to YFP. Binding of cGMP results in a conformational change and a decrease in FRET efficiency. Thus, the FRET efficiency of cGi500 depicted as CFP/YFP ratio correlates with the cGMP concentration. The figure is modified from Thunemann et al. 2103 [52].

The present study made use of a ratiometric FRET-based cGMP biosensor cGi500 (cGMP indicator with an apparent EC_{50} of 500 nM). This sensor was developed by Russwurm and colleagues in which the cGMP-binding domain of cGKI is flanked by enhanced cyan fluorescent protein (CFP) and enhanced yellow fluorescent protein (YFP) [53]. In the absence of cGMP, excitation of CFP leads to strong YFP fluorescence and weak CFP fluorescence. Binding of cGMP results in a conformational change of the cGMP binding domain leading to reduced FRET efficiency (increased CFP fluorescence and decreased YFP fluorescence). Hence, the CFP/YFP ratio (referred to as R~[cGMP]) serves as an indicator of the cGMP concentration

(Figure 3). Transgenic mice that stably express this biosensor globally in all cell types (cGi-L1) or in a cell type-specific manner (cGi-L2) using Cre/loxP system were generated in our laboratory [52]. Both of these constructs are inserted into the *Rosa26* gene locus driven by the ubiquitous cytomegalovirus early enhancer/chicken β-actin/β-globin (CAG) promoter (R26-CAG-cGi500 mice). In the present study, real-time cGMP imaging was performed in cGi500-L1 mice that express the cGMP sensor globally in all cell types.

1.2 The hepatobiliary system

The hepatobiliary system is an intricate network of organs, ducts, and structures that play a central role in digestion, processing of nutrients, and in detoxification of the body. This system is comprised of the liver, gall bladder, and associated bile ducts.

1.2.1 Anatomy and physiology of the liver

The liver is the largest organ in the body, accounting for 2 % to 3 % of the average body weight. It is dark reddish-brown in colour and is located in the right upper quadrant of the abdominal cavity under the diaphragm and is protected by the rib cage. The liver is grossly divided into two lobes when viewed from above: a right and a left lobe. The falciform ligament on the anterior surface of the liver makes a superficial division between the right and the left lobes. Two additional lobes: the caudate and the quadrate lobe are visible when viewed from below [54].

Microscopically, each liver lobe is divided into hepatic lobules which are the structural and functional units of the liver. The lobules consist of chords of hepatocytes arranged in a hexagonal shape around the central vein. Located at the periphery of this hexagon are the portal triads consisting of the hepatic artery, portal vein, and the bile ducts **(Figure 4)**. The liver receives a dual blood supply from the hepatic artery, which carries the oxygen-rich blood from the aorta and the portal vein, which carries the nutrient-rich blood from the gastrointestinal tract, spleen, and the pancreas. The blood from the artery and portal vein mixes within the hepatic sinusoids before draining into the systemic circulation via the central vein [55].

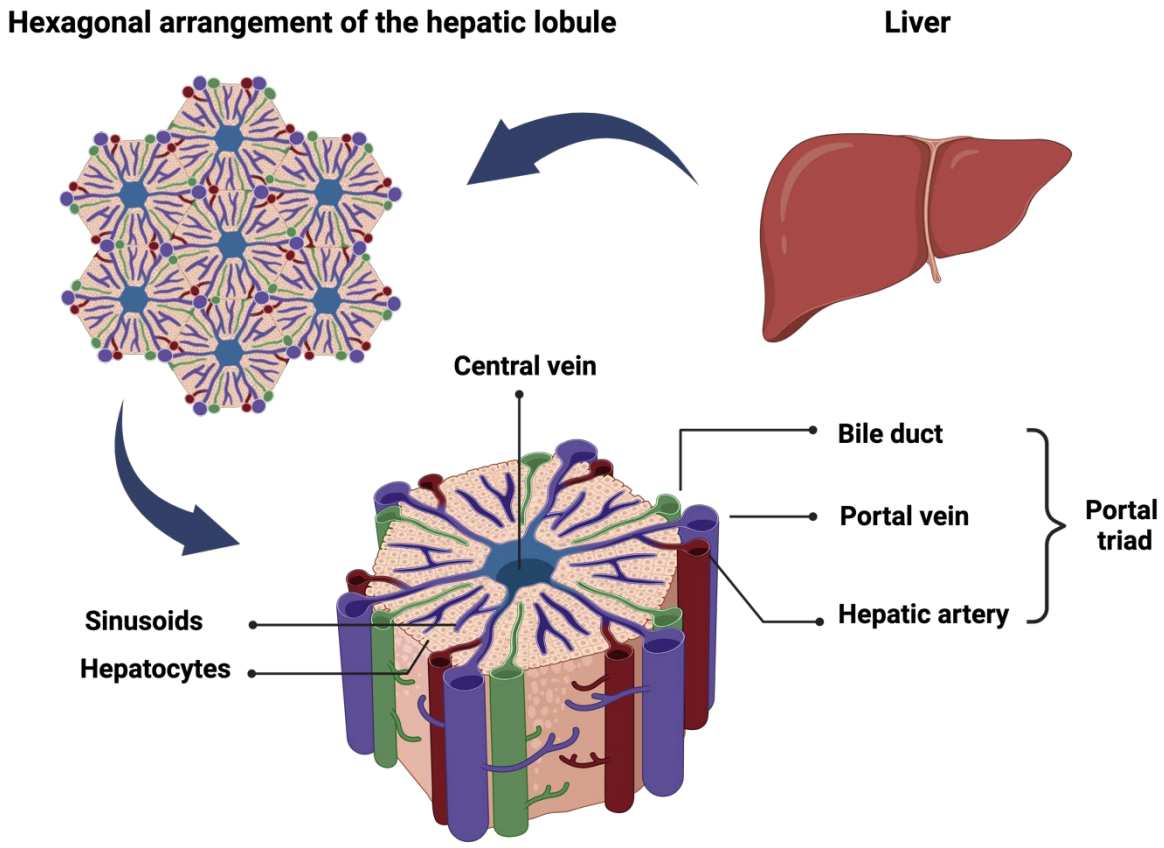

Figure 4: Structure of the hepatic lobule. Hepatic lobules are small divisions of the liver at the microscopic scale. It is the building block of the liver tissue containing plates of hepatocytes and sinusoids radiating from the central vein towards the periphery. The bile duct, hepatic artery, and the portal vein make up the portal triad. The figure is created using Biorender.com.

As the blood flows across the lobule, cells use oxygen and process nutrients, creating metabolites and waste products. This leads to deoxygenation of the blood and secretion of metabolic byproducts along the length of sinusoids. Consequently, varying gradients of oxygen, nutrients, and waste emerge, influencing liver cell function based on their lobular position. This phenomenon is known as ''metabolic zonation'' [55].

1.2.2 Liver cell types

The liver is composed of several different cell types which broadly fall into two categories: the parenchymal cells and the non-parenchymal cells. The parenchymal cells include hepatocytes and cholangiocytes which make up 80 % of the liver cell population. Non-parenchymal cells are composed of Kupffer cells (KCs), hepatic stellate cells (HSCs), and liver sinusoidal endothelial cells (LSECs) which make up 20 % of the liver cell population. **(Figure 5)** provides an overview on the organization of liver cells within a hepatic lobule.

Hepatocytes are the primary epithelial cells which make up the bulk of the liver cell mass. Hepatocytes have a myriad of functions including detoxification, bile secretion, protein synthesis, and carbohydrate and lipid metabolism [56, 57]. The second most abundant epithelial cell populations of the liver are the cholangiocytes. They line the intrahepatic and extrahepatic bile ducts extending from the liver to the duodenum and have a structural resemblance to hepatocytes. They play a central role in bile production, which is a life-sustaining function of the liver [58].

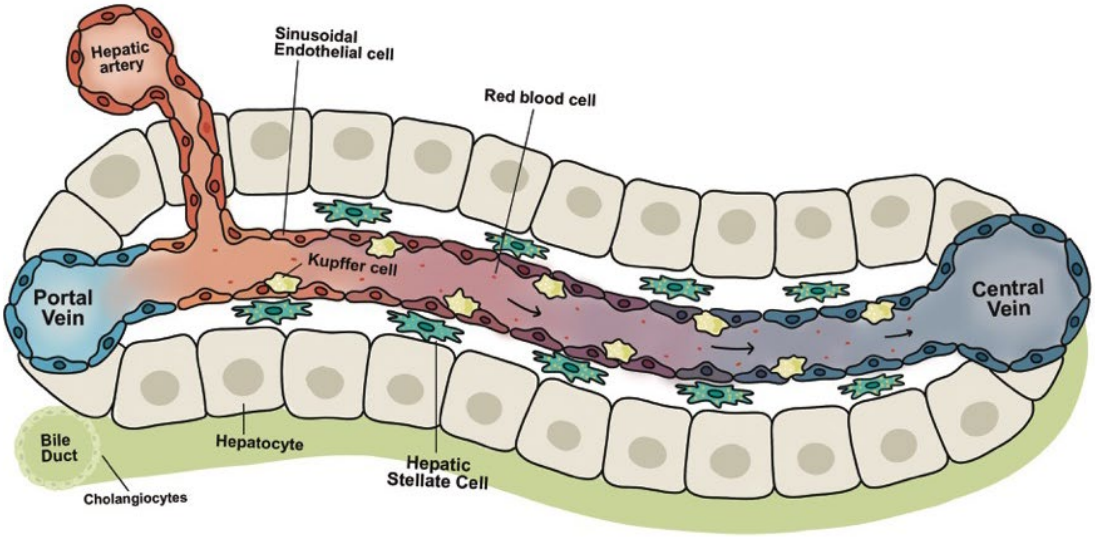

Figure 5: Organization of liver cells. Layers of hepatocytes are situated between the portal triad and the central vein. Non-parenchymal cells associated with the hepatic sinusoids include LSECs, KCs, and HSCs which reside in the space of Disse between hepatocytes and LSECs. The figure is modified from Ramachandran et al. 2020 [59].

LSECs are a specialized endothelial cell population present at the interface between hepatocytes and HSCs. They line the sinusoidal lumen and form fenestrated sieve plates. The main cellular function of LSECs is thought to be formation of a selective barrier against pathogenic agents and for the passing of substances from the blood to hepatocytes and HSCs [60]. Within the hepatic sinusoids are the Kupffer cells, which are the liver resident macrophages. They serve as a first line of defence against materials passing from the portal and arterial circulation as well as the GI tract. Thus, they have an anti-inflammatory function by preventing the movement of these substances across the sinusoids. Changes in the function of KCs is associated with a variety of diseases including MASLD/MASH [61]. Last but not least, hepatic stellate cells (HSCs) are pericytes of liver located in the space of Disse between the hepatocytes and LSECs. They exist in either a quiescent state or an activated state

and play an important role in liver physiology and disease [62]. The following section will discuss HSCs in detail.

1.2.3 Hepatic stellate cells (HSCs)

Located within the perisinusoidal space of Disse, HSCs constitute 5-10 % of the total liver cell population [62]. HSCs have a star-shaped cell body with a centrally located nucleus, a well-developed rough endoplasmic reticulum (RER) and Golgi apparatus, and prominent cytoplasmic processes [63]. In the normal liver HSCs exist in a quiescent state and are characterized by the presence of cytoplasmic lipid droplets **(Figure 6)**. HSCs store 80 % of total body's vitamin A (retinol) as retinyl esters in these lipid droplets and regulate both transport and storage of vitamin A [64]. The synthesis of retinyl esters in the liver is mediated by the enzyme lecithin retinol acyltransferase (LRAT). Additionally, the retinoid droplets contain a fading blue green autofluorescence when excited with a light of 405-407 nm [65]. HSCs regulate the ECM turnover in the space of Disse by secreting proper amounts of ECM proteins together with their degrading enzymes called matrix metalloproteinases (MMPs) and their tissue inhibitors (TIMPs). Apart from these functions, HSCs regulate blood flow within the hepatic sinusoids and also display immunological properties [66].

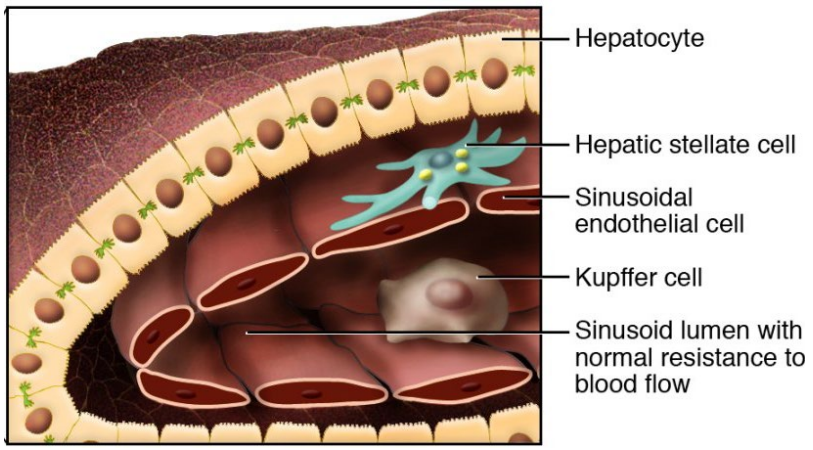

Figure 6: HSCs in a normal liver. HSCs are located in the space of Disse interacting with hepatocytes on one side and LSECs on the other side. Within the normal liver, HSCs are quiescent and contain retinoid droplets that store vitamin A in the form of retinyl esters. The figure is modified from Bataller and Brenner 2005 [67].

Following chronic liver injury, HSCs become activated (aHSCs) and transdifferentiate into a highly proliferative, myofibroblast-like cell type. HSC activation is morphologically characterized by loss of retinoid droplets, enlargement of rough ER, ruffled nuclear membrane, and appearance of contractile filaments. The sequence of HSC activation is believed to occur in two phases: ''initiation'' and ''perpetuation'' **(Figure 7)** [68]. Initiation is

the early event that make cells receptive to a wide range of extracellular stimuli. The cardinal features of initiation include rapid surge in growth factor receptors, acquisition of contractile and fibrogenic phenotype, and modulation of growth factor signalling. This is followed by the perpetuation phase which amplifies the activated phenotype leading to scar formation and secretion of numerous pro-inflammatory cytokines **(Figure 7)** [68]. All these events make aHSCs as a potential target in the onset and progression of liver fibrosis [69, 70].

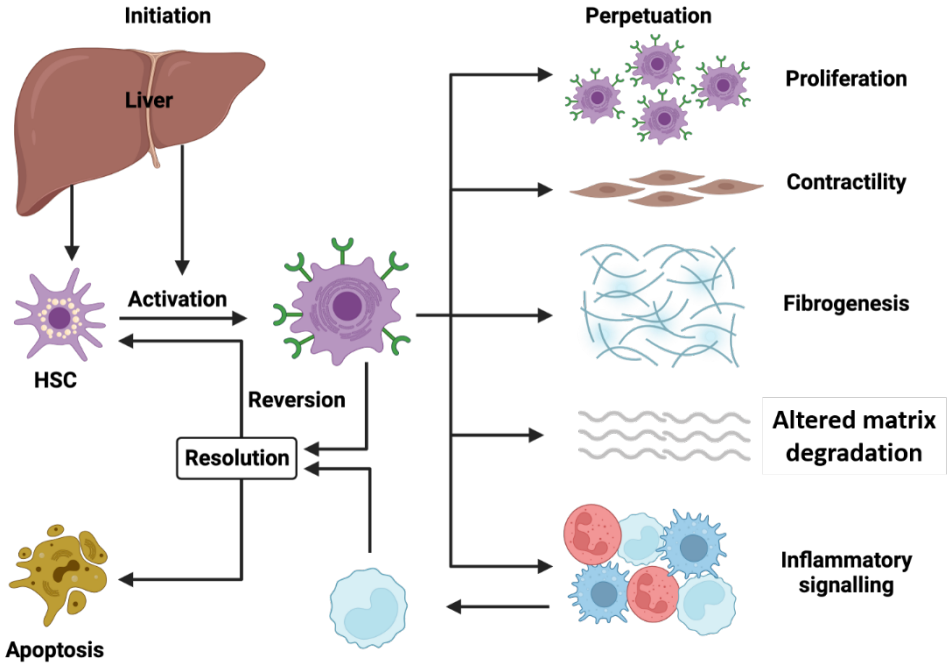

Figure 7: Fate of HSCs following liver injury. Liver injury leads to initiation of HSC transdifferentiation from a quiescent to an activated phenotype. This is followed by perpetuation, characterized by specific phenotypic changes such as proliferation, contractility, fibrogenesis, altered matrix degradation, and inflammatory signalling. These events result in excess accumulation of ECM proteins leading to scar formation and ultimately liver fibrosis. However, in rare cases during resolution of fibrosis, activated HSCs get cleared via apoptosis or by reverting to a quiescent phenotype. The figure is adapted from Tsuchida and Friedman 2017 [68] and is created using Biorender.com.

1.2.4 NO/cGMP signalling pathway in liver

Nitric oxide (NO) and its derivatives play an important role in the physiology and pathophysiology of the liver. eNOS and iNOS are major players in the liver while the function of nNOS is relatively obscure. eNOS is constitutively expressed in LSECs and generates small amounts of NO which maintains liver homeostasis and prevents pathological conditions [6]. For example, in a high-fat diet (HFD) induced obesity model, endothelial NO was shown to inhibit inflammation and insulin resistance in hepatocytes [71]. On the other hand, iNOS is induced in many liver cell types such as LSECs, HSCs, KCs, and other immune cells. Under pathological conditions, large amounts of iNOS-derived NO serves as a major source oxidative

stress and reactive nitrogen species (RNS) causing damage to a wide range of cellular molecules [6]. The NO/NO-GC/cGKI axis has been widely studied for its functional relevance in liver physiology and diseases like non-alcoholic fatty liver disease (MASLD), cirrhosis, and portal hypertension (PHT). Expression of NO-GC was observed in HSCs of healthy livers as well as in livers predisposed to MASLD [14] and fibrosis [72]. The downstream effector cGKI was also detected in HSCs of healthy livers [73, 74]. However, under oxidative stress conditions which is often the case in many liver diseases, NO signalling and affinity of NO to NO-GC is disturbed. Thus, enhancing NO-GC activity independent of NO represents a potential treatment for liver diseases. Pharmacological modulation of NO-GC in liver diseases will be discussed in the following sections.

1.3 Metabolic dysfunction- associated steatotic liver disease (MASLD)

MASLD is the major cause of liver related illness and mortality. A recently conducted meta-analysis found an overall increase of 50.4 % in the global prevalence of MASLD over 3 decades. [75]. The overall prevalence of MASLD globally was estimated to be 32.4 % with significantly higher cases in men than in women [76]. MASLD encompasses a spectrum of chronic liver diseases that begins with hepatic steatosis and over time progresses to metabolic dysfunction-associated steatohepatitis (MASH), MASH associated fibrosis, cirrhosis, and ultimately hepatocellular carcinoma (HCC) **(Figure 8)**. MASLD has emerged as the most prevailing form of chronic liver disease in the 21st century. The development of fatty liver disease is associated with several comorbidities including cardiovascular disease and chronic kidney disease [77]. Of interest to us in the present study is the cardiovascular disease atherosclerosis because of the shared risk factors and the involvement of the cGMP signalling pathway in both conditions.

1.3.1 Old and new nomenclature for fatty liver disease

Worldwide approaches to nomenclature and disease definition are critical for increasing awareness, identifying people at risk, and promoting diagnosis and access to care. The use of language can either create or aggravate stigma, isolate specific parts of the affected population, and thereby lead to health disparities [78]. The term ‘’non-alcoholic fatty liver disease’’ (NAFLD) was coined to describe the entire disease spectrum ranging from steatosis to steatohepatitis. This term specifically indicates the presence of fat in the liver while excluding another prevalent cause, namely excessive alcohol consumption [79]. While this

terminology is commonly used, it has long been perceived that the term ''non-alcoholic'' does not precisely describe the disease aetiology. Furthermore, some consider the term ''fatty'' to be stigmatizing [78].

Consequently, in June 2023, the multinational liver societies leaders from La Asociación Latinoamericana para el Estudio del Hígado (ALEH), American Association for the Study of Liver Diseases (AASLD), and European Association for the Study of Liver (EASL) announced the term ''metabolic dysfunction-associated steatotic liver disease (MASLD) to replace NAFLD and ''metabolic dysfunction-associated steatohepatitis (MASH) to replace NASH [78, 79]. The methodology and results of this Delphi process are summarized in the multinational liver societies' joint publication [78]. A major agreement to modify the definition was to incorporate the presence of at least one of five cardiometabolic risk factors. Individuals without metabolic parameters and no known cause were classified to have steatotic liver disease (SLD) [78]. This new nomenclature and diagnostic criteria are considered to be widely accepted and non-stigmatizing and can promote awareness and improve patient identification.

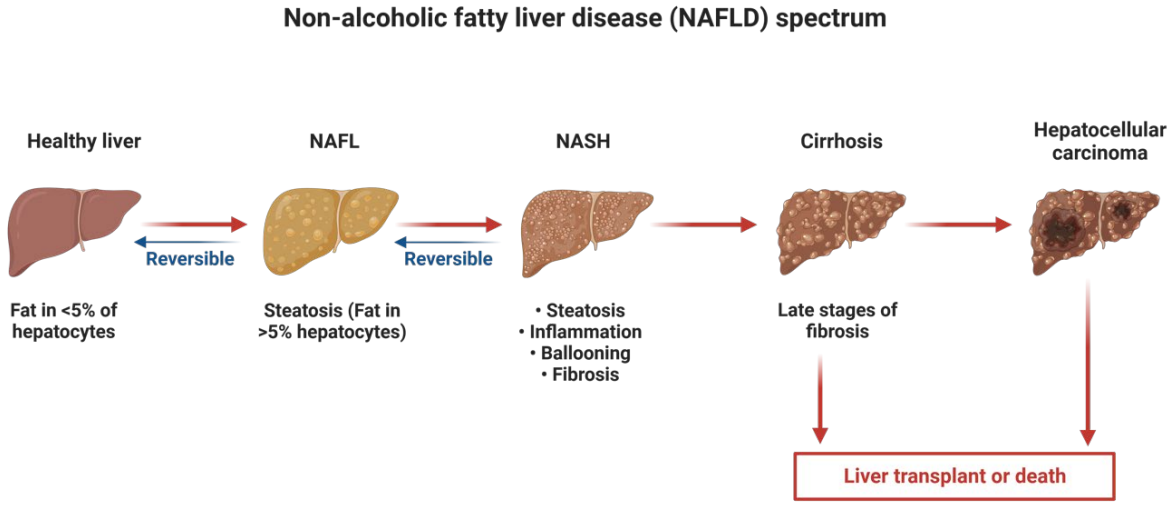

Figure 8: Pathogenesis of MASLD. Hepatic substrate overload, resulting from caloric excess and sedentary lifestyle with high fat, high cholesterol, and high fructose intake, serves as a major driver of MASH. These two factors lead steatosis characterized by oxidative stress and lipotoxicity resulting in accumulation of fat in more than 5% of hepatocytes within the liver. Factors released from these damaged hepatocytes trigger hepatic inflammation which culminates in HSC activation and fibrosis. This condition is known as MASH. By making significant alterations to diet and lifestyle practices, MASH and steatosis are reversible. In most cases, persistent fibrogenesis causes severe scarring to the liver resulting in cirrhosis which can progress to HCC. Development of HCC is associated with high mortality as the current treatment options are limited to liver transplantation which is not easily accessible in majority of the developing world. The figure is created using Biorender.com.

1.3.2 Pathogenesis of MASLD and MASH

Caloric excess and sedentary lifestyle have led to a worldwide surge in obesity and metabolic syndrome which are the major risk factors for the development of MASLD. Excessive accumulation of hepatic triglycerides and steatosis causes fatty liver which is further augmented by inflammation and hepatocyte injury leading to MASH [80]. The pathogenesis of MASH was initially described by the ''two-hit'' hypothesis in which steatosis provides the first hit in turn sensitizing the liver to a second hit of oxidative stress due to inflammation [81]. Overtime, MASLD/MASH has been recognized as a complex disease, and a ''multiple parallel hit'' hypothesis was postulated implicating environmental, metabolic, intracellular, and genetic factors as causes of disease progression [82].

Environmental factors associated with MASH include dietary habits, alcohol consumption, physical activity as well as socio-economic factors. Individuals with fatty liver disease tend to adopt diets high in fructose and fat and embrace a sedentary lifestyle. This paves way for the development of hepatic steatosis in which fat (triglycerides) accumulates in the hepatocytes due to impaired lipid metabolism and insulin resistance [83-85]. Under normal circumstances, the liver processes large quantities of free fatty acids (FFA) but stores only small in the form of triglycerides. This is because the uptake of FFAs via de novo lipogenesis within the liver is balanced by FFA oxidation and secretion into plasma as very-low-density lipoproteins (VLDL) [86]. However, caloric excess and obesity lead to increased fatty acid influx to the liver causing an imbalance between the uptake and elimination of FFAs. This further aggravates steatosis [87]. Consequently, hepatocytes experience lipotoxicity due to oxidative stress at both cellular and organelle levels which ultimately results in cell death [88].

Oxidative stress and lipotoxicity trigger the activation of other liver resident cells. Two important cell populations contributing to MASH pathogenesis are the Kupffer cells (KCs) and hepatic stellate cells (HSCs). As mentioned earlier KCs are liver resident macrophages [61]. Activation of KCs triggers the production several pro-inflammatory cytokines and chemokines which recruit macrophages, natural killer T cells, and neutrophils. Consequently, KCs together with these innate immune cells aggravate hepatic inflammation [88]. Moreover, proteins such as galectin-3 (Mac2) produced from KCs and infiltrating macrophages trigger the activation and proliferation of HSCs which results in liver fibrosis. Indeed, in a study conducted by Liu et al. KC activation in a chemically induced liver fibrosis model led to inflammation and fibrosis

[89]. Similarly, galectin-3 expression was associated with activation of HSCs and induction of liver fibrosis [90, 91].

Under normal conditions, HSC activation is an adaptive response which removes pathogens and toxins from the liver. However, in chronic diseases like MASH, factors derived from damaged hepatocytes and KC/macrophage-released cytokines and chemokines trigger the transformation of HSCs from a quiescent into an activated state [68]. Consequently, activated HSCs enhance the secretion of collagen and other ECM components, resulting in scarring and ultimately fibrosis [84, 85, 92]. It has been suggested that clearing activated HSCs can help in the resolution of fibrosis. Three mechanisms have been implicated to induce HSC clearance: apoptosis, senescence, and reversion [68]. However, long-term fibrogenesis leads to liver cirrhosis, marked by encapsulation of damaged liver tissue by a collagenous scar. This is accompanied by functional changes due to endothelial dysfunction resulting in elevated intrahepatic vascular resistance- a significant factor contributing to portal hypertension in cirrhosis [93]. Liver cirrhosis culminates in HCC which is the terminal complication of MASH. Besides liver cirrhosis, the development of HCC is also attributed to genetic predisposition and infection by hepatitis B and C viruses [94]. Current treatment options for MASH-induced HCC are limited to the removal of the underlying cause or liver transplantation. However, the demand for transplantation exceeds the availability of donor organs, making it challenging to access in many parts of the world. Therefore, it is important to target MASLD/MASH in early-stages.

1.3.3 Current therapies for MASH

Currently, there are not many FDA approved medications directly targeted against MASLD. Lifestyle modifications focusing on weight loss through a hypocaloric diet and exercise have been strongly recommended in the American Associated for the Study of Liver Diseases (AASLD) and in the European Association for the Study of the Liver (EASL) guidelines [95, 96]. Currently recommended dietary pattern for MASLD patients is the Mediterranean diet rich in vegetables, fruits, legumes, with avoidance of red meat and dairy. Observational studies and small randomized control trials have shown that the Mediterranean diet is able to reduce liver fat and improve metabolic profile in MASLD patients [97-99].

Furthermore, there are ongoing clinical trials for various agents aimed at different stages of MASLD development. These include drugs that regulate appetite and hunger, thereby targeting insulin resistance (e.g. GLP-1 receptor agonists liraglutide [100] and semaglutide [101, 102]). Other classes of drugs are targeted towards lipid metabolism (e.g. FXR agonist obeticholic acid [103]), inflammation and portal hypertension (e.g. CCR2/5 inhibitor cenicriviroc [104] and galectin-3 inhibitor belapectin [105]). In 2021, FDA approved Wegovy which is a GLP-1 receptor agonist for the treatment of chronic weight management in obesity. This drug was developed by Novo Nordisk. As described in the previous section, obesity is one of the major drivers of MASLD. Clinical trials on patients with type 2 diabetes have shown that administration of Wegovy impacted body weight gain [106]. However, the effect of Wegovy on MASLD has not been investigated so far. Additionally, the clinical trials of several other drugs targeting other aspects of MASH have been discontinued due to potential side effects or lack of efficacy [107].

1.3.4 cGMP enhancing drugs for MASH treatment

While cGMP-enhancing drugs (specifically NO-GC stimulators and activators) for the treatment of MASLD/MASH have not yet entered clinical trials, they have demonstrated protective effects in numerous mouse models. In a diseased liver, the bioavailability of NO is either limited or in excess due to oxidative stress. Therefore, the unique mechanisms of NO-GC stimulators and activators have been employed to induce cGMP generation independent of NO.

In a preclinical model of pig serum and CCl_4-induced liver fibrosis, NO-GC agonist BAY 60-2770 was well-tolerated and attenuated liver fibrosis [108]. In three different studies on experimental MASH induced via choline deficient high-fat diet (CD-HFD) feeding, treatment with NO-GC stimulators IW-1973 and praliciguat restored hepatic cGMP levels, reduced inflammation, and suppressed HSC activation and fibrosis [13, 14, 109]. In bile duct ligated cirrhotic rats, the NO-GC stimulator riociguat and PDE-5 inhibitor tadalafil improved portal hypertension and reduced fibrosis [15, 110]. Finally, a recent study with NO-GC activator BI 685509 showed reduced portal hypertension and portosystemic shunting in thioacetamide (TAA) induced cirrhosis in rats [111]. These studies highlight the importance of developing drugs that target the cGMP signalling pathway for the treatment of MASH.

1.3.5 Preclinical mouse models for MASH

Preclinical mouse models play a crucial role in examining both the mechanisms and treatment approaches in the development of MASH and the consequent HCC. These include genetically modified mice, diet-induced, and toxin-induced models of MASH [112]. Of all these models, 'Western diets' (WD) have gained increased recognition as the most effective in recapitulating the pathology and comorbidities of human MASH.

The ApoE knockout (ApoE KO) model, frequently utilized in atherosclerosis research, has also been used to study MASH. These mice are deficient in the ApoE protein, crucial for lipoprotein metabolism. Studies have shown that feeding male ApoE KO mice a WD for 7 weeks resulted in steatosis, inflammation, and fibrosis [84, 113]. The DIAMOND model (Diet-induced mouse model of MASLD) was created by a stable isogenic cross between C57BL/6J and S129 mice and feeding them a WD with sugar water for 12 months. These mice developed obesity and spontaneous MASH-HCC following after 12 months of WD [114]. Another model that closely resembles human MASH pathogenesis is the *Foz/Foz* mouse carrying a mutation in the *Alms1* gene. Ganguly et al. showed that *Foz/Foz* mice fed a high-fat/high-carbohydrate WD developed MASH and HCC [115].

Diet-induced obesity is one of the major risk factors contributing to the development of MASLD and MASH in humans. Hence, dietary-based models are considered the most suitable to faithfully mimic features of human MASH and its dynamics over time. Various dietary-based models of MASLD/MASH are available. The most commonly used is the 'Western diet' comprising of high-fat/high-carbohydrate although the exact formula of the diet can vary. A popular WD model used in the past decade was the Amylin liver MASH model (AMLN). Male C57BL/6J mice fed the AMLN diet for 30 weeks showed obesity, insulin resistance, elevated liver enzyme levels as well as histopathological features of MASH (steatosis, ballooning, fibrosis) [116]. This diet was replaced by the Gubra Amylin MASH (GAN) shortly after the ban on *trans* fats by the European Union and the FDA [112]. The choline-deficient high-fat diet (CDHFD) is predominantly made of fat and lacks choline which reduces the liver's ability to secrete very low-density lipoproteins (VLDL). This impairs lipid metabolism. Mice fed a CDHFD demonstrated a progressive body weight gain, mild fibrosis, enhanced accumulation T cells, and spontaneous HCC after 12 months of feeding [117]. Finally, the methionine choline deficient (MCD) model is known for its ability to rapidly induce liver fibrosis. However, by 8

weeks the mice lose majority of their body weight as they experience hypermetabolism [118]. This diet is considered extremely rigorous for the mice and has been discouraged as it not optimal to examine metabolic parameters of MASLD [119].

Lastly, the toxin induced models involve exposing mice to certain chemicals or substances that induce liver damage and inflammation, which in turn leads to MASLD/MASH. The choice of toxin can vary depending on the specific research goals, but commonly used substances include chemicals like carbon tetrachloride (CCl_4), streptozotocin (STZ), and diethylnitrosamine (DEN), often in conjunction with a Western diet. These models can be harsh and may impact mouse mortality rates. Most importantly, they do not phenocopy the state of obesity and features of MASH as observed in humans [112]. A more elaborate information on mouse models of MASLD/MASH can be found elsewhere [112, 119, 120].

1.4 Aim of the work

The first aim of this study was to establish and characterize a mouse model which recapitulates the characteristics of human MASH together with its comorbidity atherosclerosis. The second aim was to characterize the NO/NO-GC/cGMP signalling pathway in both healthy and MASH livers. The final aim was to test the therapeutic potential of a novel NO-GC modulating drug in MASH development.

2 Materials and methods

The following section provides a detailed description of the current study's techniques and commonly used reagents and buffers. All solutions were prepared with distilled water and the buffer pH was adjusted whenever indicated with 10 M and 1 M NaOH and HCl solutions. Subsequently, the solutions were sterilized for 20 min at 121 °C with a DX-200 autoclave (Systec.). Pipette tips, reaction tubes, and glass coverslips were sterilized under similar conditions.

2.1 Common reagents, buffers, and solutions

Table 1: Chemicals used in the present study.

Chemical	Company	Chemical	Company
Acetic acid	Sigma-Aldrich	KCl	Sigma-Aldrich
6-Aminohexanoic acid	Roth	Methanol	Sigma-Aldrich
APS	Roth	Milk powder	Roth

Bromophenol blue	Roth	$MgCl_2$. $6H_2O$	Roth
Calcium chloride	Roth	NaCl	Roth
D-glucose	Fisher	$Na_2HPO_4 \bullet 2H_2O$	Roth
Dimethyl sulfoxide	Roth	NaOH (pellets)	Roth
Direct Red 80	Sigma- Aldrich	Oil red O	Merck
EDTA. $2H_2O$	Roth	PFA	Roth
Ethanol	Sigma-Aldrich	Picric acid (1.3%)	Sigma-Aldrich
Fast green FCF Dye content	Merck	PMSF	Roth
Glutardialdehyde (25%)	Roth	SDS	Roth
Glycerol	Roth	Sodium citrate. $2H_2O$	Sigma-Aldrich
D-Glucose	Fisher	Sodium deoxycholate	Roth
Glycine	Sigma-Aldrich	D-Sucrose	Roth
HCl (37%)	Roth	TEMED	Roth
Hoechst No. 33258	Sigma-Aldrich	Tris (Trizma base)	Sigma-Aldrich
H_2O_2	Roth	Trypan Blue (0.4%)	GIBCO
HEPES	Roth	Triton X-100	Roth
Isopropanol	Sigma-Aldrich	Tween-20	Roth
$K_3Fe(CN)_6$	Merck	Xylene cyanol	Roth
$K_4Fe(CN)_6$	Roth		
KH_2PO_4	Roth		

- **cGMP-modulating drugs:**
    - **Diethylamine NONOate (DEA/NO; 100 mM):** Dissolve 50 mg DEA/NO in 2.42 ml of 10 mM ice-cold NaOH and store at -20 °C.
    - **NO-GC activator (BR11707; 10 mM):** Dissolve 3.18 mg of the activator in 617 µL DMSO. Prepare 50 µL aliquots and store at -20 °C.
- **Dulbecco's modified eagle's medium (DMEM):** DMEM high-glucose (4.5 g/l D-Glucose) GlutaMAX (containing the dipeptide L-alanyl-L-glutamine) +pyruvate (110 mg/l Na-pyruvate) (GIBCO, Cat-#31966-021). Add 10 % FBS (50 ml), 5 ml of 100x penicillin/streptomycin. Store at 4 °C.
- **2.5 M D-glucose:** Dissolve 18 g D-glucose in 30 ml of H_2O using an ultrasonic water bath set to 37 °C. Fill up to 40 ml, sterile filter through 0.45 µm filter and store at RT.
- **Imaging buffer (IB):** Dissolve 40.9 g Nacl, 1.86 g KCl, 1.22 g $MgCl_2.6H_2O$, 1.11 g $CaCl_2$, 5.96 g HEPES in 5 L ddH_2O, adjust pH to 7.4 with NaOH, autoclave, and store at RT. Add 2 ml of 2.5 M D-glucose to 500 ml IB before use.
- **Phosphate-buffered saline (PBS):** Dissolve 7.9 g NaCl, Dissolve 7.9 g NaCl, 0.2 g KCl, 1.42 g Na_2HPO_4, 0.24 g KH_2PO_4 in 1 L ddH_2O. Adjust pH to 7.4 with HCl of NaOH, autoclave, and store at RT.
- **PBS-T:** 0.1 % Triton X-100 in PBS. Stir thoroughly until dissolved and store at RT.

- **Tris buffered saline (TBS):** Dissolve 87.7 g NaCl and 12.11 g Tris in 1 L ddH_2O. Adjust pH to 8.0 with HCl and store at RT.
- **TBS-T:** 0.1 % Tween-20 in TBS. Stir until dissolved and store at RT.

2.2 Transgenic mice

The use of animal models for in *vivo* studies helps to address the shortcomings of *in vitro* studies. This is because *in vivo* studies more closely resemble the physiological situation. The present study made use of transgenic mice that carried knocked-in reporter genes and a knockout of a gene responsible for lipid metabolism. These transgenic mice enabled the characterization of MASH as well as the investigation of the role of the cGMP signalling pathway in MASH. Both male and female mice were used in the present study. All experiments were performed in accordance with the directive 2010/63/EU of the European Parliament and approved by the local Animal Care authorities (Regierungspräsidium Tübingen IB7/18G).

2.2.1 Animal diet

- **Normal diet:** Maintenance diet for mice (1324) containing 11 % fat, 24 % protein, and 65 % carbohydrates. (Altromin Spezialfutter GmbH & Co.KG, Germany).
- **Breeding diet:** Maintenance diet for mice (1314) containing 14 % fat, 27 % protein, and 59 % carbohydrates. (Altromin Spezialfutter GmbH & Co.KG, Germany).
- **High-fat diet:** Western diet (E15723-34, TD88137) containing 21 % butterfat and 1.25 % cholesterol (42 kJ% fat, 15 kJ% protein, 43 kJ% carbohydrates) from Ssniff (ssniff Spezialdiäten GmbH, Germany). The chow was delivered in vacuum sealed 5 kg packages and was stored at 4 °C. The western diet was supplemented with NO-GC activator at a concentration of 150 ppm (150 mg/kg diet).

2.2.2 Animal husbandry and mouse lines

All animals were housed at 20-24 °C and 50-60 % humidity in a 12 h light/12 h dark cycle. The animals were held in groups with up to 3 mice in a type II cage (360 cm^2) or up to 8 mice in a type III cage (810 cm^2) with bedding made of shredded aspen wood (J. Rettenmaier & Söhne GmbH + Co KG, Rosenberg, Germany). The cages were additionally equipped with wooden tunnels (Tapvei Estonia OÜ, Harjumaa, Estonia) and cellulose for nest-building. Mice had access to standard chow and tap water *ad libitum*. Mice used in this study are on a C57BL/6NCrl (B6; Charles River) genetic background. At three weeks of age, the mice were separated from their parents, ear-tagged, and genotyped as described in section 2.2.4.

Table 2: Mouse lines used in the current study. The nomenclature of the alleles is as follows: ''+'' refers to the wild-type allele, ''L1'' denotes the targeted knock-in after Cre recombination, and ''-'' refers to knockout for the endogenous allele.

Name	Systemic name	Alleles	Description	Reference
B6	C57BL/6NCrl		Wildtype mice. All mice used in the present study were on a B6 background.	RRID: IMSR_CRL:027
cGi(L1)	B6;129-Gt(ROSA)26Sor$^{tm4.1(ACTB-tdTomato,-cGi-500)Feil}$	+; L1	Global expression of cGMP biosensor cGi500 under the control of CAG promoter.	[52]
ApoE	B6.129P2-Apoe^{tm1Unc}	+; -	Genetic ablation of ApoE by deletion of the ApoE gene.	[121]

2.2.3 Generation of global cGi500 sensor mouse

To measure the cGMP levels for *ex vivo* and *in vivo* studies, Thunemann, Wen, et al. 2013 [52] have generated transgenic mice that stably express the cGMP sensor cGi500 either globally (cGi-L1) or in a specific cell type (mT/cGi-L2). These two constructs are inserted into the *Rosa26* locus driven by the ubiquitous cytomegalovirus early enhancer/chicken β-actin/β-globin (CAG) promoter. The current study made use of transgenic mice expressing the cGMP sensor cGi500 globally in all cell types (cGi-L1).

2.2.4 Mouse genotyping

It is important to examine the genetic status of experimental animals when using transgenic mouse models. For this reason, genotyping was performed for all experimental animals for the genes of interest at the age of three weeks and at the end of the experiment if required. Genotyping was performed using a polymerase chain reaction (PCR) based protocol. Using appropriate oligonucleotide primers, a defined length of DNA fragments was amplified from the genomic DNA via PCR. The amplified DNA fragments were then separated according to their length via agarose gel electrophoresis. A DNA ladder loaded together with the samples was used to determine the fragment length. The following are the materials and buffers required for genotyping.

- **DNA extraction buffer:** 1 mg/ml proteinase K (Genaxxon, CAS 39450-01-6) in 1x ''complete II KCl'' reaction buffer (BIORON).
- **Invitrogen master mix:** 20 mM Tris (pH 8.4), 50 mM KCl, 1.5 mM $MgCl_2$ (all provided with Invitrogen Taq DNA pol.), 0.2 mM of each deoxynucleotide, 0.3 μM of each primer and 0.05 U/μl Taq DNA polymerase (Invitrogen, Cat-#10342-020; final concentrations).

- **Tris borate EDTA (TBE) buffer:** Dissolve 605 g Tris, 309 g boric acid, 200 ml 0.5 M EDTA (pH 8.0) in 1 L ddH_2O. Stir thoroughly and store at RT.
- **Tris acetate EDTA (TAE) buffer:** Dissolve 242 g Tris, 57.1 ml acetic acid, 100 ml 0.5 M EDTA (pH 8.0) in 1 L ddH_2O and store at RT.
- **6x DNA loading dye:** 30 % glycerol, 0.05 % bromophenol blue, 0.05 % xylene cyanol in 66 ml 10x TBE, store at -20 °C.
- **Other buffers and chemicals:** HPLC-grade water, Midori Green Advance (NIPPON Genetics, Cat-# MG04) and 1 kb Plus DNA Ladder (Invitrogen, Cat-# 10787-018).
- After ear tagging, collect ear biopsies from mice in 1.5 ml reaction tubes. Digest the tissue samples in 50 µL DNA extraction buffer overnight at 57 °C.
- On the following day, thoroughly vortex tissue lysates, centrifuge for 5 min at 13,000 rpm, and transfer the supernatant containing the DNA into fresh tubes.
- Inactivate proteinase K for 15 min at 95 °C in a peqSTAR 2x (PEQLAB) thermal cycler. Store DNA samples at -20 °C until use.
- For performing PCR, prepare the Invitrogen master mix using the primers given in **Table 3** depending on the transgene. Add 23 µl master mix to 2 µl of DNA sample from the previous step, mix and spin down briefly.
- Place the samples in a thermocycler and run the required PCR program as mentioned in **Table 4**.
- Mix 2g agarose in 100 ml 1x TAE buffer in a short flask and bring it to a boil in a microwave until the agarose is completely solved. Cool down the solution for 15 min at RT on a magnetic stirrer, then add 2 µl of Midori green. Pour into the chamber with combs and let the gel solidify for 1h at RT.
- Add 6 µl DNA loading dye to the samples. Place the gel in an electrophoresis chamber filled with 1x TAE buffer, remove the combs, and load 12 µl DNA ladder in one well followed by 12 µl samples per well. Run the gel at 120 V for 30-35 min.
- Document the using a gel green documentation system (ChemiDoc MP, Bio-Rad).

Table 3: Genotyping primers used in the present study.

Transgene	Primer	Sequence (5'-3')	Band size
ApoE	RF115	GCCTAGCCGAGGGAGAGCCG	tg: 245 bp
	RF117	GCCGCCCCGACTGCATCT	wt: 163 bp
	RF151	AGTTCTTGTTGTGACTTGGGAG	
cGi(L1)	BB01	CTCTGCTGCCTCCTGGCTTCT	wt: 330 bp
	BB02	CGAGGCGGATCACAAGCAATA	L1: 250 bp
Cre	Cre 800	GCTGCCACGACCAAGTGACAGCAATG	tg: 402 bp
	Cre 1200	GTAGTTATTCGGATCATCAGCTACAC	wt: none

Table 4: PCR programs.

Transgene	PCR program		
ApoE	95 °C	3 min	
	94 °C	10 sec	35x
	57 °C	30 sec	

	72 °C	30 sec	
	72 °C	10 min	
	95 °C	5 min	
cGi(L1)	95 °C	10 sec	35x
	61 °C	30 sec	
	72 °C	30 sec	
	72 °C	5 min	
	95 °C	5 min	
Cre	95 °C	10 sec	35x
	58 °C	30 sec	
	72 °C	30 sec	
	72 °C	5 min	

2.2.5 Establishment of MASH mouse model

A genetic approach in combination with a high-fat diet was used to develop MASH in mice. MASH does not develop naturally in mice but interfering with their lipoprotein metabolism is known to cause hypercholesterolemia and obesity eventually leading to MASH. A commonly used genetic mouse model for MASH is the ApoE-deficient mice (ApoE KO) with a high-fat diet [84, 113]. In the current study, ApoE KO mice together with a high-fat and high cholesterol diet were used. ApoE KO mice were fed a normal chow diet (NC) until 10 weeks of age after which the NC diet was replaced by HFD (as mentioned in section 2.2.1) for 18 weeks. To study the pharmacological modulation of cGMP signaling in MASH, ApoE KO mice were fed a HFD mixed with NO-GC activator compound from Bayer for 18 weeks **(Figure 9)**. Subsequently, the mice were sacrificed, and liver tissue and blood samples were collected. Features of MASH were analysed via tissue, plasma, and histology analysis.

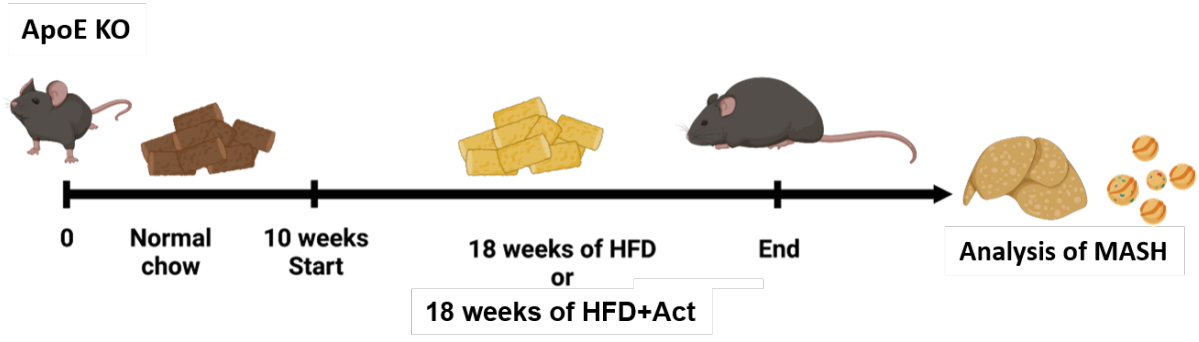

Figure 9: Schematic overview of the feeding timeline. Starting from the age of 10 weeks, ApoE KO mice were fed either a high-fat diet (HFD) or HFD mixed with NO-GC activator (HFD+Act) for a period of 18 weeks. At the end of the feeding timeline, mice were sacrificed, and liver tissue and blood samples were collected to analyse MASH. The figure is created using Biorender.com.

2.3 Analysis of primary murine HSCs in culture

To analyse cGMP signalling in cultured HSCs, primary HSCs were isolated from the livers of wild-type and transgenic mice. The isolation protocol was adapted from Mederacke et al. 2015 [65]. Old male mice (30-40 weeks of age) were used for isolation due to the high yield of cells. To analyse both the early and late stages, HSCs were cultured on coverslips for a period of 8 days with day 2 representing the early stage and day 8 representing the late stage.

2.3.1 Isolation and cultivation of primary HSCs

A wide range of equipment, reagents, and enzymes are used in the isolation procedure of primary HSCs from mouse liver. The list of equipment and the reagents with their final concentrations are given in supplementary tables I-V. All reagent solutions can be made ahead and stored at 4 °C for up to 6 months. The required solutions and buffers are listed below.

- **EGTA solution:** Prepare the EGTA solutions by dissolving the components from **(Suppl. Table I)** in 500 ml of ddH_2O. Adjust the pH to 7.35-7.4 using 10 M HCl and filter the solution through a 0.2 μm bottle top filter before use. The solution can be stored at 4 °C for up to 6 months.
- **Enzyme buffer solution:** Prepare the enzyme buffer solution by dissolving the components from **(Suppl. Table II)** in 500 ml of ddH_2O. Stir the solution for 30 minutes before slowly adding calcium chloride dihydrate ($CaCl_2.2H_2O$). Adding $CaCl_2$ before thoroughly mixing the solution will lead to the precipitation of salts from the solution. Adjust the pH to 7.35-7.4 and filter the solution through a 0.2 μm bottle top filter before use. The solution can be stored at 4 °C for up to 6 months.
- **Gey's Balanced Salt Solution A (GBSS/A):** Prepare the solution by dissolving the components from **(Suppl. Table III)** in 500 ml of ddH_2O. Adjust the pH to 7.35-7.4 and filter the solution through a 0.2 μm bottle top filter before use. The solution can be stored at 4 °C for up to 6 months.
- **Gey's Balanced Salt Solution B (GBSS/B):** Prepare the solution by dissolving the components from **(Suppl. Table IV)** in 500 ml of ddH_2O. Adjust the pH to 7.35-7.4 and filter the solution through a 0.2 μm bottle top filter. The solution can be stored at 4 °C for up to 6 months.

All the enzyme solutions must be prepared fresh shortly before starting the isolation procedure.

- **DNase I:** Prepare DNase I by dissolving 100 mg in 50 ml of GBSS/B by gently pipetting since DNase is prone to physical denaturation. This should be aliquoted and stored at -20 °C until use. The aliquots are stable up to 18 months.
- **EGTA solution:** Aliquot 35 ml of EGTA solution per mouse through a 0.2 μm bottle top filter.

- **Pronase E solution** (Merck, Darmstadt, Germany) **(per mouse):** Dissolve 0.014 g of pronase E in 35 ml enzyme buffer solution by filtering through a 0.2 μm bottle top filter under a sterile cell culture hood.
- **Collagenase D solution** (Roche, Indianapolis, IN, USA) **(per mouse):** Dissolve 0.0148 g of collagenase in 40 ml of enzyme buffer solution by filtering through a 0.2 μm bottle top filter under a sterile cell culture hood.
- **Pronase/collagenase solution (per mouse):** Dissolve 0.025 g of pronase E and 0.0175 g of collagenase D in 50 ml of enzyme buffer solution by filtering through a 0.2 μm bottle top filter under a sterile cell culture hood. Add 1% DNase I shortly before adding the minced liver.
- **Histodenz solution** (Sigma-Aldrich, St. Louis, MO, USA)**:** Dissolve 4.95 g of histodenz in 15 ml of GBSS/A by vortexing thoroughly. Once dissolved, fill up the volume to 17 ml and filter through a 0.2 μm syringe filter. Store the solution at 4°C until mixing with HSCs.

The isolation protocol is split into four parts. **(Figure 10)** shows a schematic overview of HSC isolation from mouse liver. Adjust the flow rate of the perfusion pump to 5 ml/min using ddH_2O. Empty the perfusion line and fill up the system with EGTA solution. Before the start of the procedure, all the enzyme solutions (EGTA, pronase, collagenase, and pronase/collagenase) must be heated up in a water bath set to 42 °C. Set the centrifuge to 4 °C.

Part I: *In situ* pronase/collagenase perfusion of mouse liver (Timing: 20 min)

- Fix the upper and lower extremities of an anesthetized mouse on a dissecting board using tape and conduct a laparotomy to expose the liver and inferior vena cava (IVC).
- Expose the IVC by moving the visceral organs to the right side and cannulate the IVC with the 22G needle attached to the perfusion line.
- Start the pump and perfuse the mouse liver first with EGTA solution. Wait and cut the portal vein once it is distended. Perfuse with EGTA for 2 min.
- The liver becomes pale if the initial perfusion is done properly and once the portal vein is severed.
- Switch from EGTA to pronase solution and perfuse the liver for 5 min. (Caution: Turn off the pump while switching between solutions to avoid air bubbles)
- Switch from pronase to collagenase solution and perfuse the liver for 7 min.
- Detach the catheter from the IVC. Transfer the liver into a sterile petri dish containing 5 ml of pronase/collagenase solution.
- Mince the liver gently under a sterile bench using forceps. The liver should appear completely fluid without any residual chunks after *in situ* perfusion.

Part II: *In vitro* digestion (Timing: 50 min)

- To the prewarmed pronase/collagenase solution, add 1% DNase I. Transfer the minced liver into a small conical flask with pronase/collagenase solution containing 1% DNase I. Place the mixture on a stir plate set to 40 °C for 20 min.
- Using a 70 μm cell strainer, filter the digested mouse liver into a 50 ml falcon tube and centrifuge the mixture at 580 g for 10 min at 4 °C.
- Aspirate the supernatant leaving behind 10 ml in the tube and add 120 μl of DNase I and gently resuspend with a 10 ml pipette to avoid air bubbles. Fill up to 50 ml with filtered GBSS/B, mix by inverting, and centrifuge again at 580 g for 10 min at 4 °C.

Part III: Density gradient centrifugation (Timing: 60 min)

- Aspirate the supernatant leaving behind 10 ml in the tube and add 120 μl of DNase I and gently resuspend with a 10 ml pipette avoiding air bubbles.
- Fill up to 32 ml with GBSS/B and then add 16 ml of histodenz solution. Mix thoroughly by pipetting and inverting. Distribute 12 ml of cell-histodenz solution into four 15 ml falcon tubes.
- Tilt the tubes to dampen the walls to allow the overlay. Gently overlay the cell-histodenz suspension with 1.5 ml of filtered GBSS/B using a 2 ml syringe with a 26 G needle. Centrifuge the mixture at 1380 g for 17 min at 4 °C (without break; set acceleration to 4).
- Towards the end of centrifugation, the HSCs are visible as a thin white layer at the interface between the cell-histodenz solution and the GBSS/B overlay. Using a 1 ml pipette, carefully collect the HSC layer and transfer it into a 50 ml falcon tube. Repeat the process with the remaining 15 ml falcon tubes.
- Fill up to 50 ml with filtered GBSS/B and gently pipette to resuspend the HSCs and centrifuge at 580 g for 10 min at 4 °C.

Part IV: Cell culture

- Remove the supernatant and resuspend the cell pellet in 1 ml of DMEM medium supplemented with 10 % FBS.
- Count the viable number of cells with a Neubauer chamber (18 μl cell suspension, 2 μl trypan blue). Dilute the cell suspension to 3 x 10^4 cells/ml with the full medium.
- Seed 1ml per well of a 24-well plate containing 12 mm glass coverslips.

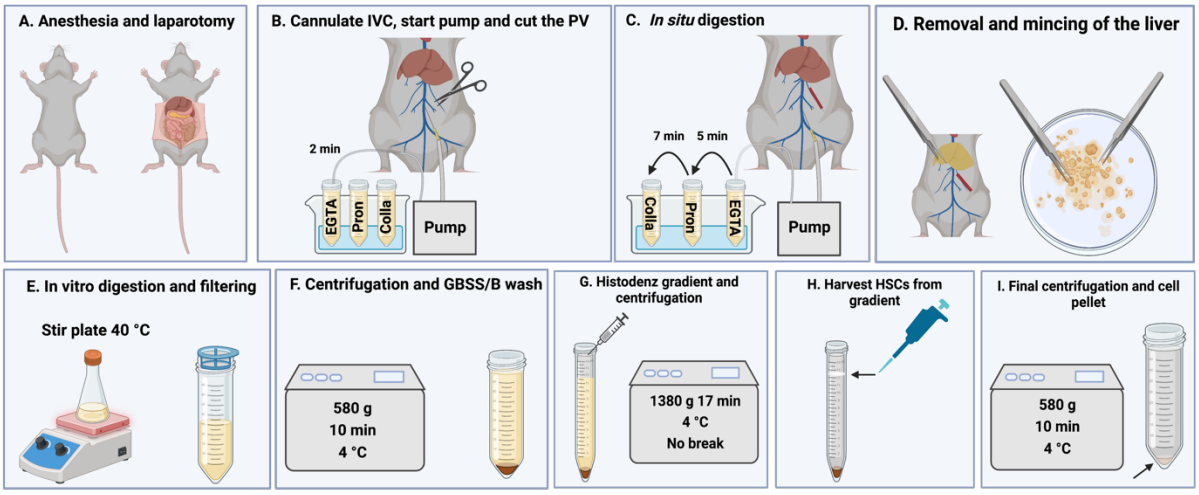

Figure 10: **Overview of isolation of primary HCSs from mouse liver. A.** Laparotomy of an anesthetized mouse. **B.** IVC is cannulated, the pump is started, and the PV is severed. **C.** In situ digestion of the liver with pre-warmed EGTA, pronase, and collagenase. **D.** Digested liver is excised and minced in a petri dish with pronase/collagenase solution. **E.** In vitro digestion of the liver in pronase/collagenase solution on a hot plate and filtering. **F.** Centrifugation followed by GBSS/B wash. **G.** GBSS/B is overlayed on cell-histodenz mixture followed by density gradient centrifugation. **H.** HSCs are harvested from the white ring at the gradient interface. **I.** Final centrifugation and the cell pellet (indicated by arrows) containing HSCs can be used for cultivation. The figure is created using Biorender.com.

2.3.2 Detection of vitamin A containing lipid droplets in HSCs

Vitamin A containing lipid droplets (= retinoids) in primary cultured HSCs were detected by their autofluorescence using fluorescence microscopy (excitation at 340 nm and emission > 480 nm; see **Table 5** for filterset). To detect the autofluorescence of vitamin A in liver tissues, excised livers should be cut into slices and incubated in 3.7 % formaldehyde in the dark for 24 hours at 4 °C. 20 µm thick liver sections can be examined as described above for cultured HSCs. Due to the light-sensitive nature of vitamin A autofluorescence, exposure with excitation light should be kept at minimum (intensity/timewise).

2.3.3 Immunofluorescence staining of primary HSCs

To analyse the expression of cGMP pathway proteins, immunofluorescence staining was performed on primary HSCs on glass coverslips. Firstly, the HSCs were fixed at three different time points (Day 1, 4, and 8) to analyse the expression as they transitioned from early to intermediate to late stages. The staining was performed at the end to have comparable results. Antibodies used for IF staining are listed in the supplementary table VI.

- **Cell fix:** 3.7 % formaldehyde in PBS.

- **Wash buffer (0.5 % bovine serum albumin (BSA) in PBST):** Dissolve 0.25 g of BSA in 50 ml of PBST and store at 4 °C for up to 2 weeks.
- **Blocking buffer:** 5 % normal goat serum (NGS) in wash buffer
- **Antibody solution:** Prepare both primary and secondary antibody solutions (pAb, sAb) in wash buffer. Centrifuge both pAb and sAb solution at 13,000 rpm for 5 min.
- Wash cells twice with PBS. Transfer the glass coverslips to a fresh 24 well place and fix the cells using cell fix for 10 min at RT. Wash the cells once with wash buffer and store the coverslips at 4 °C until staining. (Tightly seal the plate with parafilm to avoid any contamination). If staining is to be continued immediately, follow the steps given below.
- Post fixation, block and permeabilize the cells with the blocking buffer for 10 min at RT.
- Place a sheet of parafilm in a moist chamber. Pipette ~70 µl of pAb and place the coverslips with cells facing the parafilm. Incubate overnight at 4 °C.
- On the following day, wash cells twice with the wash buffer with each wash lasting for 3 min at RT. Incubate cells with ~70 µl sAb in the dark for 1 hour at RT.
- Wash cells twice with PBS for 3 min each. Dip the coverslip once in distilled water to remove any precipitates and mount on glass slides with the DAPI mounting medium (ROTI®Mount FluorCare DAPI, Roth).
- Let the coverslips dry overnight at RT and document the staining with an inverted epifluorescence microscope (Axiovert 200, ZEISS).

The microscope (Axiovert 200, ZEISS) was equipped with a Plan NeoFluar 10x/0.30 objective (ZEISS) and an electron-multiplying charged-coupled device (EM-CCD) camera (Retiga 2000R, QImaging). The computer-controlled Oligochrome (TILL Photonics) equipped with a Xenon short-arc lamp (UXL-S150MO, Ushio) and a set of excitation filters (AHF) was used as the light source. The combination of excitation filters together with emission filters and dichroic mirrors facilitated the detection of specific fluorophores **(Table 5)**.

Table 5: Filter combinations used to detect different fluorophores.

Fluorophore		Excitation filter	Dichroic mirror	Emission filter
Hoechst 33258		BR 387/11	410 DCLP	LP 440
YFP, Alexa 488		BR 497/16	516 DCLP	BR 535/22
FRET	CFP	BP 445/20	470 DCXRUV	BP 480/50
	YFP		+ 516 DCLP	BP 535/40

2.3.4 cGMP/FRET measurements in cultured HSCs

For cGMP/FRET measurements, HSCs from transgenic mice expressing the cGMP biosensor cGi500 globally (cGi (L1)) were used. To analyse the intracellular cGMP levels, HSCs were isolated and cultivated on 12 mm glass coverslips in a 24-well plate. HSCs were cultured in full

medium (DMEM with 10 % FBS and penicillin/streptomycin) and were cultivated for a period of 8 days. The cGMP signals were recorded after day 1 and day 7. For recording the ratio metric cGMP/FRET signals, a beam splitter with 05-EM insert (Micro-Imager DUAL-View, Photometrics) in front of the EM-CCD camera was used. This allowed for the separation of CFP and YFP emissions for simultaneous recording. It contained a dichroic long pass mirror (516 DCLP) and two emission bandpass filters (BP 480/50 [for CFP emission] and BP 535/40 [for YFP emission]). The adjustable mirrors and shutters allowed for the manipulation of the light path such that half of the camera sensor was exposed to YFP emission while the other half was exposed to CFP emission.

The coverslip with cells was mounted into a superfusion system and the cells were constantly superfused with IB during the measurement. The system was equipped with a fast-performance liquid chromatography pump (Pharmacia P-500, GE Healthcare), fast-performance liquid chromatography injection valves (Pharmacia V-7, GE Healthcare), a vacuum pump (Laboport N86, KNF Neuberger), a 2 ml sample loop, tubing (Tygon S3 E-3603, Saint-Gobain), a superfusion chamber for holding the 12 mm coverslips (RC-25, #64-0232, Warner Instruments) attached to a magnetic chamber holder (PM-1, #64-1526, Warner Instruments), and a pen that can be heated to pre-warm the buffer during superfusion (TC-344C Dual automatic temperature controller, Warner Instruments).

A typical FRET measurement lasted for 50-60 min, and it was crucial to minimize the photobleaching of the biosensor. This was done by reducing the exposure time and increasing the acquisition time between two cycles. The signal of several pixels was summed up (binning) to improve the signal-to-noise (SNR) ratio at low exposure times. This improved the quality of FRET signals. The following settings were used for cGMP/FRET measurements with HSCs: 4x4 binning, 300 ms exposure time, 10x magnification, 5 sec cycle time, and a flow rate of 1 ml/min.

Switch on the microscope and the light source 30 min prior to the start of the experiment. Pre-dilute the DEA/NO stock solution 1:1000 in 10 mM NaOH and store it on ice. Thaw remaining drugs to be tested on ice.

- Perform solvent change by flushing the perfusion system with IB including the sample loops. Make sure that both the valves are on load position.

- Before starting the measurement, align the CFP and YFP channels of the beam splitter using a calibration grid (Photometrics).
- Assembling the superfusion chamber:
    a. Coat the back of the chamber and the chamber holder with a thin layer of silicon grease. Remove excess silicon with a cotton bud. Place the coverslip with cells onto the chamber with cells facing inwards. Flip the chamber upside down, press onto the holder, and cover the cells immediately with IB. Secure the chamber with metal plates and wipe the bottom of the coverslip with 70 % ethanol.

    b. Place the chamber holder onto the microscope stage and attach the inlet and the outlet needle to the chamber.

- Begin superfusion and vacuum. Adjust the level of the outlet needle until a constant buffer flow is achieved.
- Visualize and examine the cells first through the eyepiece using the YFP filter set. Find an appropriate region consisting of good cell density and a cell-free region for the background correction.
- Switch to camera mode and acquire three snapshots in the following order: brightfield (1x1 binning, 2-sec exposure, brightfield filter set), Retinoids (1x1 binning, 2-sec exposure, FURA-380 filter set), and YFP (1x1 binning, 2-sec exposure, YFP filter set).
- Switch to the FRET filter set and adjust the measurement settings to 4x4 binning, 300 ms exposure, and 5-sec cycle time. Start measurement and draw ROIs around ~5 cells and a background region. Prepare the drugs by diluting them to their final concentration in IB.
- Record 30 frames before the first drug application. Load the sample loop with the first drug and apply the drug by switching the loop from load to inject. Note the frame number when the drug is applied and stop the application after 30 frames.
- Wash the loop 3x with IB and wait until the signals are back to baseline before applying the next drug. Continue measuring until all drugs have been applied.
- After the final recordings are done, stop the measurement. Detach the inlet and the outlet needle from the chamber, remove the chamber from the stage, and perform solvent exchange using 70 % ethanol to clean the system.
- Discard the coverslip and turn off the microscope.

2.3.4.1 Quantification of cGMP/FRET imaging

The images acquired during cGMP/FRET measurement were first analysed with Fiji to obtain the background corrected fluorescence signals. This data allowed us to calculate the cGMP/FRET signals using MS Excel and OriginPro software. The analysis can be summarized into four simple steps:

- The regions/cells of interest were identified.

- For every time point in the YFP and CFP image, the mean fluorescence intensity was assessed and corrected for background signals.
- From this data the cGMP/FRET signals (CFP/YFP ratio) were calculated and normalized to baseline.
- cGMP/FRET signals in the ratio trace were verified to be true.
- **Fiji analysis**
    - Open snapshot series (1x1 binning) and apply ''Z Project: Average intensity''. This can be found under Image -> stacks -> Z Project. This creates an average image and makes the cell borders easily recognizable.
    - Adjust the brightness/contrast of the average image. Using a drawing tool mark the outline of all cells with the region of interest (ROI) and press ''Ctrl T'' to add to the ROI manager. Repeat this process until all cells are marked. In the end, place a circular ROI in a region with no cells and label as background. Save ROI set.
    - Open the CFP and YFP image stacks together with the corresponding ROI set matching the binning. From the ROI window, use ''Multi Measure: mean gray value'' to determine the mean fluorescence intensity of all ROIs for all time points.
- **MS Excel analysis**
    - Import the ''mean gray values'' in MS Excel. The cGMP/FRET ratios are calculated using a macro kindly provided by Dr. Martin Thunemann. In a nutshell, the mean fluorescence intensities are corrected for background signals.
    - The CFP/YFP ratio is built and is normalized to the baseline (R~[cGMP]). This ratio represents the cGMP concentration. The single traces of CFP and YFP fluorescence are also normalized to the baseline which describes the signal change relative to baseline.
- **OriginPro analysis**
    - The single traces and cGMP/FRET signals are evaluated using OriginPro. All ratio traces together with the corresponding single traces are plotted in separate graphs together with the drug applications.
    - An increase of CFP fluorescence with a concomitant decrease of YFP fluorescence is regarded as a real cGMP/FRET signal. The signals of all cells are examined based on this criterion to distinguish real signals from artefacts.
    - Using the Savitzky-Golay filtering method, the R (cGMP) traces are smoothened. Excessive smoothing can influence signal shapes. Therefore, depending on the signal-to-noise ratio, a smoothing window of 10-30 points is considered appropriate.

- Finally, using the ''Peak Analyser'' tool of OriginPro, calculate the area under the curve (AUC) and peak height (relative R [cGMP] change) for each signal.

2.4 Analysis of murine liver tissue and plasma

Livers isolated from control and experimental animals were analysed in detail via different techniques such as histology, immunostaining, RT-PCR, and western blotting. A stepwise procedure for each of these techniques are described in the following sections. The plasma of MASH mice was analysed to get an overview of certain liver enzyme levels that are normally upregulated in MASH. The parameters assessed were as follows: triglycerides, cholesterin, LDL, aspartate aminotransferase (AST), and alanine aminotransferase (ALT).

2.4.1 Tissue preparation for histology

Liver tissue histology was performed to characterize MASH and to locate the expression of cGMP pathway proteins. Once the mouse was sacrificed, the liver was excised, and the liver lobes were divided to be used for protein analysis and histology. For histology experiments, the right, quadrate, and caudate lobes of the liver were used while the left lobe was for western blotting **(Figure 11)**. The following two sections describe paraffin and frozen sectioning in detail.

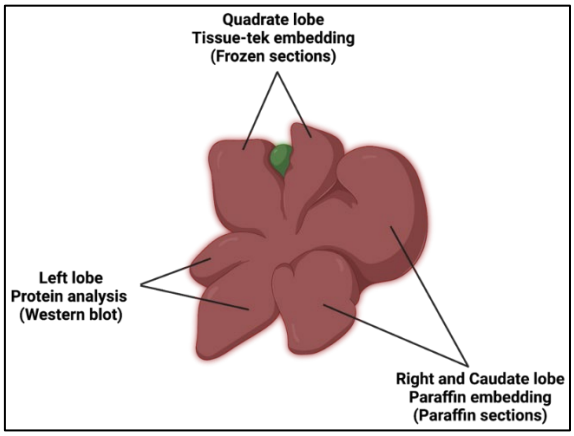

Figure 11: Liver lobes used for histology. After excising, the liver was dissected into three different parts. The right and caudate lobes were used for paraffin embedding, the quadrate lobe was used for tissue-tek embedding and the left lobe was frozen in liquid nitrogen for western blot analysis. The figure is created using Biorender.com.

2.4.1.1 Paraffin embedding and sectioning (paraffin sections)

Paraffin embedding is a standard technique used to prepare formalin-fixed, paraffin-embedded (FFPE) blocks of tissue. In short, the tissue is fixed, processed, and embedded in paraffin to create a paraffin block. Using a microtome, the paraffin block is cut into thin

sections. The sections are stored at RT and used for immunohistochemistry staining and other histological analysis [122].

- **General materials needed for embedding:** 4 % paraformaldehyde (PFA), ethanol concentration row (70 %, 80 %, 95 %, 100 %), toluene, paraffin (Surgipath Paraplast X-tra; Leica; melt and keep at 56 °C), embedding cassettes and molds, microtome (Leica), low-profile disposable blades (DB80LS; Leica), and polysine glass slides (Menzel).

- **Tissue fixation and dehydration:**
    - Fix the dissected liver lobes in 4 % PFA at RT for 3 hours. After fixing, wash the tissues in PBS three times for 15 min each.
    - Label embedding cassettes using a pencil, place the tissues in the cassettes, and dehydrate using an increasing ethanol concentration row in the following order at RT. (70 % EtOH- 30 min, 80 % EtOH- 30 min, 95 % EtOH- 30 min, 100 % EtOH- 45 min, toluene- 10 min).
    - After the last step, drop the tissue cassettes into molten paraffin and incubate overnight at 56 °C. On the following day, transfer the tissue cassettes to a new paraffin solution and incubate them overnight at 56 °C. Repeat this step one last time on the following day.

- **Embedding and sectioning (Figure 12)**
    - Remove the tissue from the cassette and choose an appropriate mold depending on the size of the tissue.
    - Place the mold on a hot plate and pour a small amount of paraffin into the mold. Orientate the convex side of the liver facing downward.
    - Transfer the mold onto ice and wait until the bottom starts to solidify. Place the embedding ring on top and fill it up with paraffin.
    - Leave the molds on ice until the paraffin solidifies. Carefully detach the embedding ring from the mold. Store the tissue blocks at 4 °C.
    - The tissue blocks were cut into 10 μm thick paraffin sections using a microtome. The sections were briefly stretched by placing them in a water bath set to 40 °C and were mounted onto adhesive Polysine glass slides After mounting, the slides allowed to dry overnight in a 37 °C incubator and stored at RT until further processing.

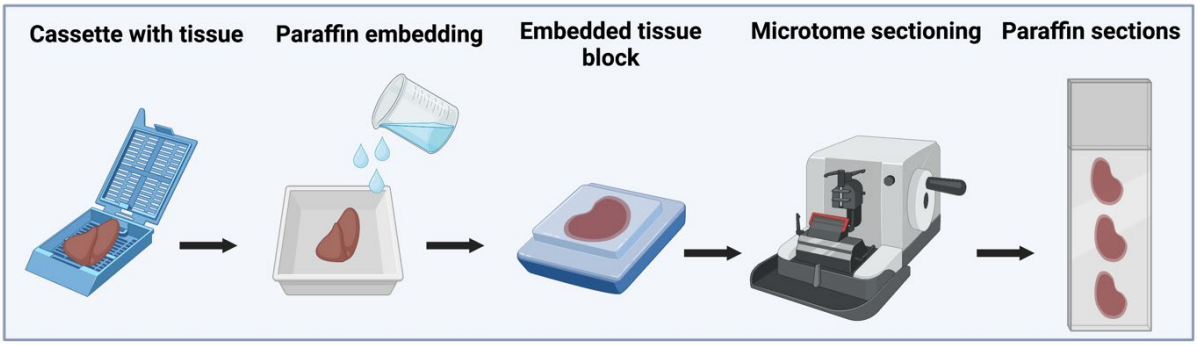

Figure 12: Embedding of liver tissue in paraffin for preparation of histological sections. Liver tissue was transferred from the cassette into the embedding mold. Molten paraffin was poured, and the block was allowed to solidify on ice. The embedded block was sectioned using a microtome and the liver sections were mounted on a polysine slide for staining. The figure is created using Biorender.com.

2.4.1.2 O.C.T embedding and sectioning (frozen sections)

Cryosectioning, also known as frozen sectioning, is a technique used for microscopic analysis of a tissue section via immunofluorescence staining. The procedure involves rapid freezing of tissue samples, which reduces any morphological damage.

- **General materials needed for embedding:** 4 % PFA, 30 % sucrose in PBS, silicone embedding molds, optimal cutting temperature compound (O.C.T ™, Tissue-Tek®), and dry ice.
- **Tissue fixation and preservation:** Fix the dissected liver for 3 hours at RT. Briefly wash the tissues for three times in PBS (15 min each). Preserve the tissues in 30 % sucrose overnight at RT to ensure cryoprotection.
- **Embedding and sectioning:**
    - Add a small amount of O.C.T. in the silicone embedding mold and place the liver tissue. Fill up the mold with O.C.T. and place the block on dry ice to ensure rapid freezing. (Rapid freezing is crucial as slow freezing leads to the formation of ice crystals which damage the tissue structure).
    - Once frozen, detach the O.C.T. block from the tissue mold and wrap it in aluminum foil. Store the O.C.T blocks at -20 °C until sectioning.
    - Turn on the cryotome a day before sectioning. For the liver, an optimum temperature of -21 °C yields good-quality flat frozen sections.
    - Cut 10 µm thick liver sections and mount them on Superfrost™ Plus Adhesion Microscopic Slides. Store the slides at -20 °C until immunostaining.

2.4.2 Histological staining of liver tissue sections

The histopathology of MASH was analysed via oil red o (steatosis), hematoxylin and eosin (hepatocyte ballooning), and picrosirius red with fast green (fibrosis) staining.

2.4.2.1 Oil red O staining (ORO)

Oil Red O staining is used to assess hepatic steatosis which is the abnormal accumulation of fat in the liver. Oil Red O is a fat-soluble dye that stains neutral lipids and cholesteryl esters [123].

- **General materials needed for staining:** Frozen liver sections, 99 % isopropyl alcohol, oil red o (MN 61; Macherey-Nagel), ddH_2O, Mayer's hematoxylin (Carl Roth), 45 µm syringe filter.
- **Oil red O stock solution:** 2.5 g of Oil Red O in 400 ml of 99 % isopropyl alcohol, mix by magnetic stirring for 1 hour at RT, and store at RT for up to 6 months.
- **Oil red O working solution:** Mix 351 ml of Oil Red O stock with 234 ml ddH_2O and filter the solution through a 45 µm filter (Use the solution within 6 hours).
- **Staining procedure:**
    - Thaw frozen liver sections at RT for ~15 min and wash the sections in PBS for 15 min to remove O.C.T.
    - Incubate sections in Oil Red O working solution for 5 min at RT. Briefly wash by dipping the sections in tap water twice.
    - Incubate the sections in hematoxylin for 15 sec to stain the nuclei. Dip sections in tap water to remove hematoxylin and develop the hematoxylin stain under running tap water for 10 min.
    - Remove excess water and mount the slides using a water-soluble mounting medium (Aquatex) and let the mounting to dry for at least 1 hour before documenting.
- **Image documentation:**

Liver sections should be photographed within 24 hours after staining. Oil Red O staining was documented using an upright epifluorescence microscope (Axioskop 20, ZEISS) equipped with an A-Plan 5x/0.12, an A-Plan 10x/0.5x and Plan NeoFluar 20x/0.5 objective (ZEISS). An EOS 750 D (Canon) digital camera mounted with a 1.6x lens was used for image acquisition. The camera was controlled using the EOS utility software and the images were documented in brightfield.

- Set up Koehler illumination [124, 125]. Gently clean the glass slide and coverslip with 70 % ethanol.
- Inspect the staining through the eyepiece and adjust the brightness of the light source and the exposure time.
- Switch to the camera and apply the white balance in an empty region on the slide.
- Using BF and 20x magnification document three to four regions per slide.

2.4.2.2 Hematoxylin and eosin (H&E) staining

H&E staining was used to analyse hepatocyte ballooning which is the swelling and enlargement of hepatocytes. H&E staining is a standard procedure for pathological diagnosis. It combines two histological stains – hematoxylin which stains the nucleus and eosin which stains the cytoplasm.

- **General materials needed for staining:** Mayer's hematoxylin (Carl Roth), Eosin G (Carl Roth), paraffin liver sections with 10 µm thickness, ddH_2O, tap water, toluene, ethanol concentration row, and DPX mounting medium (Sigma-Aldrich).
- **Staining procedure:**
    - Dry paraffin sections overnight in a 37 °C oven. Deparaffinize and rehydrate the sections in the following sequence. (Toluene- 5 min, 100 % EtOH- 40 sec, 95 % EtOH- 20 sec, 80 % EtOH- 20 sec, tap water- 2min).
    - Stain sections with Mayer's hematoxylin for 10 min at RT. Develop the staining under running tap water for 10-12 min. Rinse sections in 95 % EtOH by dipping two times.
    - Stain with eosin G for 40 sec. Rinse in 95 % EtOH to remove excess eosin staining. Dehydrate sections in 100 % EtOH for 2 min and clear in toluene for 1 min.
    - Mount the slides using DPX mounting medium and let them dry overnight before documenting.
- **Image documentation:**

H&E staining was documented using the same set up which was utilized for oil red o staining. In this case, the A-Plan 10/0.5x objective was used. As for the region of interest (ROI), a hexagonal region was selected with a central vein (pericentral) in the middle and portal veins (periportal) at the periphery. Enlarged hepatocytes and fat bubbles were mostly concentrated in the periportal region.

- **Quantification of lipid vacuoles:**
    - Open an image in Fiji and calibrate the using pixel/µm values. For 10x magnification, 4.304 pixels/µm was used.
    - Use the BIOP SimpleColorBalance to perform a white balance. Count the lipid vacuoles manually using the cell counting tool in Fiji.
    - Three ROIs per mouse with fat vacuoles around 3 portal veins per region should be counted.
    - Calculate the average number of vacuoles from all three regions and plot it in a bar graph.

2.4.2.3 Picrosirius Red/Fast Green staining (PSR/FG)

Sirius red/fast green staining is used to analyse hepatic fibrosis which is caused due to excess collagen deposition in the liver in response to chronic and repeated liver cell injury. To analyse fibrosis, Picrosirius red dye is widely used due to its specificity in detecting most collagen fibers [126]. In the present study, Sirius-red was combined with Fast Green staining. This allowed for clear detection of collagen fibers that stood out from the green-stained non-collagen compounds, resulting in high sensitivity in terms of both qualitative and quantitative analysis of collagen fibers. The staining procedure was adapted from [127].

- **General materials needed for staining:** Paraffin liver sections (10 µm), Direct Red 80 (Sigma-Aldrich), Fast Green FCF Dye Content (Merck), picric acid, acetic acid, toluene, ethanol concentration row, and DPX mounting medium.
- **Fast Green solution:** Dissolve 0.2 g Fast Green in 500 ml ddH_2O, mix and store at RT (can be re-used).
- **Fast Green/Sirius Red solution:** Direct red 0.5 g, Fast Green 0.2 g in 500 ml picric acid, mix and store at RT (can be re-used).
- **Acidified water:** 5 ml acetic acid in 1000 ml ddH_2O, mix and store at RT.
- **Staining procedure:**
    - Dry paraffin sections overnight in a 37 °C oven. Deparaffinize and rehydrate the sections in the following sequence. (Toluene- 5 min, 100 % EtOH- 3 min, 90 % EtOH- 1 min 30 sec, ddH_2O- 1 min 30 sec).
    - Incubate sections in Fast Green Solution for 15 min at RT and wash briefly with ddH_2O for 1 min 30 sec.
    - Stain sections with PSR/FG Solution for 1 hour at RT. Wash sections by dipping in two changes of acidified water for 30 sec each.
    - Dehydrate in 100% EtOH for 2 min and clear in toluene for 1 min.
    - Mount slides using DPX mounting medium and allow them to dry overnight before documentation.
- **Image documentation:**

PSR/FG staining was documented using the same set up which was utilized for ORO and H&E staining. In this case, the A-Plan 10/0.5x objective was used. As for the region of interest (ROI), a hexagonal region was selected with a central vein (pericentral) in the middle and portal veins (periportal) at the periphery. Three to four ROIs were documented per slide.

- **Quantification of collagen positive area:**

- Open an image in Fiji and calibrate the using pixel/μm values. For 10x magnification, 4.304 pixels/μm was used. Use the BIOP SimpleColorBalance to perform a white balance on the image.
- Split the BF image into three channels using ''Image ->color->split channels'' and use the green channel for further analysis.
- Select ''Threshold'' and adjust the threshold until only PSR+ area is visible. Note the threshold and keep this constant for all the images to be analysed. Once set, apply the threshold.
- Use ''Analyse Particles'' with the additional option ''Exclude on edges'' on the threshold image to mark the PSR+ area with ROI and combine with the ''OR'' function. Rename value as **''area1''**.
- Invert the image and use ''Analyse Particles'', deselect ''Exclude on edges'' to mark the PSR-negative area on the section that is surrounded by the PSR+ area. Combine ROIs with ''OR'' and rename them as **''holes1''**.
- Invert image again, select ''holes1'' and use ''Analyse Particles''. This marks the PSR+ area within the holes. Combine ROIs with OR as ''area2''.
- Invert image, select **''area2''** and use ''Analyse Particles''. Combine ROIs with ''OR'' and rename as **''holes2''**.
- It is important to exclude the PSR-negative area from PSR+ area. Combine **''area1''** and **''holes1''** with ''XOR'' as ''staining1'' and **''area2''** and **''holes2''** with ''XOR'' as ''staining2''.
- Combine **''staining1''** and **''staining2''** with ''OR'' as ''PSR+ area''. This gives the complete ''PSR+ area''.
- Repeat this procedure with all PSR/FG-stained images.
- At the end using the ''rectangle tool'' in Fiji mark the whole image and measure the area. This gives the total area of the image.
- Calculate the percentage of PSR positive area using the following formula:

$$Percentage\ of\ PSR\ positive\ area = \frac{PSR\ positive\ area}{total\ area} \times 100\ [\%]$$

2.4.3 Immunostaining of liver tissue sections

To investigate the expression pattern and distribution of different marker proteins as well as the proteins of the cGMP pathway in MASH livers, immunohistochemistry (IHC) and immunofluorescence (IF) staining were performed. The following sections below describe the procedure and quantification of IHC and IF staining.

2.4.3.1 Immunohistochemistry (IHC)

IHC was performed on paraffin liver sections. This technique involves the specific binding between an antigen and an antibody to detect and locate specific proteins in cells and tissues.

The protein or antigen was unmasked via antigen retrieval and detected by a pAb which in turn was bound by biotinylated sAb. An enzymatic reaction was used for detection. H_2O_2-dependent oxidation of DAB catalyzed by HRP resulted in an insoluble brown precipitate. The biotinylated HRP formed complexes with avidin that could bind the biotinylated sAb [128]. The antibodies used for IHC staining are listed in the supplementary table VI.

- **Peroxidase blocking solution:** 300 µl of 30 % H_2O_2, 130 µl of 10 % methanol in 1 ml PBS (sufficient for 1 slide).
- **Antigen retrieval buffer:** Dissolve 2.4 g of sodium citrate in 1 L ddH_2O. Adjust the pH to 6.0 with citric acid and store at RT.
- **Blocking solution:** 10 % NGS in TBST.
- **Antibody solution:** Prepare both primary and secondary antibodies in 5 % NGS TBST. Spin down at 13,000 rpm for 5 min.
- **ABC solution (Vectastain Elite ABC Kit Peroxidase, Vector Labs):** 12 µL solution A (avidin), 12 µL solution B (biotinylated horseradish peroxidase, HRP) in 600 µL PBS, mix and incubate in dark at RT for 30 min, add 600 µL TBS-T before use.
- **DAB staining solution:** 800 µL 3,3'-Diaminobenzidine (0.1 % DAB), 800 µL PBS, 1 µL 30 % H_2O_2.
- **Staining procedure:**
    - Incubate paraffin sections overnight at 37 °C.
    - Deparaffinize with 100 % toluene (2x 2 min) and rehydrate sections using decreasing concentrations of ethanol (2x 1.5 min 100 %, 1.5 min 90 %, 1.5 min 80 %, 1.5 % min 70 %, 1.5 min 60 %) at RT. Wash sections in PBS for 5 min.
    - Using a PAP pen (Science services) separate sections that are to be stained with different antibodies to create a hydrophobic barrier.
    - Block endogenous peroxidase using peroxidase blocking solution for 20 min at RT. Wash in PBS for 3 min.
    - Unmask antigens by incubating sections for 15 min in antigen retrieval solution at RT, followed by 10 min in a water bath set to 92 °C. Let cool down for 10 min at RT and wash briefly in TBS-T.
    - Block unspecific binding sites with the blocking solution for 2 hours at RT.
    - Remove the blocking solution and incubate with pAb overnight at 4 °C in a humid chamber. Wash slides 3x 5 min in TBS-T at RT.
    - Incubate with sAb for 2 hours at RT in a humid chamber. Prepare ABC solution before incubation time ends. Remove sAb, wash 3x 5 min in TBS-T, and incubate with ABC solution for 30 min at RT.
    - Prepare DAB staining solution. Discard ABC solution and wash 3x 5 min in TBS-T at RT. Incubate with DAB staining solution at RT until color develops. Monitor color development under a microscope.

- Stop staining by immersing the slides in tap water, pat dry the slides, and mount them with Aquatex® mounting medium. Let dry overnight before documenting.

- **Documentation and quantification of IHC staining:**

IHC staining of liver sections was documented in BF without phase contrast. Images were documented as mentioned under section 2.4.2.1 with an A-Plan 10/0.5x objective. In this case, color deconvolution with the H DAB option was used to separate different channels. The brown channel was used for further analysis. A hexagonal region with a central vein surrounded by the portal triad was taken as the region of interest (ROI). This is because most of the activated HSCs (aHSCs) were localized in the periportal region. Three to four ROIs were documented per slide. The images were quantified using the same protocol as mentioned in section 2.4.2.3 and the percentage of positive stained area for a given antibody was calculated as using the formula:

$$Percentage\ of\ positive\ stained\ area\ = \frac{IHC\ stained\ area}{Total\ area} \times 100\ [\%]$$

2.4.3.2 Immunofluorescence (IF)

In contrast to IHC, IF staining accounts for more sensitivity, high resolution, and signal amplification using various microscopy techniques [129]. With the availability of several different fluorophores that can be conjugated to secondary antibodies, IF allows for co-staining of several proteins. In this project the nuclear stain DAPI was combined with green (Alexa Fluor 488) and red (Alexa Fluor 555) fluorescence to analyse the status of HSCs in MASH as well as to colocalize HSC markers with proteins of the cGMP pathway. Antibodies used for IF staining are listed in the supplementary table VI.

- **General materials for staining:** Frozen liver sections (10 µm thickness), wash solution (0.1 % Triton-X 100 in PBS), blocking solution (1 % NGS in PBST), antibody solution (prepare pAb and sAb in 1 % NGS PBST; spin down at 13,000 rpm for 5 min), and DAPI mounting medium.
- **Staining procedure:**
    - Thaw liver sections at RT for ~15 min and wash sections in PBS for 15 min to remove O.C.T. Block unspecific binding sites with the blocking solution for 1 hour at RT.
    - Remove the blocking solution, add pAb, and incubate overnight at 4 °C in a humid chamber. Remove pAb and wash 3x 10 min with PBS-T.

- Incubate sections with sAb for 2 hours at RT. Keep the samples in the dark for further steps. Remove sAb and wash 3x 10 min with PBS-T. If more than one IF staining is to be performed, repeat steps 4-6.
- After the last immunostaining, immerse the slides in H_2O, remove excess liquid, and mount using DAPI mounting medium.
- Remove air bubbles by gently pressing with a pipette tip and let dry overnight before documenting.

- **Image documentation:**

Images were acquired using a confocal laser scanning microscope (LSM) 710. The setup was comprised of an inverted Axio Observer.Z1 stand (ZEISS) equipped with a diode laser (405 nm), a multiline Argon laser (25 mW; 458 nm, 488 nm, and 514 nm), a diode-pumped solid-state laser (516 nm), a He/Ne laser (633 nm) and an air objective (Plan-APOCHROMAT 20x/0.8; ZEISS). The 405 nm laser was used to excite Hoechst 33258, while the Argon laser 488 nm line and the 561 nm laser were used to excite Alexa Fluor 488 and Alexa Fluor 555/594 respectively. Images were documented using the ZEN Black software (ZEISS) with a 20x objective.

- **Image analysis:**

Images acquired with LSM 710 were analysed using QuPath (RRID: SCR_018257). QuPath is an open source bioimage analysis software with built-in algorithms for cell and tissue detection. It consists of a cross-platform, multithreaded, tile-based whole slide image viewer with extensive annotation and visualization tools. The software allows for creating customized workflows with powerful Groovy scripting functionality which can be linked together for batch processing of images [130]. In this study, the two parameters analysed for IF images are- the percentage of cells positive for a given staining and the percentage of area positive for a given staining. A detailed scripting protocol is given in the extended methods 7.2.

2.4.4 RNA and protein expression analysis

2.4.4.1 RNA extraction and RT-PCR

To analyse the expression of inflammatory and fibrotic markers in the liver that are upregulated during MASH, RNA was extracted from liver tissues using QIAGEN RNeasy mini kit (Cat-#74106) and RT-PCR was performed. The following markers were analysed: ACTA2, TNF-α, IL-6, IL1A, IFN-γ, CCL2, and CXCL10.

- **General materials for RNA isolation:** Tissue homogenizer, QIAGEN RNeasy mini kit (Cat-#74106), β-mercaptoethanol, NanoDrop, and 2 ml Eppendorf tubes.
- **RNA extraction procedure:**
    - Weigh 2 ml Eppis and tare it. Cut a small piece from the liver tissue using a scalpel and place it in the 2 ml Eppi. The tissue should not weigh more than 30 mg.
    - Prepare tissue homogenizing buffer with RLT buffer + β-Mercaptoethanol. Use 350 μL of this buffer for < 20 mg of tissue and 600 μL for 20-30 mg of tissue.
    - Clean homogenizer with 70 % isopropanol, ddH_2O, and RNeasy Zap Spray. Perform this cleaning step between each sample.
    - Homogenize each tissue sample for 3 sec or longer if clumps exist without too much foam.
    - Centrifuge the lysate(s) for 3 min, full speed at RT, and transfer the supernatant to a new reaction tube.
    - Add 1 volume of 70 % EtOH to the lysate(s) and mix gently by pipetting. Transfer the whole mixture to a QIAshredder spin column in a 2 ml collection tube, close the lid gently, and centrifuge for 2 min, full speed at RT.
    - Transfer the run-through to a new Eppi, add 1 volume of 70 % EtOH to the lysate(s), and mix gently by pipetting. Transfer 700 μL to a RNeasy spin column in a 2 ml collection tube and close the lid gently.
    - Centrifuge for 1 min, full speed at RT. Discard the flow through in the 2 ml collection tube. Re-use the collection tube.
    - Add 700 μL of RW1 buffer to the RNeasy spin column and close the lid gently. Centrifuge for 1 min, full speed at RT. Discard the flow through in the 2 ml collection tube. Re-use the collection tube.
    - Prepare the RPE buffer according to the manual instructions. Add 500 μL of RPE buffer to the RNeasy spin column. Centrifuge for 1 min, full speed at RT. Discard the collection tube with the flow through.
    - Add 500 μL of RPE buffer to the RNeasy spin column and close the lid gently. Centrifuge for 2 min, full speed at RT. Discard the collection tube and the flow through.
    - Place the RNeasy spin column in a fresh 2 ml collection tube, close the lid, and centrifuge for 1 min, at full speed at RT. This step eliminates any leftover RPE buffer.
    - Place the RNeasy column in a 1.5 ml Eppi (provided from the kit), add 30-50 μL of RNeasy-free water directly to the spin column membrane, and centrifuge for 1 min, full speed at RT to elute the RNA.
- **RNA quality and quantity analysis with NanoDrop:**

The eluate-containing RNA was assessed for its purity and concentration using NanoDrop 1000 Spectrophotometer and its software (Thermo Fisher Scientific).

- Place 1.3 µL of RNA sample onto the sample retention system and close the sampling arm. Begin the measurement using the operating software.
- Clean the sample retention system and the arm using Precision Wipes (KIMTECH^{Science}) between measurements and repeat step 1.

To check any contamination from protein or co-purified contaminants, the ratio of absorbance A260/A280 and A260/A230 was used. In either case, a ratio between 1.8-2.0 was considered pure for RNA. The measured RNA samples were then analysed via RT-PCR.

2.4.4.2 Protein extraction

Protein expression of healthy and MASH liver tissue was compared by western blotting. The antibodies are listed in supplementary table VI. The dissected liver lobe was preserved by shock freezing in liquid nitrogen and was stored at – 20 °C until protein extraction. Firstly, the proteins were extracted from tissues and their concentration was determined. The proteins were then separated according to their molecular weight using SDS-PAGE and blotted onto a membrane. Finally, the proteins of interest were detected with highly sensitive chemiluminescence (ECL) detection.

- **General materials for protein extraction:** FastPrep® tubes, orange caps, 6.35 mm ceramic spheres, garnet matrix A bulk (all from MP Biomedicals).
- **Tissue lysis buffer:** 50 mM Tris-Cl (pH 8.0), 100 mM NaCl, 5 mM EDTA, 2 % SDS and 2.5 mM PMSF in H_2O. Attention: Add PMSF towards the end.
- Dissect and weigh a small piece of the liver tissue using an analytical balance (QUINTIX35-1S; SARTORIUS) and note down the exact weight.
- Place tissue in FastPrep® 2 ml Lysing Matrix Tubes supplemented with garnet matrix A and 635 mm ceramic sphere. Add 7.5 µL of tissue lysis buffer per mg tissue sample.
- Disrupt tissue with two FastPrep-24 (MP Biomedicals) cycles for 1 min at 6.5 m/s speed for each cycle. Put samples on ice between cycles.
- Denature samples for 5 min at 94 °C in a Thermomixer compact (Eppendorf). Centrifuge samples for 10 min at 14,000 rpm at 4 °C. Transfer the supernatant into a new tube and store it at - 20°C or immediately continue with protein quantification.

Total protein content was estimated with bicinchoninic acid (BCA) assay [131]. Like Lowry, this colorimetric assay involves the conversion of Cu^{2+} to Cu^{+} under alkaline conditions. The Cu^{+} is detected upon reaction with BCA. The stability of BCA under alkaline conditions allows this assay to be carried out as a one-step process [Walker, JM. 1994]. The assay was performed in a 96-well plate in duplicates. The resulting intense purple color with an absorbance of 562 nm was measured with the MultiSkan EX multi-well plate reader (Thermo).

- Pierce™ BCA Protein Assay Kit (Thermo Scientific, REF 23227, contains BSA standard, BCA Reagent A, BCA Reagent B). Prepare the BSA standard according to the kit instructions.
- Prepare the BCA working reagent (WR) as using the following formula to determine the total volume of WR required: (6 standards + # unknowns (protein sample)) x (2 replicates) x (2 ml per sample) = total volume of WR required.
- Prepare the WR by mixing 50 parts of BCA Reagent A with 1 part of BCA Reagent B (50:1, Reagent A:B) and mix thoroughly by vortexing.
- Pipette 25 µL of each standard and the protein sample replicate into a microplate well. Add 200 µL of the WR to each well, cover the plate and incubate at 37 °C for 30 mins.
- Measure the absorbance at 562 nm using a plate reader and calculate the protein concentration using the BSA standard curve after subtracting the appropriate blank control.

2.4.4.3 SDS-PAGE

- **4x Tris/SDS pH 8.8:** 1.5 M Tris (18.2 g) and 0.4 % SDS (0.4 g) in H_2O. Adjust pH to 8.8 and store at 4 °C.
- **4x Tris/SDS pH 6.8:** 0.5 M Tris (3.02 g) and 0.4 % SDS (0.2 g) in H_2O. Adjust pH to 6.8 and store at 4 °C.
- **5x SDS loading dye:** 320 mM Tris pH 6.8, 40 % Glycerol, 15 % SDS, 25 % 2-mercaptoethanol, and 1 mg/ml bromophenol blue. Concentrations are adjusted to the 5x stock solution used in the protocol. Store at -20 °C.
- **10x SDS running buffer:** 25 mM Tris (15.1 g), 192 mM glycine (72.0 g), and 0.1 % SDS (5.0 g) in ddH_2O. Store at RT.
- **Other buffers and chemicals:** Rotiphorese Gel 30 (Roth, Cat-#3029.1), TEMED, APS (20 % in H_2O), isopropanol, protein ladder (PageRuler Prestained Protein Ladder; Thermo)
- **10 % separating gel (1.5 mm):** 3.3 ml Rotiphorese Gel 30, 1.25 ml 4x Tris/SDS pH 8.8, 4.1 ml H_2O, 10 µL TEMED, 50 µL APS, always prepare freshly before casting the gel.
- **4 % stacking gel (1.5 mm):** 0.65 ml Rotiphorese Gel 30, 1.25 ml Tris/SDS pH 6.8, 3.05 ml H_2O, 10 µL TEMED, 50 µL APS, always prepare freshly before casting the gel.
- Prepare gel in the mini-protein chamber (Bio-Rad). First, pour the separating gel and overlay it with isopropanol to achieve an even layer and let polymerize for ~ 30 min.
- Remove isopropanol, pour the stacking gel, and gently place the combs. Let polymerize for ~ 30 min.
- Thaw protein samples on ice and dilute them to the required concentration with H_2O and 5x SDS loading dye.
- Denature protein samples at 95 °C for 5 min in a Thermomixer compact (Eppendorf).
- Fill the gel running chamber with 1x SDS running buffer and place the gel setup. Load samples into the gel (40 µg total protein in 15 µL/pocket). Load 3 µL of protein ladder as a size reference.

- Separate proteins by applying 80 V for 10 min and 120 V for 1 hour (Standard Power Pack P25, Biometra).

2.4.4.4 Western blotting and detection

- **Anode buffer I:** 300 mM Tris (36.3 g), 20 % (v/v) methanol (200 ml 100 % methanol), fill up to 1 L with H_2O, adjust pH to 10.4, and store at RT.
- **Anode buffer II:** 20 mM Tris (3 g), 20 % (v/v) methanol (200 ml 100 % methanol), fill up to 1 L with H_2O, adjust pH to 10.4 and store at RT.
- **Cathode buffer:** 40 mM 6-amino hexanoic acid (5.2 g), 25 mM Tris (3 g), 20 % (v/v) methanol (200 ml 100 % methanol), fill up to 1 L with H_2O, adjust pH to 7.6 with HCl and store at RT.
- **Blocking solution:** 5 % milk powder in TBS-T, store at 4 °C.
- **Blotting materials:** 0.35 mm, 195 g/m^2 blotting paper (Cat-#GB46, A.Hartenstein), PVDF membrane (0.2 μm pore size, #03010040001, Roche).
- **ECL reagent:** mix 1 ml WesternBright® Sirius (luminol/enhancer solution, Biozym) with 1 ml WesternBright® Peroxide (chemiluminescent detection reagent, Biozym), prepare directly before use.
- **pAb solution:** pAb (see Supplementary table VI) in 5 % BSA, 0.05 % NaN_3, add 5 ml TBS-T and store at 4 °C.
- **sAb solution:** HRP coupled sAb (see supplementary table VI) in 1 % milk TBS-T, prepare freshly.
- **Wash buffer:** 1x TBS (100 ml 10X TBS), 0.1 % Tween-20 (1 ml), fill up to 1 L with ddH_2O and store at RT.
- After separation of proteins with SDS-PAGE, transfer proteins from SDS gel onto a PVDF membrane using a discontinuous Trans-Blot SD Semi-Dry Transfer Cell system (Bio-Rad).
- Assemble the ''blotting sandwich'' in the following order (from anode to cathode):
    a. 4 Whatman blotting papers soaked in anode buffer I
    b. 4 Whatman blotting papers soaked in anode buffer II
    c. PVDF membrane
    d. SDS gel
    e. 8 Whatman blotting papers soaked in cathode buffer
- Remove all air bubbles by gently rolling a 10 ml pipette over the assembled sandwich.
- Blot by applying a current of 60 mA per blotting sandwich for 75 min (Standard Power Pack P25, Biometra).
- Disassemble the blotting sandwich after ensuring complete protein transfer by looking at the prestained protein ladder.
- Block PVDF membrane for 1 hour at RT in blocking solution. After blocking, cut membranes according to the molecular weight of proteins being detected.
- Wash membranes 2x with TBS-T. Incubate membranes in pAb overnight at 4 °C.

- Wash 3x with wash buffer for 5 min each. Incubate in HRP-coupled sAb for 2 hours at RT. Wash 3x with wash buffer for 5 min each.
- Add ECL substrate to PVDF membrane and detect chemiluminescence with a ChemiDoc Imaging System (Bio-Rad).

2.5 Software and statistical analysis

The software used in the current study for data analysis and figure preparation is as follows.

- **FIJI (RRID:SCR_002285)** (latest version 1.53k) was used for histology image analysis [132]. The update sites ''ImageJ'', ''Fiji'', ''Java-8'', ''BIG-EPFL'', and ''PTBIOP'' were activated to download the required plugins.
- **QuPath (RRID:SCR_018257)** (version v0.4.3 from qupath.github.io) was used for immunofluorescence image analysis [130].
- **Origin Pro (RRID:SCR_014212)** (latest version 9.8.5.201, OriginLab Corporation, Northampton, MA, USA) and **MS Excel** (latest version 16.0.14326.20384, Microsoft Corporation, Redmond, WA, USA) were used for data analysis.
- **CorelDRAW 2017 (RRID:SCR_014235)** (latest version 19.0.0.328, Corel Corporation, Ottawa, Ontario, Canada) was used for preparing the figures.
- **BioRender (RRID:SCR_018361)** web application was used for creating graphical illustrations.
- **EndNote 20 (RRID:SCR_014001)** (latest build 15341, Clarivate, Boston, MA, USA) was used for bibliography.

Statistical analysis was performed using OriginPro. The Shapiro-Wilk test was used to test the normal distribution of the data. The Mann-Whitney U test was performed for pairwise comparison of non-normally distributed data. A Two-Sample Test was used for pairwise comparison of normally distributed data. For group wise comparisons of more than two groups, a non-parametric analysis with Mann-Whitney-U-Test was used. Statistical significance was considered for $p<0.05$ and indicated in three ways (*$p<0.05$, **$p<0.01$, ***$p<0.001$, n.s $p>0.05$).

3 Results

3.1 A diet-induced mouse model for MASH

Non-alcoholic steatohepatitis (MASH) belongs to the spectrum of non-alcoholic fatty liver disease (MASLD) and is characterized by hepatic steatosis, inflammation, and fibrosis [133]. Patients with fatty liver disease are predisposed to various non-liver comorbidities, including atherosclerosis [134]. In the current study, we established a new diet-induced mouse model

for MASH in the presence of ApoE knockout (ApoE KO). This model is based on an existing mouse model which recapitulates the features of human MASH [84, 113] and the development of atherosclerosis [135-137]. In the following sections, we characterized ApoE KO mice fed a high-fat diet for 18 weeks (HFD) and compared them to wildtype mice on a normal diet (ND) to study liver health and MASH.

3.1.1 The body and liver weight are increased in HFD mice compared to ND mice

ApoE KO with a high-fat diet is a widely used mouse model to study the development of atherosclerosis. ApoE is known to play a crucial role in lipoprotein metabolism [138-140] and its absence, among others, is known to cause metabolic syndrome and obesity which are known risk factors for MASH [141-143]. Studies have shown that ApoE KO on HFD can be used for analysing MASH [84, 113]. We made a modification to this previously described model by extending the duration of high-fat diet feeding to 18 weeks and compared the effects in both sexes for the first time. First, we analysed physiological alterations such as weight gain and liver weight. To examine the weight gain, 10-week-old male and female ApoE KO mice were placed on a high-fat diet (hereafter referred to as HFD mice) for 18 weeks. As a control group, 10-week-old male and female wildtype (WT) mice were fed a normal chow diet (hereafter referred to as ND mice) for 18 weeks. To calculate the liver-to-body weight ratio, the liver weight was divided by the body weight. As expected, after 18 weeks on the diet, both male and female HFD mice showed a significant body weight gain compared to the ND mice **(Figure 13A-B)**. It is also interesting to note that both male and female HFD mice showed signs of hepatomegaly [84] as seen by the increase in liver-to-body weight ratio **(Figure 13C-D)**. In conclusion, ApoE KO in combination with HFD affected the body and liver weight in both sexes with males being slightly heavier than females.

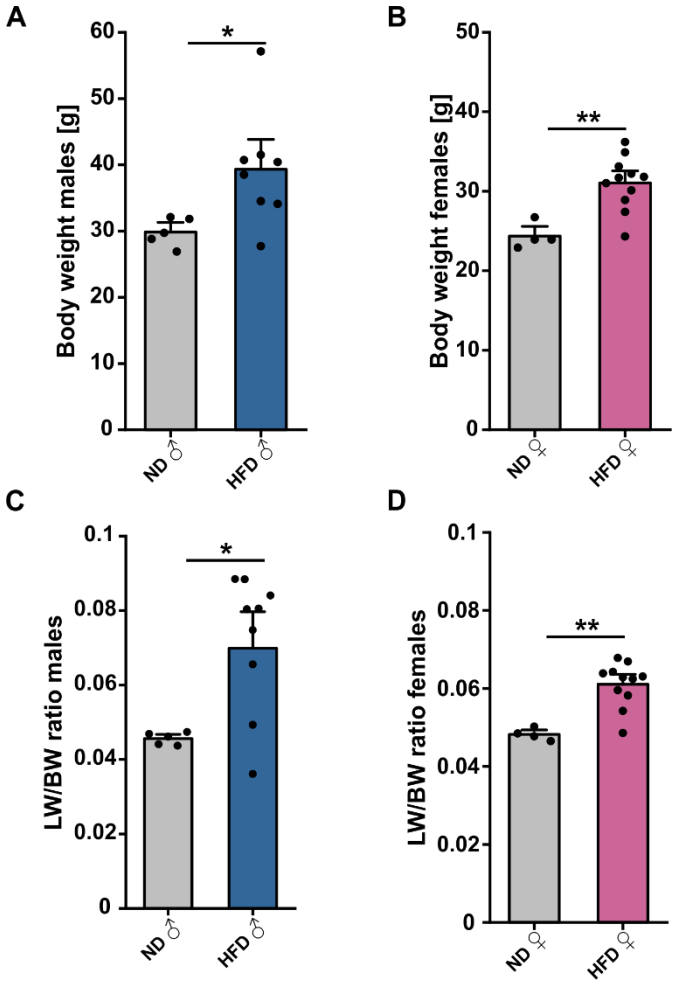

Figure 13: Body and liver weight in ND and HFD mice (A, B) Body weight of **(A)** male ND (n=5 mice), HFD (n=8 mice) and **(B)** female ND (n=4 mice), HFD (n=11 mice) groups. **(C, D)** Relative liver weight (liver-to-body weight ratio) in **(C)** male ND (n=5 mice), HFD (n=8 mice) and **(D)** female ND (n=4 mice), HFD (n=11 mice) groups. Data are represented as mean ± SEM. Statistical significance with the Mann-Whitney U test is indicated by asterisks (* $p<0.05$; ** $p<0.01$). ND: WT mice on ND; HFD: ApoE KO mice on HFD.

3.1.2 HFD leads to intrahepatic fat accumulation (steatosis) and hepatocyte degeneration (ballooning) in male and female mice

Hepatic steatosis and hepatocyte ballooning are the onsets of fatty liver disease and important histological parameters in the diagnosis of MASH. Hepatic steatosis is characterized by the accumulation of triacylglycerol-rich lipid droplets within the hepatocytes [87]. Oil Red O (ORO) staining was performed on frozen liver sections to analyse steatosis and the nuclei of hepatocytes were counter-stained with hematoxylin. The percentage of ORO positive area was quantified computationally in relation to the total area of the image. After ORO staining, the accumulated lipids could be easily visualized by their intense orange color. Hematoxylin stained the nuclei of hepatocytes in blue. ND mice showed a sparse accumulation of lipid

droplets in the liver section **(Figure 14A)**. On the other hand, HFD mice showed an increased accumulation of large lipid droplets throughout the liver section indicating steatosis **(Figure 14B)**. Quantification of ORO staining in males and females showed an increase in the percentage of ORO positive area in HFD mice (males: 18 % ± 0.7; females: 21 % ± 2.9) in comparison to the ND mice (males: 0.2 % ± 0.08; females: 0.4 % ± 0.06) **(Figure 14C)**. Statistical analysis was not significant due to the small sample size.

Next, we analysed hepatocyte ballooning which is caused as a result of excess fat accumulation in hepatocytes. It is defined as the cellular enlargement of hepatocytes with disrupted cytoplasm [144]. To analyse ballooning, an H&E staining was performed on paraffin liver sections. The hematoxylin stained the cell nuclei in blue and eosin stained the cytoplasm in pink. There was a striking difference in the structure of hepatocytes and the appearance of the liver parenchyma between both groups. ND mice displayed healthy liver parenchyma consisting of uniformly stacked hepatocytes from the central vein toward the periphery **(Figure 14D)**. These hepatocytes were roughly circular in shape with a large well-defined nucleus in the centre **(Figure 14D right, arrows)**. However, HFD mice showed a distorted liver parenchyma with numerous large lipid vacuoles in the peri-portal areas **(Figure 14E indicated a PP)**. The hepatocytes in these livers were swollen consisting of large and small lipid droplets deposited in the cytoplasm. The nucleus was rather small and pushed toward the periphery of the cell **(Figure 14E right, arrows)**. However, the ballooning effect was not very severe in female HFD mice. This was also reflected in the number of lipid vacuole count surrounding the portal veins (PV) in male and female HFD mice **(Figure 14F)**. A total of 124 portal vein regions (2-3 regions per section) were analysed. The average count of lipid vacuoles was 177 ± 30.8 in male HFD mice (counted in 18 sections from 6 mice) and 93 ± 10.8 in female HFD mice (counted in 26 sections from 9 mice). No lipid vacuoles were detected in the livers of ND mice.

Finally, we analysed the metabolic disorders associated with the development of MASH by measuring the triglyceride (TAG) and cholesterol content in liver tissue lysates. These parameters were significantly increased in HFD compared to the ND mice, in line with increased LDL levels determined in the blood plasma **(Figure 14G-H)**. The plasma lipid values are shown in supplementary table IX. Although, the female HFD mice showed reduced ballooning in comparison to the males, the other parameters remained relatively same between both sexes.

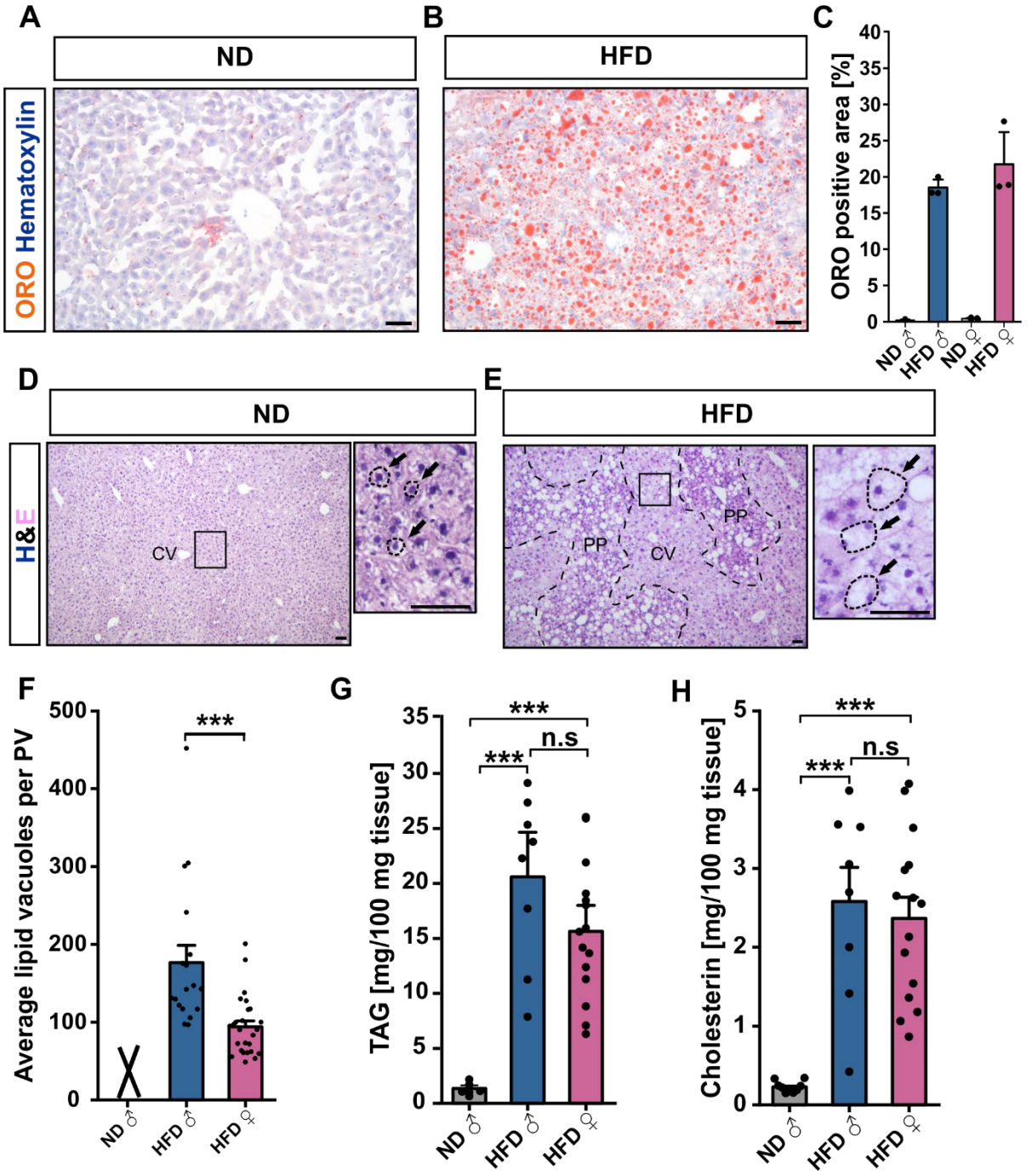

Figure 14: Hepatic steatosis and hepatocyte ballooning in ND and HFD mice. (A, B) Representative ORO staining on frozen liver sections of **(A)** ND and **(B)** HFD mice. **(C)** Quantification of ORO-positive area in male ND (n=3 mice) and HFD (n=3 mice) mice and female ND (n=3 mice) and HFD (n=3 mice) groups. **(D, E)** Representative images of H&E staining on paraffin liver sections of **(D)** ND and **(E)** HFD mice. Panels show for each image (from left to right) an overview picture and magnification with arrows denoting the structure of hepatocytes. Regions marked with CV indicate central vein and PP peri-portal areas. **(F)** Average count of lipid vacuoles per portal vein in male HFD (n=6 mice) and female HFD (n=9 mice) groups. Data points represent the number of sections analysed. **(G)** Hepatic triglycerides measured in liver tissues from male ND (n=9 mice), HFD (n=8 mice) and female HFD (n=15 mice) groups. **(H)** Hepatic cholesterol content measured in liver tissues from male ND (n=9 mice), HFD (n=8 mice) and female HFD (n=15 mice) groups. Data are represented as mean ± SEM. Statistical significance with the Mann-Whitney U test is indicated by asterisks or n.s (* $p<0.05$; ** $p<0.01$; *** $p<0.001$; n.s $p>0.05$). The scale bars are 50 µm. ND- WT mice on ND; HFD- ApoE KO mice on HFD.

3.1.3 Peri-portal fibrosis is enhanced in male and female HFD mice

Hepatic fibrosis is a wound-healing response to long-term chronic liver injury. It is characterized by the excessive accumulation of ECM proteins including collagen in the liver [145, 146]. Chronic liver injury causes hepatic stellate cells (HSCs) to transdifferentiate from a ''quiescent'' (qHSCs) to an ''activated'' (aHSCs) state which is associated with the enhanced secretion of ECM components leading to fibrosis [68, 147]. We analysed hepatic fibrosis by performing picrosirius red (PSR) in combination with fast-green (FG) staining on paraffin liver sections. PSR stained the collagen fibers in red. The additional FG staining of non-collagen compounds enabled a more precise quantification of fibrotic areas by reducing the background interference from PSR.

In the ND group, PSR staining was observed exclusively around the vascular walls of the blood vessels together with a very low amount of collagen fibres in the liver parenchyma **(Figure 15A)**. Whereas, both male and female HFD mice showed enhanced fibrosis, particularly in the peri-portal areas **(Figure 15B-C indicated as PP)**. Contrary to the ND, we observed an excess accumulation of collagen fibres in the liver parenchyma. Quantification revealed a 13-fold increase in the percentage of PSR-positive area in male HFD mice (5.5 % ± 1.5; 18 sections from 6 mice) in comparison to the ND (0.4 % ± 0.04; 12 sections from 4 mice) mice. In female HFD mice, the PSR-positive area was observed to be 8-fold higher (3.1 % ± 0.7; 18 sections from 6 mice) compared to the male ND mice. The females exhibited a significant decrease in PSR-positive area compared to the male HFD mice **(Figure 15D)**.

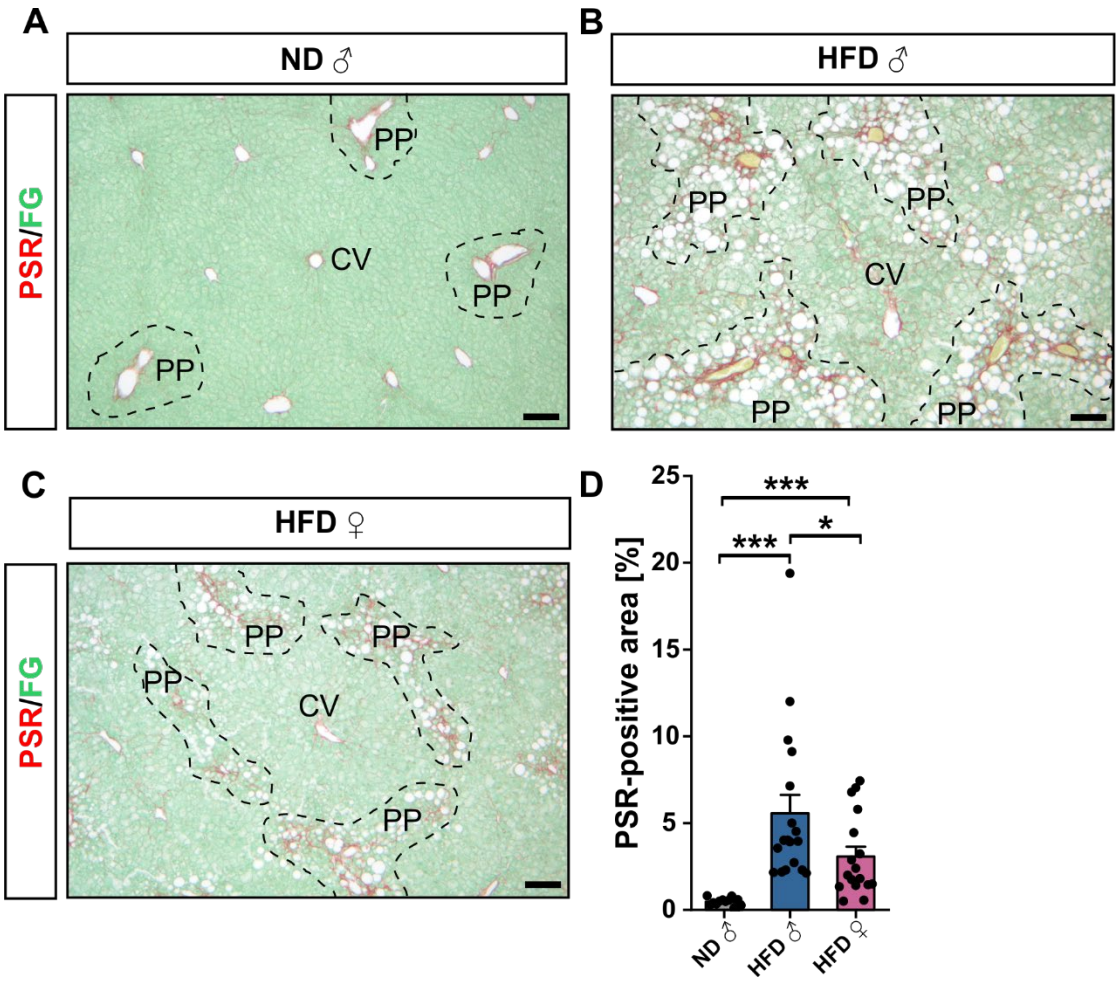

Figure 15: Hepatic fibrosis in ND and HFD mice. (A-C) Representative images of PSR/FG staining on paraffin liver sections from **(A)** male ND **(B)** male HFD and **(C)** female HFD mice. **(D)** Percentage of PSR-positive area analysed in male ND (n=4 mice), HFD (n=6 mice) and female HFD (n=6 mice) groups. Regions marked with CV indicate central vein and PP peri-portal areas. Data points represent sections analysed. Data are represented as mean ± SEM. Statistical significance with the Mann-Whitney U test is indicated by asterisks (* $p<0.05$; *** $p<0.001$). The scale bars are 100 µm. ND- WT mice on ND; HFD- ApoE KO mice on HFD.

3.1.4 HSCs in HFD mice show activation and altered morphology

In the previous section, we analysed hepatic fibrosis associated with excess of collagen deposition, presumably due to the activation of HSCs. Hence, our next aim was to study HSCs in the liver, focusing on the changes they undergo upon activation (aHSCs). To address this goal, we checked the expression of classical HSC markers- desmin, an intermediate filament protein serving as a reliable HSC marker regardless of their activation status [92, 148], and α-SMA, a widely recognized indicator of activated HSCs [92, 149-151]. Recent studies using scRNA-seq have also identified SM22 (Transgelin) as an additional HSC activation marker [72, 152, 153].

We first checked the protein expression of desmin and SM22 in whole liver lysates of male and female ND and HFD mice. Western blot analysis was performed with three independent biological replicates for each group and GAPDH was used as a loading control. Both male and female HFD mice showed an enhanced protein expression of desmin and SM22 in comparison to the ND group **(Figure 16A left and right)**. This was reflected in the protein quantification which was normalized to GAPDH. Due to the small sample size (protein from three 3 livers per group), the data from male and female mice was pooled for statistical analysis **(Figure 16B-C)**.

Immunofluorescence (IF) staining confirmed the localization of desmin and SM22 in HSCs and an enhanced expression could be detected in the liver sections of animals on HFD. In sections of ND mice, desmin stained HSCs with their characteristic cytoplasmic extensions were present throughout the liver parenchyma as single cells **(Figure 16D)** and appeared smaller in size **(Figure 16D right, arrows)**. On the other hand, HSCs in liver sections of HFD mice were more elongated with long cytoplasmic extensions contacting the surrounding cells **(Figure 16E)** and were present in clusters **(Figure 16E right, arrows)**. The percentage of desmin-positive cells was 16 % ± 1.5 in the ND group (3 sections from 3 mice) and 35 % ± 8.7 in the HFD group (3 sections from 3 mice) **(Figure 16J)**.

In the ND group, SM22 staining was mainly observed in the smooth muscle cells (SMCs) around the blood vessels **(Figure 16F)**. Furthermore, very few SM22-positive cells were seen in the liver parenchyma indicating that the amount of aHSCs in these livers is very low **(Figure 16F right, arrows)**. In addition to the SMCs around the vessels, the HFD group showed more SM22-expressing cells in the liver parenchyma **(Figure 16G)**. These cells were found in clusters and had elongated cytoplasmic extensions **(Figure 16G right, arrows)** similar to the desmin-positive cells in **(Figure 16E)**, indicating that they are aHSCs. SM22-positive cells were determined in a total of 12 sections from 3 ND mice and 3 HFD mice. The percentage of SM22-positive cells was 1.4 % ± 0.4 (7 sections from 3 mice) in the ND group and 7.2 % ± 1.9 in the HFD group (7 sections from 3 mice) **(Figure 16K)**.

Finally, the expression of the classical HSC activation marker α-SMA was analysed using immunohistochemistry (IHC). α-SMA was observed predominantly in SMCs surrounding the vascular walls of portal and central veins in the ND group **(Figure 16H).** The HFD group showed an increased amount of α-SMA-positive aHSCs within the liver parenchyma in addition to the

SMCs surrounding portal and central veins **(Figure 16I right, arrows)**. The percentage of α-SMA-positive area was 0.29 % ± 0.08 in the ND group (9 sections from 3 mice) and 3.15 % ± 0.17 (20 sections from 5 mice) in the HFD group **(Figure 16L)**. Taken together these data indicate that HSCs are activated in our HFD model which is evident by alterations in cell morphology and enhanced expression of activation markers SM22 and α-SMA.

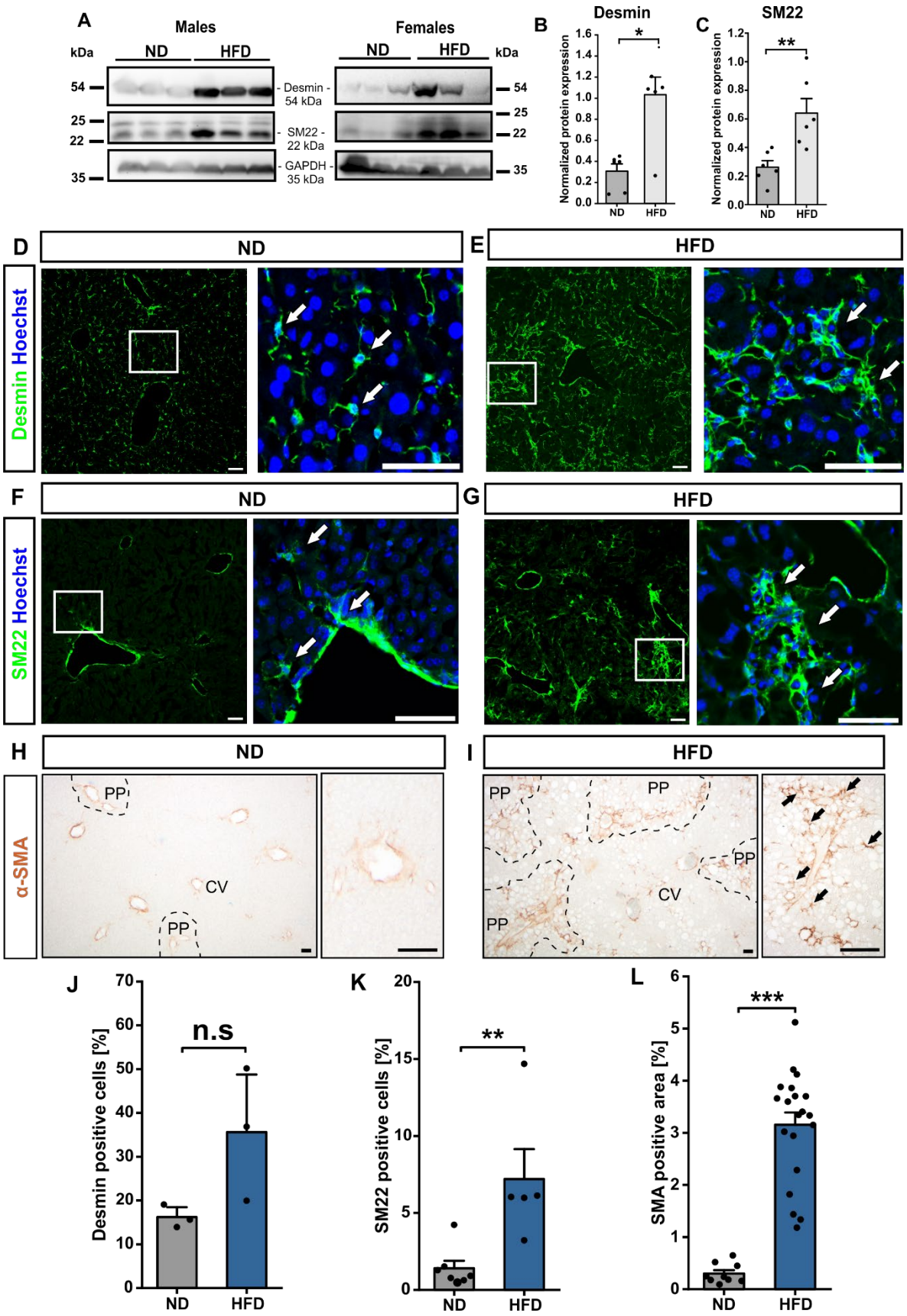

Figure 16: Expression analysis of Desmin, SM22, and α-SMA (A) Western blot analysis of desmin and SM22 in male **(left)** and female **(right)** ND and HFD mice. **(B)** Normalized protein expression of desmin in pooled male and female ND (n=6) and HFD (n=6) mice. **(C)** Normalized protein expression of SM22 in pooled male and female ND

(n=6) and HFD (n=6) mice. **(D, E)** Representative desmin IF staining on frozen liver sections from **(D)** ND and **(E)** HFD mice. **(F, G)** Representative SM22 IF staining on frozen liver sections from **(F)** ND and **(G)** HFD mice. Panels show for each image (from left to right) an overview picture and an overlay magnification with arrows denoting HSCs. (Blue: nuclei (Hoechst 33258); Green: Desmin or SM22). **(H, I)** Representative α-SMA IHC staining on paraffin liver sections from **(H)** ND and **(I)** HFD mice. Panels show for each image (from left to right) an overview picture and a magnification with arrows indicating the presence of aHSCs. Regions marked with CV indicate central vein and PP peri-portal areas. **(J)** Percentage of desmin-positive cells in ND (n=3 mice) and HFD (n=3 mice) groups. **(K)** Percentage of SM22-positive cells in ND (n=3 mice) and HFD (n=3 mice) groups. Data points represent sections analysed. **(L)** Percentage of α-SMA-positive area in ND (n=3 mice) and HFD (n=5 mice). Data points represent sections analysed. Data are represented as mean ± SEM. Statistical significance with the Mann-Whitney U test and Two-sample t-test is indicated by asterisks or n.s (n.s $p>0.05$; * $p<0.05$; ** $p<0.01$). The scale bars are 50 µm. ND- WT mice on ND; HFD- ApoE KO mice on HFD.

The first part of our results indicates that ApoE KO mice subjected to an 18-week HFD serve as a suitable model for studying MASH. Both male and female animals develop MASH characterized by steatosis, ballooning, fibrosis, and HSC activation. Notably, females exhibit relatively milder effects compared to males.

3.2 cGMP signalling pathway in healthy and MASH livers

Altered lipid metabolism and inflammation are the primary factors that contribute to MASH and comorbidities like atherosclerosis. The intracellular 2nd messenger cGMP is known to have varying effects on both disease conditions. cGMP production is induced by the endogenous ligand NO via the activation of its receptor NO-GC. NO-GC in turn generates cGMP from GTP. Subsequently, cGMP exerts its effects via its downstream effectors like cGKI [1, 25].

Interestingly, the NO/cGMP/cGKI signalling cascade has been shown to have a pro-atherogenic as well as anti-atherogenic effects [3, 154, 155]. In the context of the liver, studies have indicated the expression of the cGMP generator NO-GC in HSCs of MASH and fibrotic livers induced via a choline-deficient high-fat diet (CD-HFD) or carbon tetrachloride (CCl_4) [14, 72]. It has been demonstrated that the cGMP effector cGKI is expressed in HSCs of a healthy liver [73, 74]. Furthermore, the cGMP pathway was shown to play a role in improving the liver phenotype in diseases like fibrosis [13, 109] and cirrhosis [15, 156].

These studies indicate that the NO/cGMP/cGKI signalling could be a promising target in maintaining liver health. However, these liver disease models often exhibit a high mortality rate owing to their diet and/or exposure to various chemical treatments. Therefore, our objective was to characterize this pathway in healthy as well as for the first time in the context

of MASH in an ApoE KO+HFD model, which is comparatively less rigorous and ensures long-term survival. Our model simultaneously develops both MASH and atherosclerosis.

3.2.1 Components of the NO/cGMP pathway are expressed in healthy and MASH livers

Expression of the cGMP pathway components NO-GC and cGKI was initially checked in the whole liver lysates from ND and HFD mice via western blot analysis. Three independent biological replicates were used for each group with GAPDH as a loading control. The protein expression was quantified by normalizing to GAPDH. Both male and female HFD mice showed enhanced protein expression of NO-GC and cGKI in comparison to the ND group **(Figure 17A; left and right)**. Due to the small sample size (protein from three 3 livers per group), the data from male and female mice was pooled for statistical analysis **(Figure 17B-C)**.

To identify cells that express NO-GC and cGKI, IF staining was performed on frozen liver sections from ND and HFD mice. In healthy ND liver sections, cells with star-like morphology containing short cytoplasmic extensions stained positive for NO-GC and were present as single cells within the liver parenchyma **(Figure 17D; right, arrows)**. In HFD MASH liver sections, we observed clusters of NO-GC-positive cells in the liver parenchyma with long cytoplasmic extensions. The cells were present in clusters **(Figure 17E; right, arrows)**. The percentage of NO-GC positive cells was 13 % ± 0.6 in the ND (3 sections from 3 mice) and 27 % ± 8.6 in the HFD (analysed in 3 sections from 3 mice) group. For statistical analysis, the number of sections stained with NO-GC has to be increased.

The effects of cGMP in many tissues are mediated via its downstream effector cGKI. Therefore, it was determined whether cGKI is also expressed in healthy and MASH livers. IF staining revealed an identical expression pattern to NO-GC. Liver sections from ND showed star-like cells positive for cGKI **(Figure 17F; right, arrows)** while HFD showed clusters of cGKI-positive cells **(Figure 17G; right, arrows)**. The percentage of cGKI positive cells was 6 % ± 0.9 the ND group (3 sections from 3 mice) and 30 % ± 2.8 (analysed in 3 sections from 3 mice) in the HFD group. For statistical analysis, the number of sections stained with cGKI has to be increased.

Hepatocytes, the most common cell type in the liver were not stained by NO-GC or cGKI antibodies **(Figure 17D-G; right, nuclei without NO-GC or cGKI staining)**. Additionally, in both groups, NO-GC and cGKI were detected in SMCs around the blood vessels.

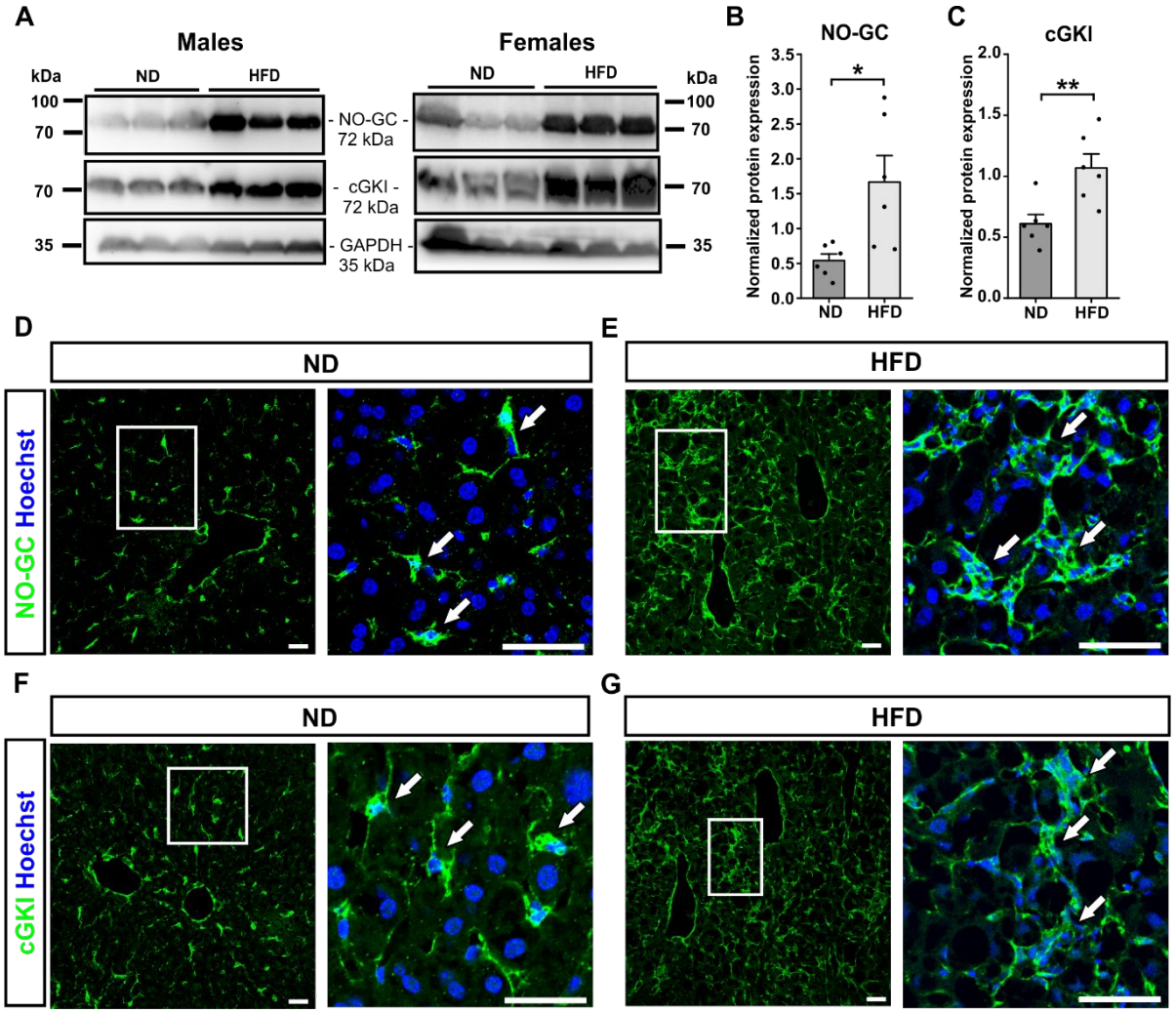

Figure 17: **Expression analysis of NO-GC and cGKI. (A)** Western blot analysis of NO-GC and cGKI in male **(left)** and female **(right)** ND and HFD mice. **(B)** Normalized protein expression of NO-GC in pooled male and female ND (n= 6) and HFD (n= 6) mice. **(C)** Normalized protein expression of cGKI in pooled male and female ND (n= 6) and HFD (n= 6) mice. **(D, E)** IF staining of NO-GC on frozen liver sections from **(D)** ND (n=3 mice) and **(E)** HFD (n=3 mice). **(F, G)** IF staining of cGKI on frozen liver sections from **(F)** ND (n=3 mice) and **(G)** HFD (n=3 mice). Panels show for each image (from left to right) an overview picture and an overlay magnification with arrows denoting the structure HSCs. (Blue: nuclei (Hoechst 33258); Green: NO-GC or cGKI). Data are represented as mean ± SEM. Statistical significance with the Mann-Whitney U test is indicated by asterisks (* $p<0.05$; ** $p<0.01$). The scale bars are 50 µm. ND- WT mice on ND; HFD- ApoE KO mice on HFD.

3.2.2 NO-GC and cGKI are expressed in HSCs of fibrotic liver

It has been shown previously that NO-GC is expressed in HSCs of healthy and fibrotic livers [14]. The expression of cGKI was demonstrated only in HSCs of a healthy liver [73, 74]. Our aim was to confirm these findings in our model and additionally to check for the expression of cGKI in HSCs of MASH liver. We performed IF co-staining of HSC marker desmin which is fluorescently conjugated to Alexa 488 with NO-GC or cGKI. IF staining on frozen liver sections from HFD mice revealed colocalization of desmin with NO-GC **(Figure 18A)** or desmin with cGKI **(Figure 18B)**, confirming the presence of these components of the cGMP signalling

pathway within clustered, presumably activated HSCs **(Figure 18A zoom-in with arrows; Figure 18B zoom-in with arrows)**.

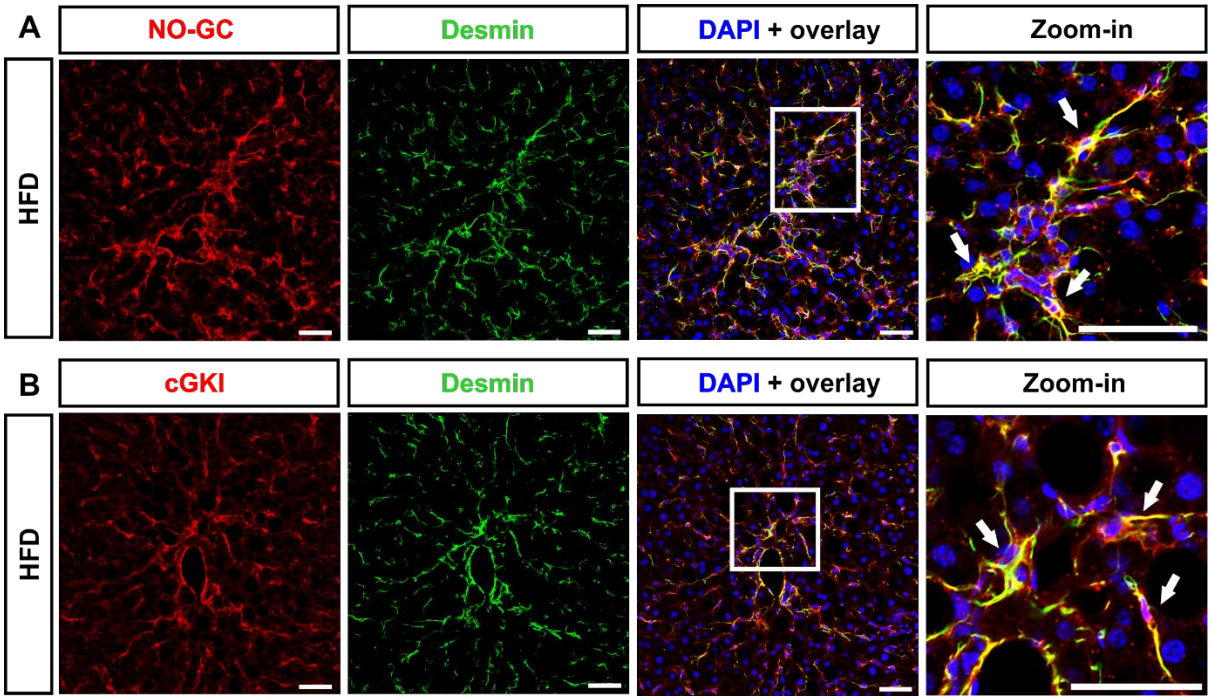

Figure 18: Co-immunostaining analysis of NO-GC and cGKI with desmin. (A) IF co-staining of HSC marker desmin with NO-GC on liver sections from a HFD mouse. **(B)** IF co-staining of HSC marker desmin with cGKI on liver sections from a HFD mouse. Panels show for each image (from left to right) single staining of NO-GC, desmin and cGKI, desmin, an overlay picture (Red: NO-GC or cGKI; Green: desmin; Blue: nuclei (FluorCare DAPI)) and a zoom-in region with arrows indicating colocalization of desmin with NO-GC or cGKI. The Scale bars are 50 µm. n=1 mouse with 3 sections co-stained for NO-GC and Desmin; 3 sections co-stained for cGKI and Desmin. HFD- ApoE KO mice on HFD.

3.3 The cGMP signalling pathway in primary HSCs in culture

Primary HSCs in culture are a suitable means for various cell-based assays and to investigate liver function and physiology. High purity isolation of HSCs from mouse livers has been previously established [65, 157, 158]. When cultured on uncoated coverslips or on Petri dishes, HSCs become activated over time and undergo a phenotypic transition from a quiescent to a proliferative, activated phenotype [159, 160]. This process of transdifferentiation reflects the hallmarks of this cell type that occurs during hepatic fibrosis. Therefore, we used this approach to further corroborate the existence of a functional NO/cGMP pathway in an *in vitro* setting. HSCs in culture were used for immunofluorescence staining and real-time cGMP imaging.

3.3.1 HSCs in culture undergo phenotypic modulation to an activated state

HSCs were isolated from male wild-type mice and grown on 12 mm glass coverslips (100,000 cells per coverslip) in 24-well plates for a period of 8 days. HSCs were recognized via their distinct retinoid-containing lipid droplets. These retinoids have endogenous autofluorescence and were visualized using a fluorescence microscope (excitation 340 nm and emission > 480 nm). During the 8-day culture period, the cells changed their morphology and lipid droplet content and exhibited features associated with activation.

On day 1, HSCs were smaller in size with short cytoplasmic extensions and numerous retinoid droplets. The two main signs of HSC activation were apparent from day 4 in culture when the cells began to change their morphology and started losing the retinoid droplets. Finally, by the 8^{th} day, HSCs displayed elongated cell bodies with numerous processes and less retinoids, as observed by loss of white bubbles in **(Figure 19A)** and autofluorescence **(Figure 19B)** indicating their transdifferentiation, possibly into an activated phenotype. For a better visualization of changes in cell size, HSCs that expressed a YFP-containing protein in their cytosol were isolated from a transgenic mouse **(Figure 19B)**. We examined the increase in cell size by measuring the area of single HSCs (3 coverslips per day). After 1, 4, and 8 days in culture, the average size of HSCs was 575 μm^2 145, 2647 μm^2 ± 66, and 9557 μm^2 ± 358 respectively. This represented approximately a significant 16-fold increase in cell size from day 1 to day 8 **(Figure 19C)**.

The expression of the classical HSC activation marker α-SMA was consistently observed in HSCs from day 1 to day 8 **(Figure 19D)**. The presence of α-SMA as early as day 1 in culture suggests that HSC activation could start directly after their isolation. We observed that the α-SMA stained cells appear much smaller in size when compared to the live cells visualized using YFP fluorescence. This could likely be due to a fixation artefact, causing the cells to shrink.

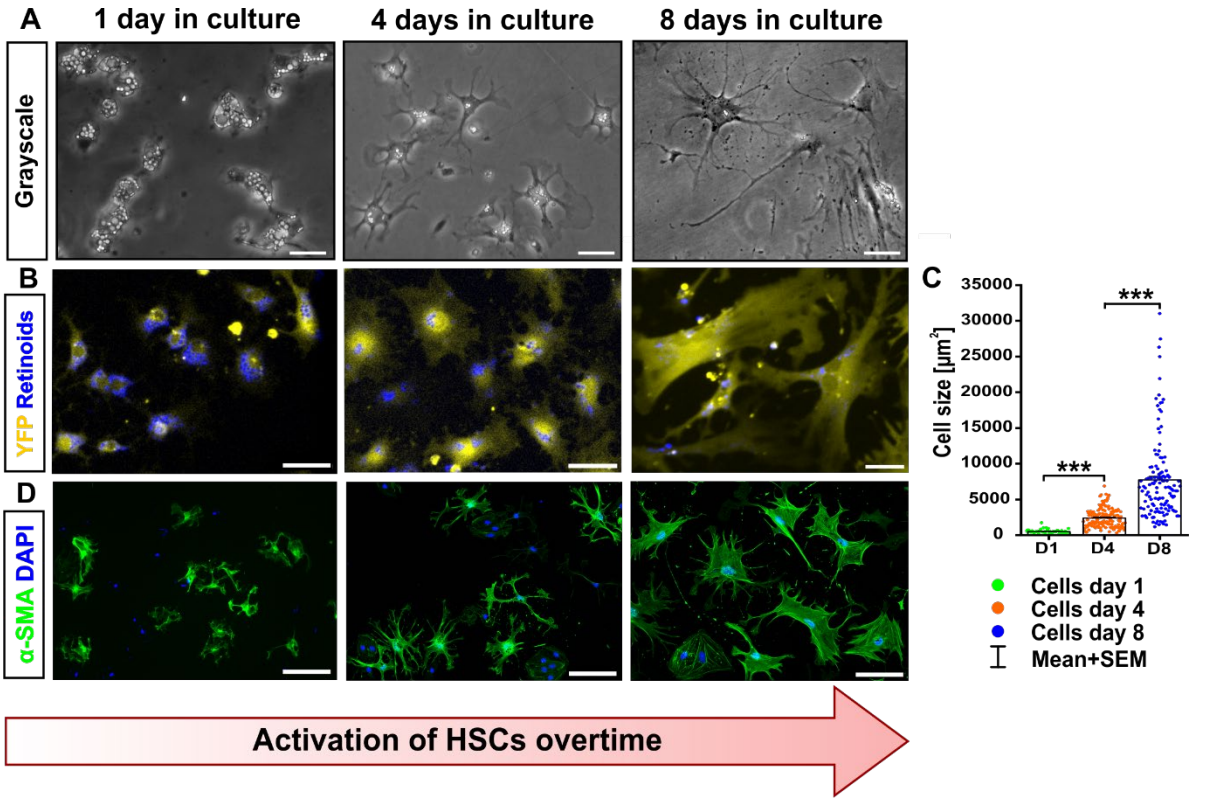

Figure 19: Characterization of hepatic stellate cells in culture. (A) HSCs in culture on days 1, 4, and 8. **(B)** Fluorescently labelled HSCs (YFP) isolated from a cGMP sensor mouse and retinoids (blue) visualized by autofluorescence of vitamin A. **(C)** Analysis of cell size on days 1, 4, and 8. Day 1 (n= 44 cells), day 4 (n= 145 cells), and day 8 (n= 127 cells) in culture (3 coverslips per day, HSCs isolated from one mouse). **(D)** α-SMA IF staining in cultured HSCs. Data are represented as mean ± SEM. Statistical significance with the Mann-Whitney U test is indicated by asterisks (***p<0.0001). The scale bars are 50 µm.

3.3.2 HSCs in culture express proteins of the cGMP pathway at all stages

After analysing the transdifferentiation of HSCs in culture, we checked the expression pattern of cGMP pathway proteins in early and late-stage. HSCs isolated from mouse liver were cultured on coverslips and were fixed after days 1, 4, and 8. IF staining was performed on all coverslips simultaneously to have comparable results. The cells were stained via IF for NO-GC, cGKI, and the HSC marker desmin (green). The cell nuclei were stained with Hoechst 33258 and three regions per coverslip were documented for each staining. Desmin staining was observed in short thickened filamentous structures in the cell cytoplasm extending to the processes at all stages **(Figure 20A)**. Both NO-GC **(Figure 20B)** and cGKI **(Figure 20C)** were also expressed during all stages. The expression was predominantly localized in the cytosol around the cell nucleus. Unlike the cell size, the intensity of the staining did not seem to change over time for all three markers.

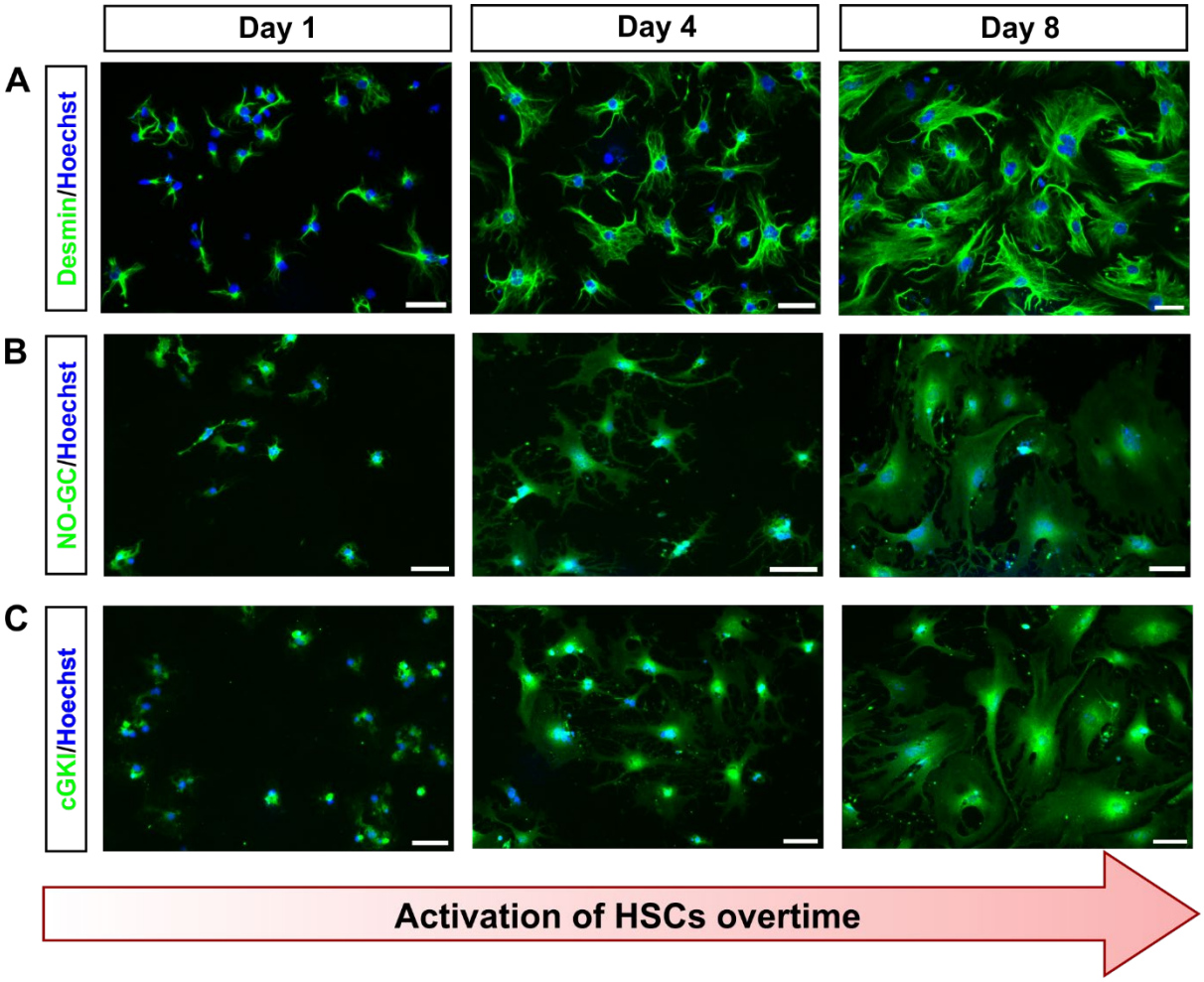

Figure 20: Expression of desmin, NO-GC, and cGKI, in cultured HSCs. (A) IF staining of desmin on days 1, 4, and 8. **(B)** IF staining of NO-GC on days 1, 4, and 8. **(C)** IF staining of cGKI on days 1, 4, and 8. The scale bars are 50 µm. HSCs are isolated from one mouse liver.

3.3.3 HSCs in culture generate cGMP

To investigate cGMP generation in real-time, FRET-based cGMP imaging was performed. We isolated primary HSCs from sensor mice expressing the cGMP biosensor cGi500 globally (cGi-L1) and cultured them for a period of 8 days. Partially confluent HSC cultures were used for FRET measurements. To prevent overcrowding in the field of view (FOV), particularly on day 8 when the cell size increases, 10,000 cells were seeded per coverslip. These sub confluent cultures were stimulated with different compounds and the cGMP/FRET signals were recorded on day 2 and day 8. cGMP signals were differentiated from artefacts by the opposite movement of the single channels (YFP decrease and CFP increase). The traces in black, blue, and yellow represent CFP/YFP ratio, the CFP trace, and the YFP trace, respectively. Retinoid-containing HSCs on day 2 expressed the cGMP sensor cGi500 in their cytosol as observed by the YFP fluorescence **(Figure 21A)**. On this 2nd day of measurement, the cells were first

stimulated with the NO donor DEA/NO (hereafter referred to as NO). In **Figure 21B**, cGMP signals from the representative cell (marked in figure 21A) are shown. This cell showed cGMP generation in response to 50 nM NO **(Figure 21B; black curve, peak 1)**.

After stimulating the cells with NO, we tested the effect of a novel NO-GC activator tool compound (Act) from Bayer (dissolved in DMSO) on the same cells, and recorded their cGMP responses. Prior to applying the activator, we measured the cells with 0.02% DMSO to ensure that the cGMP signals elicited in response to the activator were a result of the compound and not influenced by its solvent, DMSO. Notably, the representative cell did not respond to DMSO **(Figure 21B; black curve, 2nd application)**. Out of the 74 cells measured in the FOV, none exhibited a reaction to DMSO, whereas 53 cells responded to NO. Subsequently, the cells were stimulated with the activator compound at increasing concentrations of 1 nM, 10 nM, 50 nM, and 100 nM. We observed concentration-dependent cGMP responses, with particularly robust signals detected at 50 and 100 nM **(Figure 21B; black curve, peaks 2-5)**.

Towards the end of the measurement, the stimulation with NO for a second time led to only a slight elevation in the cGMP levels, in contrast to the first NO application **(Figure 21B; black cure, peak 6)**. This difference could be attributed to the time it took for the signals from activator compound to return to the baseline, resulting in longer FRET measurements. It is noteworthy to mention that despite multiple stimulations, the cells still reacted to NO at the end of the experiment. The 53 cells reacting to NO also showed cGMP increases in response to the activator. The peak height and area under the curve (AUC) were determined as shown in **(Figure 21C-D)**.

The FRET measurements were repeated with HSCs on day 8. By this stage, HSCs had increased in size and lost majority of their retinoid droplets. The expression of the cGMP sensor cGi500 appeared comparatively weaker than in day 2 HSCs **(Figure 21E)**. Nevertheless, by stimulating the cells with similar drug concentrations as that of day 2, we observed cGMP signals in response to NO and the activator **(Figure 21F; black curves)**. Out of 63 cells measured within the FOV, 27 cells showed cGMP generation in triggered by NO and the activator. The peak height and AUC were determined as shown in **(Figure 21G-H)**. Collectively, these findings demonstrate the presence of a functional NO/cGMP signalling pathway in primary cultured

HSCs on both day 2 and day 8, indicating that cGMP elevation can be achieved through stimulation with NO and the activator.

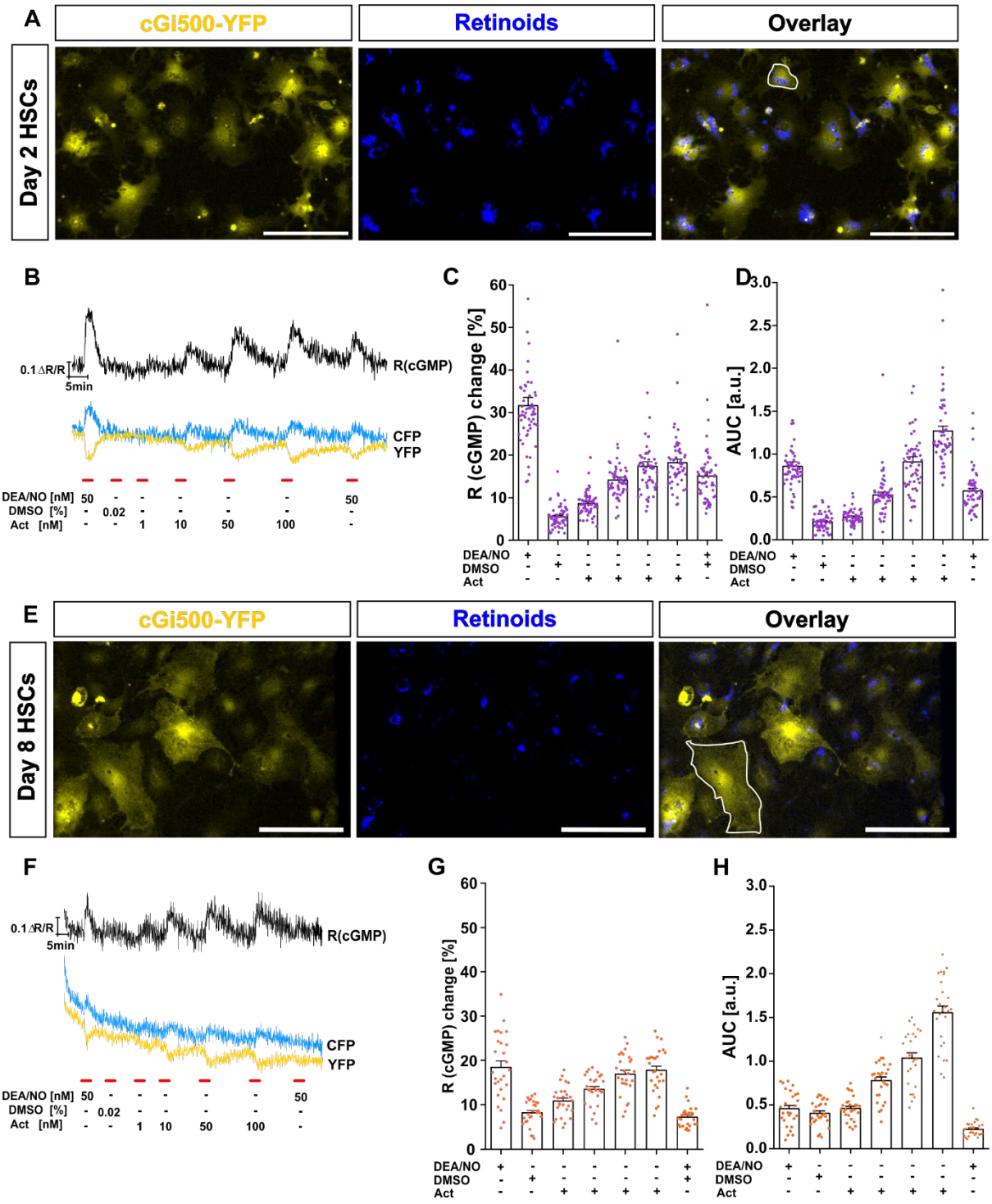

Figure 21: cGMP/FRET measurements with HSCs on day 2 and day 8 (A) Day 2 HSCs in culture isolated from cGi500 mouse liver. Panel shows (from left to right) sensor expression (YFP channel), retinoids (autofluorescence in blue) and an overlay with a single cell marked. **(B)** Representative cGMP/FRET of the exemplary cell on day 2. Black traces represent CFP/YFP ratio R, which indicates cGMP concentration changes recorded in the marked cell in response to NO (50 nM), DMSO (0.02 %), and Act (1 nM, 10 nM, 50 nM, and 100 nM). Blue and yellow traces represent separation of CFP and YFP. **(C)** Analysis of peak height represented as R (cGMP) change and **(D)** area

under the curve (AUC) of all cells in the FOV on day 2. **(E)** Day 8 HSCs in culture isolated from cGi500 mouse liver. Panel shows (from left to right) sensor expression (YFP channel), retinoids (autofluorescence in blue) and an overlay with a single cell marked. **(F)** Representative cGMP/FRET responses of the exemplary cell on day 8. Black traces represent CFP/YFP ratio R, which indicates cGMP concentration changes recorded in the marked cell in response to NO (50 nM), DMSO (0.02 %), and Act (1 nM, 10 nM, 50 nM, and 100 nM). Blue and yellow traces represent separation of CFP and YFP. **(G)** Analysis of peak height represented as R (cGMP) change and **(H)** area under the curve (AUC) of all cells in the FOV on day 8. Data area represented as mean ± SEM. On day 2, a total of 74 cells were measured in the FOV and 53 cells responded to NO and the activator. On day 8, a total of 63 cells were measured in the FOV and 27 cells responded to NO and the activator. FRET measurement was performed with 2 coverslips each on day 2 and day 8.

Our findings demonstrate the presence of an active NO/cGMP signalling pathway in HSCs of healthy and MASH livers in our HFD-induced MASH ApoE KO mouse model. *In vivo*, the cGMP generator NO-GC and its downstream effector cGKI were upregulated during MASH. Using a cell culture model, we could show that NO-GC and cGKI are present in early and late-stage activated primary HSCs. Furthermore, live-cell cGMP imaging demonstrated increased cGMP levels in cultured HSCs in response to NO donor DEA/NO and a novel NO-GC activator tool compound from Bayer. NO-GC activators, in contrast to NO-GC stimulators can activate the oxidized, heme-free form of NO-GC. Considering that MASH is marked by high oxidative stress, our data points towards a therapeutic potential of the NO-GC activator for MASH, especially in cases when endogenous NO might fail to activate the cGMP signalling pathway in activated HSCs.

3.4 Pharmacological modulation of the NO/cGMP pathway in MASH mice

Considering the connection between MASH and atherosclerosis, it is important to recognize that the treatment of one condition could potentially impact the other. As mentioned earlier in section 3.2, the NO/cGMP/cGKI pathway plays a role in both of these diseases. Therefore, it is worth noting that the pharmacological modulation of this pathway might be a promising therapeutic target.

Interestingly in the liver, most studies focussed on exploring the therapeutic potential of NO-GC stimulators (act on the reduced, NO-sensitive form of NO-GC) in models of MASH, induced via CD-HFD [13, 14, 109]. To the best of our knowledge, no study has investigated the effect of NO-GC activators specifically in the context of MASH, with most studies directed towards other liver disease models like TAA-induced cirrhosis [156] and BDL-induced cirrhosis [15]. Based on our results so far, we hypothesized that the NO-GC activator can increase cGMP

generation in our comorbidity mouse model of MASH and atherosclerosis and can thereby influence the progression of MASH. The effect of the NO-GC activator on MASH was analysed in ApoE KO mice fed a HFD for 18-weeks mixed with the activator (HFD+Act mice) and compared to ApoE KO mice on HFD alone (HFD mice).

3.4.1 Treatment with the activator improved hepatocyte ballooning and liver enzyme levels

Initially we assessed hepatocyte ballooning, one of the early onsets of fatty liver disease that results in hepatocyte damage. H&E staining showed reduced hepatocyte ballooning in activator treated mice. In comparison to the HFD group, male activator treated mice displayed a healthy liver parenchyma with sparse accumulation of lipid vacuoles in the peri-portal areas **(Figure 22A, lower panel indicated as PP)**. Similar effect was observed in female animals as well (Figure not shown). The hepatocytes were not swollen and had a well-defined centrally located nucleus **(Figure 22A, lower panel indicated with arrows)**.

The staining was quantified by manually counting the number of lipid vacuoles surrounding the portal vein. Within the male group, a total of 79 portal vein regions (2-3 regions per section) were analysed. The average count of lipid vacuoles was 177 ± 30.8 in male HFD mice (counted in 18 sections from 6 mice) and 60 ± 11.4 in male HFD+Act mice (counted in 12 sections from 4 mice) **(Figure 22B)**. Within the female group, a total of 105 portal vein regions (2-3 per region) were analysed. The average count of lipid vacuoles was 93 ± 10.8 in female HFD mice (counted in 27 sections from 9 mice) and 47 ± 11.7 in female HFD+Act mice (counted in 9 sections from 3 mice) **(Figure 22C)**. When compared to the HFD group, both male and female activator treated mice showed a significantly reduced number of lipid vacuoles.

Next, we assessed the liver function by measuring the serum levels of aspartate transaminase (AST) and alanine transaminase (ALT) in international units per litre (U/l). Predominantly found in the liver, these enzymes are released into the bloodstream and elevated levels indicate liver damage. Due to a high variation, significantly lower ALT levels in the serum were only found in male mice treated with the activator in comparison to the HFD group **(Figure 22E)**. Both male and female HFD+Act mice seem to show a trend towards reduced serum levels of AST and ALT in comparison to the HFD group, with a comparatively mild effect observed in females

(Figure 22D, F, G). Further serum analysis with a large cohort of animals is planned to obtain more definitive results.

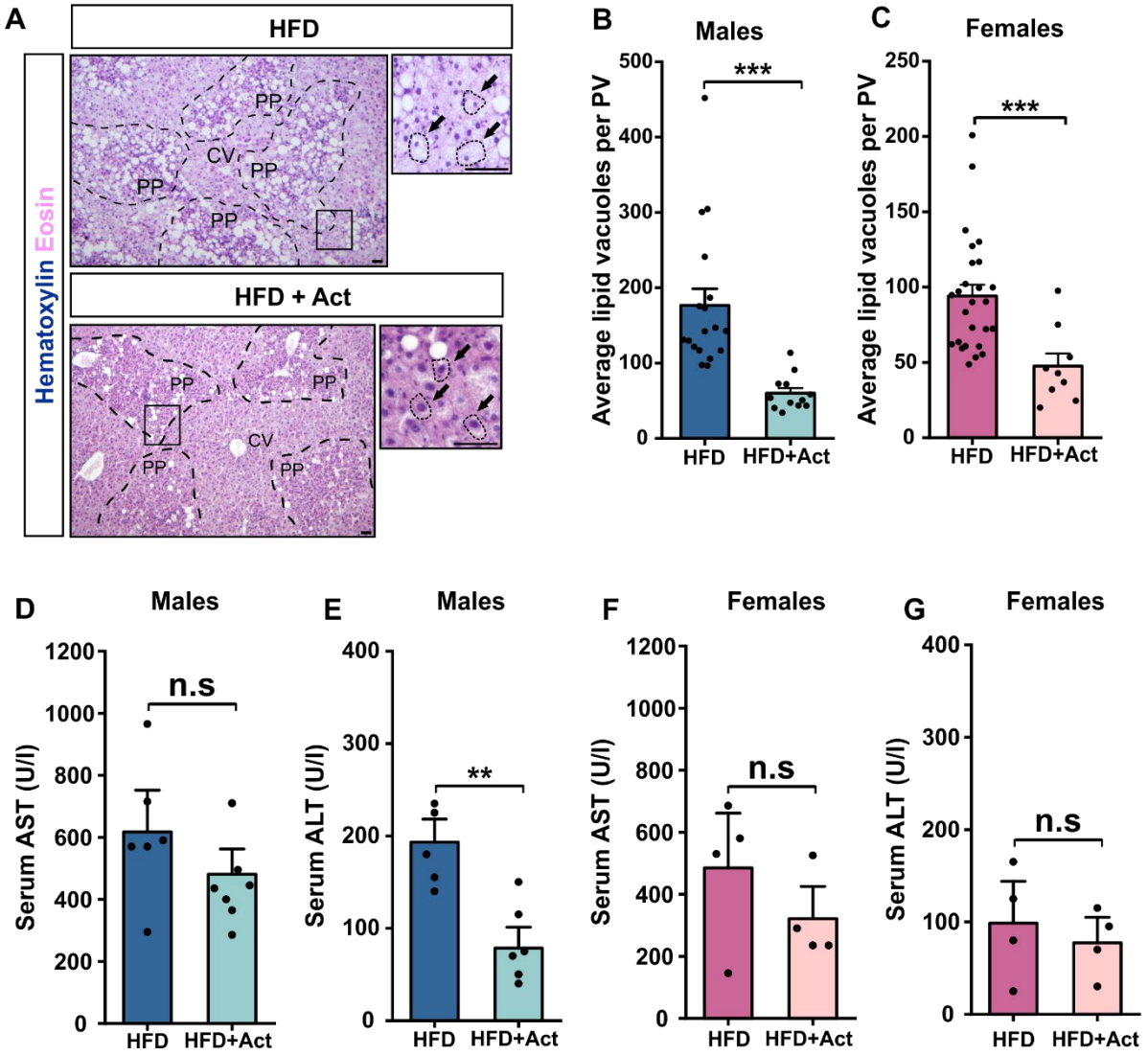

Figure 22: Effect of activator on hepatocellular ballooning and liver enyzmes. (A) Representative H&E staining on paraffin liver sections from HFD and HFD+Act mice. Panels show (from left to right) an overview picture and magnification with arrows denoting the structure of hepatocytes. Regions marked with CV indicate central vein and PP peri-portal areas. **(B)** Average count of lipid vacuoles per portal vein in male HFD (n=6 mice) and HFD+Act (n=4 mice) groups. Data points represent the number of sections analysed. **(C)** Average count of lipid vacuoles per portal vein in female HFD (n=9 mice) and HFD+Act (n=3 mice) groups. Data points represent the number of sections analysed. **(D, E)** Serum levels of AST and ALT in male HFD (n=5-6 mice) and HFD+Act (n=6-7 mice) groups. **(F, G)** Serum AST and ALT levels in female HFD (n=4 mice) and HFD+Act (n=4 mice) groups. Data are represented as mean ± SEM. Statistical significance with the Mann-Whitney U test is indicated by asterisks or n.s (*** $p<0.001$; ** $p<0.01$; n.s $p>0.05$). The scale bars are 50 µm. HFD- ApoE KO mice on HFD; HFD+Act- ApoE KO mice on HFD with activator.

3.4.2 Treatment with the activator shows a tendency of reduced hepatic inflammation

Inflammation is a physiological response to tissue injury or infection that triggers the release of several inflammatory mediators like cytokines and chemokines. These substances mediate

cellular defence mechanisms and aid in tissue repair. However, in fatty liver disease, prolonged inflammatory activity over time leads to chronic inflammation contributing to the emergence of MASH [161]. Lipid induced hepatocyte injury (ballooning), accumulation of triglycerides and lipid metabolites among other cues outside the liver trigger hepatic inflammation in MASH [82]. Therefore, we took a closer look at the effect of activator on liver inflammation. We used Mac-2 (Galectin-3) and F4/80 which are the two well-known biomarkers for inflammation used to identify tissue resident macrophages. IHC and IF staining was performed on paraffin and frozen liver sections from HFD and HFD+Act mice.

We observed a significant decrease in the Mac-2 positive area within the livers of activator-treated mice in comparison to the HFD group **(Figure 23A, right panel)**. As there were no nuclei staining present, we analysed Mac-2 expression by quantifying the proportion of the area that displayed positive Mac-2 staining. This revealed 1.2-fold decrease in Mac-2 positive area in HFD+Act (10 % ± 0.4; 15 sections from 5 mice) compared to the HFD group (12 % ± 0.6; 12 sections from 4 mice) **(Figure 23B)**. On the other hand, we observed only a tendency towards reduced F4/80 expression in the activator-treated mice compared to the HFD group **(Figure 23C, right panel)**. This is likely due to the high variation between samples. The percentage of F4/80 positive cells were 24 % ± 8 (3 sections from 3 mice) in the HFD group and 17 % ± 2.5 (3 sections from 3 mice) within HFD+Act group **(Figure 23D)**.

We then performed RT-PCR to analyse locally expressed proinflammatory cytokines- IL-6, IFNG, IL1A, TNFα and chemokines CCL2 and CXCL10. Mice treated with the activator exhibited a tendency towards decreased expression of these inflammatory markers, with the exception of CCL2, which showed a significant reduction **(Figure 23E)**.

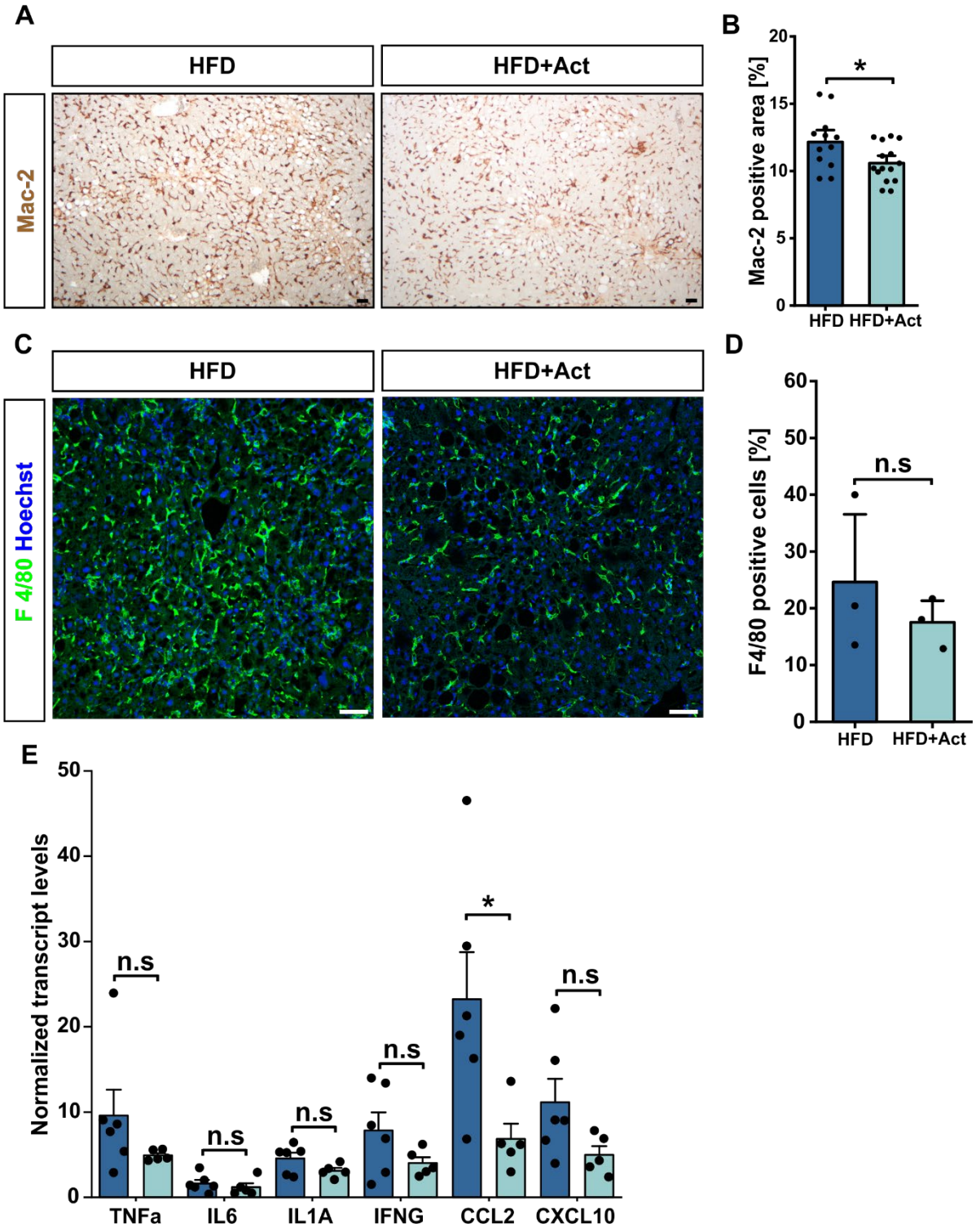

Figure 23: Effect of activator on hepatic inflammation. (A) Representative IHC staining of Mac-2 on paraffin liver sections from HFD and HFD+Act mice. **(B)** Quantification of percentage of mac-2 positive area in male HFD (n=4 mice) and HFD+Act (n=5 mice) groups. Data points represent the number of sections stained. **(C)** Representative IF staining of F4/80 on frozen liver sections from HFD and HFD+Act mice. **(D)** Quantification of percentage of F4/80 positive cells in male HFD (n=3 mice) and HFD+Act (n=3 mice) groups. Data points represent the number of mice per each group. **(E)** mRNA levels of proinflammatory markers in male HFD (n=6 mice) and HFD+Act (n=5 mice) liver tissues. Data are represented as mean ± SEM. Statistical significance with the Mann-Whitney U test and Two-sample T-test is indicated by asterisks or n.s (* $p<0.05$; n.s $p>0.05$). The scale bars are 50 µm. HFD- ApoE KO mice on HFD; HFD+Act- ApoE KO mice on HFD with activator.

3.4.3 Treatment with the activator leads to diminished liver fibrosis

Next, we examined hepatic fibrosis which is the consequence of excessive collagen deposition in the liver caused by HSC activation. To analyse HSC activation, we performed α-SMA staining on paraffin liver sections from HFD and HFD+Act mice. α-SMA expression was enhanced in the HFD group, especially in the peri-portal area **(Figure 24A)**. We observed an increased amount of α-SMA positive aHSCs mainly concentrated in the fibrotic areas of the portal tracts **(Figure 24A right, arrows)**. Conversely, treatment with the activator demonstrated a significant reduction in α-SMA expression along with a decreased number of α-SMA positive aHSCs in the periportal areas **(Figure 24B right, arrows)**. The percentage of α-SMA positive area was 3.1 % ± 0.1 in the HFD group (20 sections from 5 mice) and 1.3 % ± 0.3 in the activator treated group (16 sections from 5 mice) **(Figure 24C)**. This data was confirmed by a significant reduction in ACTA2 (gene name for α-SMA) transcript levels observed in mice treated with the activator compared to those in the HFD group **(Figure 24D)**.

Next, we performed PSR/FG staining to assess collagen deposition. Treatment with activator led to a decrease in peri-portal fibrosis and collagen fibre accumulation within the liver parenchyma in comparison to the HFD group **(Figure 24E-F)**. Quantitative analysis revealed a significant 6-fold reduction in PSR-positive area in male HFD+Act mice (0.8 % ± 0.1; analysed in 15 sections from 5 mice) in comparison to the HFD group (5.5 % ± 1.5; analysed in 18 sections from 6 mice) **(Figure 24G)**. Female mice treated with the activator showed only a 1.6-fold decrease in PSR-positive area (1.9 % ± 0.7; analysed in 9 sections from 3 mice) in comparison to the HFD group (3.1 % ± 0.7; analysed in 18 sections from 6 mice) **(Figure 24H)**. These results further align with our observations of a diminished accumulation of ECM protein collagen IV in HFD+Act (1.5 % ± 0.2; analysed in 9 sections from 3 mice) when compared to the HFD group (8.3 % ± 1.2; analysed in 9 sections from 3 mice) **(Figure 24I-J)**.

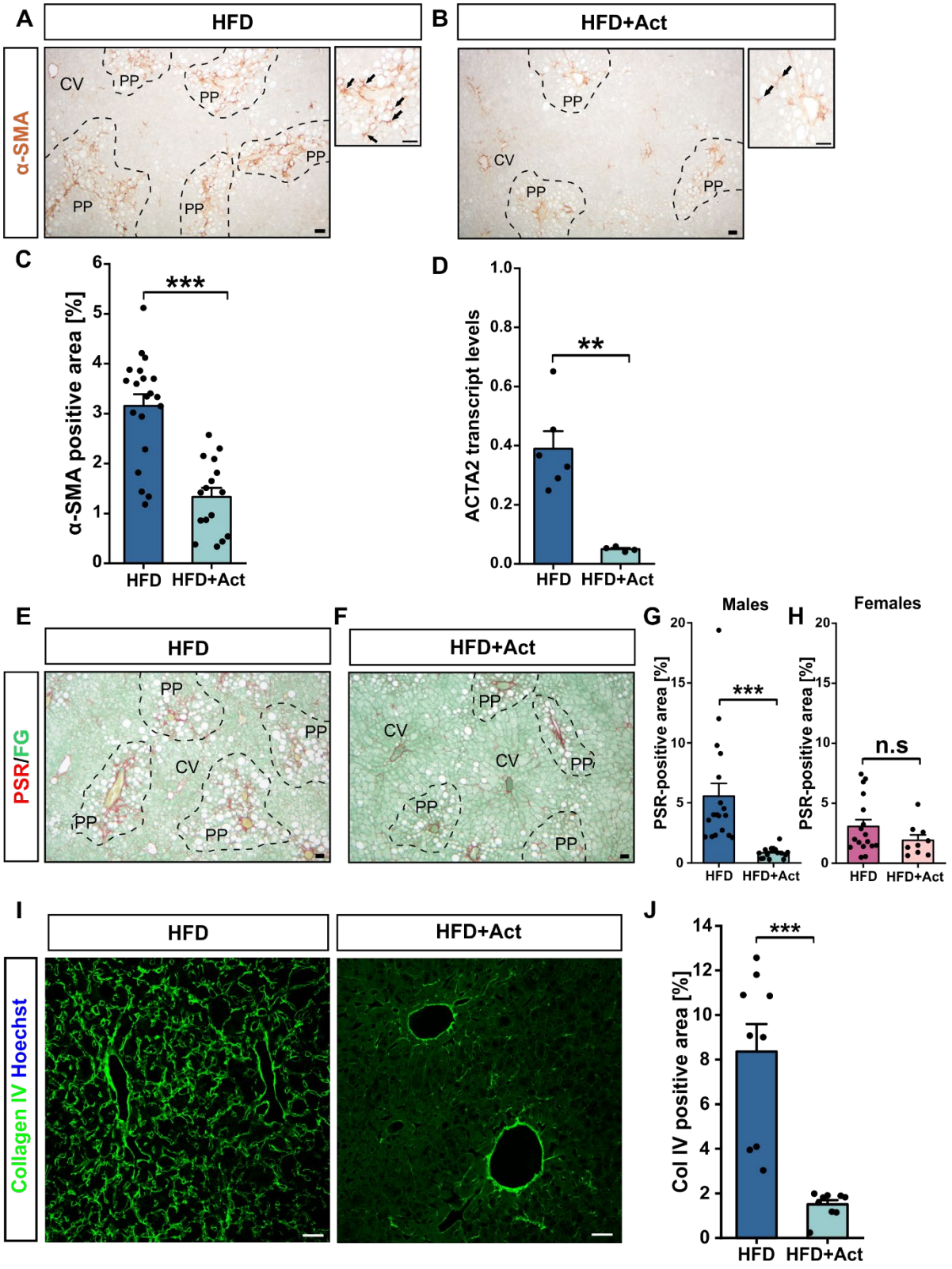

Figure 24: Effect of activator on hepatic fibrosis. (A, B) Representative images of α-SMA staining on paraffin liver sections from **(A)** HFD and **(B)** HFD+Act mice. **(C)** Quantification of α-SMA positive area in male HFD (n=5 mice) and HFD+Act (n=5 mice) groups. Data points represent sections analysed. **(D)** RT-PCR analysis of ACTA2 mRNA levels in male HFD (n=6) and HFD+Act (n=4) mice. **(E, F)** Representative images of PSR/FG staining on paraffin liver sections from **(E)** HFD and **(F)** HFD+Act mice. **(G)** Quantification of PSR-positive area in male HFD (n=6 mice) and HFD+Act (n=5 mice) groups. Data points represent sections analysed. **(H)** Quantification of PSR-positive area

in female HFD (n=6 mice) and HFD+Act (n=3 mice) groups. Data points represent sections analysed. **(I)** Representative images of collagen IV staining on frozen liver sections from HFD and HFD+Act mice. **(J)** Quantification of collagen IV positive area in male HFD (n=3 mice) and HFD+Act (n=3) groups. Data points represent sections analysed. Data are represented as mean ± SEM. Statistical significance with the Mann-Whitney U test is indicated by asterisks or n.s (** $p<0.01$; *** $p<0.001$; n.s $p>0.05$). The scale bars are 50 µm. HFD- ApoE KO mice on HFD; HFD+Act- ApoE KO mice on HFD with activator.

Together, these experiments highlight the therapeutic potential of the novel NO-GC activator in ameliorating the pathological phenotype of MASH livers. The activator effectively improved hepatocyte ballooning, hepatic fibrosis, and showed a tendency towards reducing liver inflammation and enzyme levels.

4 Discussion

This study established a diet induced mouse model for MASH in the presence of ApoE KO and has examined the steatotic liver disease spectrum from MASLD to MASH in male and female mice. Additionally, we investigated the cellular dynamics of HSCs in a healthy liver and during disease pathogenesis. For the first time, the expression pattern of cGMP pathway components- NO-GC and cGKI were analysed in the context of MASH in an ApoE KO+HFD mouse model. In line with the existing data, our model showed features of human MASH, HSC activation [84, 113], and confirmed the expression of NO-GC and cGKI in HSCs [14, 73, 74]. It is also for the first time that the spatiotemporal dynamics of cGMP signals in response to a NO donor and a novel NO-GC activator were demonstrated in early-stage (day 2) and late-stage (day 8) primary HSCs. Lastly, we tested the therapeutic potential of the novel NO-GC activator in the progression of disease from MASLD to MASH. Taken together, our findings report that components of the NO/cGMP pathway- NO-GC and cGKI as markers for HSCs and points towards the development of treatment approaches targeting the cGMP signalling pathway for MASLD therapy.

4.1 ApoE KO+HFD as a mouse model for MASH

MASH was induced using ApoE KO mice fed a HFD (HFD), which were compared to WT mice on a ND (ND). In humans, the development of MASH is often attributed to caloric excess (consuming a diet high in fat and fructose) and a sedentary lifestyle. ApoE is a protein involved in lipid metabolism [162] and its absence, among others, leads to obesity and metabolic syndrome which are the common risk factors for MASH [143]. Therefore, upon combining these two aspects, our mice became obese and in turn developed fatty liver and MASH. The

model we used here is based on a current model [84, 113] to which we have done a slight modification by extending the feeding timeline to 18 weeks. In addition to MASH, our mice also developed atherosclerosis simultaneously. This again is another aspect which closely mimics the real-life setting, because in humans, the development of fatty liver disease often goes hand in hand with other comorbidities including atherosclerosis due to the presence of shared risk factors [134]. On the other hand, a limitation of our model is its inability to mimic advanced stages of the fatty liver disease spectrum, such as cirrhosis and HCC. To address this deficiency, Wolf et al. introduced the choline deficient high-fat diet (CD-HFD) model [117]. This model led to spontaneous development of HCC after 12 months of feeding. However, despite its ability to induce the complete MASLD spectrum, this approach is extremely time consuming. Throughout our experiments, the mice displayed no signs of stress or adverse health effects, indicating that our model is less rigorous in comparison to the MCD diet model, where mice are hypermetabolic and experience substantial weight loss [118].

4.1.1 Physiological alterations in ND and HFD mice

After 18-weeks on an HFD, both male and female mice showed a significant increase in their body weight in comparison to the ND mice **(Figure 13A-B)**. This weight gain could be attributed to the consumption of the HFD and the absence of ApoE, which in the liver is normally secreted by hepatocytes [163]. The deficiency of ApoE impairs the hepatocytes' ability to metabolize surplus fats. Consequently, fat accumulates in the liver and other parts of the body, resulting in abnormal weight gain. In line with weight gain, both male and female HFD mice exhibited hepatomegaly, a condition characterized by an abnormal increase in liver weight **(Figure 13C-D)**. These data align with previously documented findings of elevated body and liver weight during MASH in ApoE KO mice on a HFD [84, 113]. These observations further correlate with the link between weight gain and increased risk of MASLD development in humans [164].

4.1.2 Pathophysiology of MASH

After analysing the physiological alterations, this study went on to characterize the pathogenesis of MASH in both sexes on ND and HFD. Long-term feeding of HFD in the absence of ApoE led to intrahepatic fat accumulation resulting in steatosis **(Figure 14A-C)**. This represented the first histopathological sign of MASH in our model. The build-up of fat in the livers of HFD mice could be due to abnormal lipid metabolism which was not the case in ND

fed WT mice. However, literature suggests that there are several other mechanisms which could lead to intrahepatic fat accumulation. These include increased free fatty acid (FFA) influx, increased de novo lipogenesis, and clearance of fat via β oxidation or VLDL secretion [87]. These factors give rise to oxidative stress by altering the oxidant/antioxidant balance in the liver, which leads to cellular dysfunction, injury, and cell death [165].

We did not test for these factors in our model, however, the series of findings we observed following steatosis indicated that one or more of these mechanisms could be involved. Steatosis was accompanied by an increase in hepatic triglycerides and hepatic cholesterol levels in HFD mice **(Figure 14G-H)**. Under normal circumstances, the liver only stores small amounts FFAs in the form of triglycerides which are then disposed via fatty acid oxidation and secretion in the form of VLDL into the plasma (See section 1.3.2). In case of our HFD animals, there could have been an imbalance between the uptake and elimination of FFAs, leading to the build-up of triglycerides within hepatocytes. This finding is well in line with a previous study [166] although, another study on high-fat diet induced obese rats concluded that triglyceride accumulation might be an ''innocent bystander''. Instead, FFAs or their metabolites might lead to disease progression [167].

High levels of triglycerides and cholesterol were concomitant with changes in plasma LDL levels in our HFD mice as opposed to the ND mice **(Suppl. table IX)**. Because the HFD mice have an impaired lipid metabolism due to the absence of ApoE, the build-up of triglycerides within the liver exceeds its capacity to metabolise them. Therefore, these are secreted into the bloodstream as VLDL where they are converted into cholesterol-rich LDL particles. An increase in cholesterol and LDL levels has also been described in other experimental models of MASH [168, 169] as well as in human MASH [170]. These data suggest that the dysregulation of lipid metabolism in our ApoE KO model supplemented with HFD resembles human MASH.

As a result of metabolic dysfunction and steatosis, the hepatocytes in HFD mice underwent structural changes resulting in hepatocellular ballooning, a finding well in line with previous studies [84, 85, 116]. This was the second histopathological sign we observed in our model. Notably, this ballooning is also a key histological finding used to diagnose the progression of human MASH [144]. In contrast to the hepatocytes in ND mice, those in HFD mice exhibited

an enlargement in size and their nucleus was pushed towards the periphery of the cell **(Figure 14D-E)**. This enlargement can be attributed to the substantial accumulation of fat within the cells, which is prominently visible in the magnified image indicated by arrows **(Figure 14E)**. Another observation in our model was that the liver parenchyma of HFD mice was distorted and had a lot of lipid vacuoles (empty holes) which were otherwise not detectable in the liver sections of ND mice **(Figure 14F)**. However, the severity of ballooning and the amount of lipid vacuoles were less in female HFD mice in comparison to the males. A similar trend was also observed with the levels of triglycerides between both sexes. This seems to be a sex-dependent effect.

Although ballooning is an important phenotype, one particular observation called the Mallory bodies (MB) closely associated with ballooning were lacking in our model. MBs are cytoplasmic inclusions found in hepatocytes which is a peculiar manifestation of hepatocyte cell death and a hallmark of MASH [171]. There could be two possible explanations for their absence in our model: i) their presence might vary depending on the stage and severity of the disease and ii) the use of conventional H&E staining is probably not the best method to visualize and detect them. In this case an IHC staining with an antibody against keratin 18 could be used to identify and visualize MBs. Keratin 18 is an intermediate filament protein that is a component of cytoskeleton in epithelial cells, including hepatocytes [172].

Following steatosis and hepatocyte damage, hepatic fibrosis marked the third histopathological sign in our model. HFD mice developed a significant periportal fibrosis in comparison to the ND mice characterized by increased collagen deposition in these areas **(Figure 15A-C)**. The periportal area encompasses the portal vein, hepatic artery, and the bile duct, distinguishing it from the pericentral area which only contains the central vein. Female mice on HFD exhibited less severe fibrosis compared to their male counterparts **(Figure 15D; blue and pink columns)**. Development of fibrosis correlated with the activation of HSCs in our model, a topic which will be discussed in the following section. A primary factor contributing to HSC activation in our model could be hepatocyte damage followed by subsequent cell death, alongside other contributing factors. This hypothesis can be supported by the close proximity of HSCs and hepatocytes within the perisinusoidal space of Disse, potentially engaging in cell-cell interactions **(Figure 6)**. Therefore, it is plausible that the substances

released by damaged hepatocytes might serve as signalling cues, potentially triggering HSC activation [173].

In addition to hepatocyte damage, our ApoE KO with HFD model itself establishes a chronic liver disease setting in which HSC activation is known to occur. As mentioned previously, HSCs are responsible for maintaining the three-dimensional architecture of the liver by secreting correct amounts of ECM components and their degrading enzymes [66] (see section 1.3.2). In our model, the disruption of this tightly regulated mechanism might have led to an excess production of ECM components, particularly collagen, without subsequent degradation, ultimately resulting in scarring. The development of fibrosis in our model is consistent with previous studies in ApoE KO mice fed a WD [84, 113] as well as another experimental models of MASH [168, 169, 174].

4.1.3 HSCs in healthy and in MASH livers

After analysing the pathophysiology of MASH in our model, we sought out to examine HSCs in their ''quiescent'' and ''activated'' states and follow the changes they undergo during transition. At the protein level, both male and female HFD mice showed elevated expression of desmin and SM22 when compared to the mice on a ND **(Figure 16A-B)**. As stated earlier, desmin is a marker for HSCs regardless of their state, whether quiescent or activated [92, 148]. Furthermore, recent studies using scRNA-seq have shown that SM22 (Transgelin) is a marker for activated HSCs [72, 152, 153]. Based on our findings, we could deduce that an increase in the expression of desmin and SM22 in the livers of HFD mice indicates HSC expansion and activation which is consistent with the progression of MASH.

The IF staining of desmin on frozen liver sections from both ND and HFD mice provided insights into the morphology changes undergone by HSCs during transition. HSCs within the liver parenchyma of ND and HFD liver sections stained positive for desmin **(Figure 16D-E)**. This observation aligns well with the study conducted by Hoffmann et al. who similarly identified desmin-positive HSCs in the livers of mice on standard diet (SD) and choline-deficient high fat diet (CDHFD) [92]. We distinguished HSCs into quiescent or activated states based on their morphology. HSCs within the livers of ND mice were star-shaped with tiny processes, a feature consistent with a quiescent morphology. In HFD induced MASH livers, HSCs exhibited a myofibroblast like morphology with elongated cell body and long processes, consistent with

an activated phenotype [72]. In addition to the phenotypic change, HSCs within the HFD livers also increased in number **(Suppl. table VIII)**.

Moreover, in accordance with the established dogma that activated HSCs (aHSCs) show enhanced expression of ECM-associated proteins during MASH progression [68], the aHSCs in HFD livers showed increased expression of SM22 **(Figure 16F-G and K)** positive cells and α-SMA positive area **(Figure 16H-I and L)**. α-SMA is a classical marker for HSC activation [149, 151]. Consistent with enhanced periportal fibrosis in HFD livers, we also observed α-SMA positive HSCs in the periportal areas. In this regard, our observations of positive α-SMA staining in aHSCs align with the results shown by others [84, 92]. The studies mentioned earlier have indicated SM22 as an aHSC marker using scRNA-seq. However, our IF staining technique offers more definitive evidence, demonstrating its specific presence in aHSCs within MASH livers.

While these conventional methods have offered us valuable insights, it is important to note that the process of HSC activation is a highly intricate process. Its comprehension cannot be confined solely to the analysis of two classical markers. In this context, Yang et al. utilized both conventional and scRNA-seq techniques in two liver fibrosis models, offering a comprehensive roadmap outlining the sequential stages of HSC activation together with the expression of cell-type specific markers during disease progression [72].

4.2 Distribution of NO-GC and cGKI in healthy and in MASH livers

Previous studies have already demonstrated the existence of NO-GC and cGKI in either MASH or healthy livers using different experimental models. However, our study stands out as the first to simultaneously analyse the expression pattern of these two components in both healthy and in HFD mice bred on an ApoE-deficient background which developed atherosclerosis simultaneously. The cGMP pathway is known to have diverse effects on both disease conditions [175, 176].

NO-GC and cGKI were detected in the livers of mice on both ND and a HFD. Notably, at the protein level, a greater amount of NO-GC and cGKI expression was observed in the HFD group than in the ND group **(Figure 17A-C)**. In line with our findings, Hall et al. have similarly demonstrated an elevation in sGCβ1 expression in a CCl_4 induced liver fibrosis model, in

comparison to mice treated with a vehicle using western blot analysis [14]. We further validated this expression pattern via IF staining. The analysis, including single staining **(Figure 17D-G)** and co-staining **(Figure 18A-B)** revealed that both qHSCs in healthy and aHSCs in MASH livers expressed NO-GC and cGKI, along with the SMCs surrounding the vascular walls.

Our observations regarding NO-GC expression within HSCs are consistent with previous studies [14, 72]. However, they differ with one of these studies in terms of observed levels of expression. We demonstrated an increase in NO-GC expression in aHSCs, while Yang et al. using single cell sequencing reported a steady decrease and absence of Gucy1a1 and Gucy1b1 (gene name of NO-GC α1 and β1 subunits) expression following HSC activation in CCl_4 induced liver fibrosis model [72]. This discrepancy could potentially stem from an increase in the number of cells (aHSCs) expressing NO-GC in our model, likely due to HSC expansion rather than an actual increase in the expression levels itself. While not specifically analysed in our model, it is possible that the expression could decline in advanced stages of MASH, such as in cirrhosis and HCC. Schwabl et al. reported that besides HSCs, hepatocytes, Kupffer cells, and LSECs in both healthy and BDL livers expressed varying levels of NO-GC at the mRNA level [110]. It is important to note here that this was not validated via staining. Moreover, in our data, the hepatocytes were not stained by NO-GC (see section 3.2.1).

The expression of cGKI in the liver has been previously shown by Franko et al. and Lutz et al. [73, 74]. Their studies conclusively demonstrate that genetic ablation of cGKI in all cell types, except for SMCs, resulted in events consistent with metabolic liver disease progression and HSC activation. Furthermore, Lutz et al. specifically demonstrated that within the liver, cGKI is expressed in HSCs but not in Mac-2 positive macrophages [73]. However, these two studies showed cGKI exclusively in HSCs and SMCs of a healthy liver. Our findings on the expression of cGKI in aHSCs of MASH livers as well as in qHSCs of healthy liver **(Figure 17F-G)** represents a new addition to this existing body of knowledge. Akin to NO-GC, we observed an increase in the number of aHSCs expressing cGKI due enhanced expansion. Taken together, the data from our study and others shows the presence of an active cGMP signalling pathway in the liver, with its two primary components predominantly expressed in HSCs. However, several questions remain unanswered.

For instance, why do HSCs still retain the expression of NO-GC and cGKI after activation? If we consider the 'NO-paradox', there is a decreased availability of NO in a diseased liver in contrast to an excess of NO in the peripheral systemic circulation [5]. This leads to impaired downstream NO/cGMP signalling within the liver, setting into motion a cascade of events that progress to liver injury [176]. But it could be likely that the absence of the endogenous ligand does not necessarily imply a complete loss of the signalling axis itself. Perhaps, activated HSCs retain NO-GC and cGKI as a protective mechanism, either to possibly revert back to a quiescent state or to prevent further progression of the liver disease.

This, however, prompts another question: are NO-GC and cGKI still expressed in later stages of MASH? The answer to this question lies outside the scope of this study and our mouse model. The expression pattern of NO-GC and cGKI should be investigated in detail using other mouse models that induce MASH with cirrhosis and HCC.

4.3 *In vitro* characterization of primary HSCs and analysis of cGMP signalling

Based on our *in vivo* data, we have observed a transition in the cellular status of HSCs from a ''quiescent'' to an ''activated'' state. Furthermore, our findings indicate the presence of cGMP pathway components NO-GC and cGKI in both quiescent and activated HSCs. While the *in vivo* setting closely mirrors the human condition, it is not always feasible to perform certain experiments due to the nature of certain organs. This is particularly true for the liver which is highly prone to degradation due to its inherent enzymatic activity. In this regard, *in vitro* studies offer a simplified model to conduct these experiments with ease.

4.3.1 Culture and characterization of primary HSCs

As described earlier, primary HSCs in culture can effectively mimic the characteristic changes associated with transdifferentiation during hepatic fibrosis. This can be achieved by prolonging the cultivation time of HSCs on plastic dishes. To this end, using a previously described protocol [65], we isolated HSCs from WT murine livers and subsequently characterized them. We observed that culturing HSCs on over a period of 8 days resulted in their transdifferentiation to an activated state. This was reflected in their morphological shift from a star-like shape to myofibroblast-like shape, characterized by a progressive loss of retinoid droplets **(Figure 19A-B)** and a significant increase in cell size **(Figure 19C)**. The

observations seen in our cell culture model correlate with those reported by others [177, 178] and our in vivo findings with regard to change in morphology and loss of retinoids [92].

HSC activation was further characterized via IF staining with α-SMA. Although α-SMA is a well-established aHSC marker, in our model we observed its expression in both day 1 as well as day 8 **(Figure 19D)** HSCs. This observation does not align with other studies which observed α-SMA expression only in aHSCs in culture [177-179]. Kawada et al. showed a potential involvement of NO/cGMP pathway in regulating α-SMA expression in rat HSCs [180]. Rat HSCs in culture generated NO in response to LPS and/or INFγ treatment. The NO in turn attenuated α-SMA expression in a cGMP-dependent manner. While we did not test this, it is possible that in our cell culture model, already after 1 day in culture, HSCs may have begun to exhibit subtle signs of activation. Nevertheless, this hypothesis needs to be confirmed by western blotting to see if HSCs from days 1, 4, and 8 express equal amounts of α-SMA at the protein level or if there is a downregulation at the early-stages.

It is important to mention here the challenges that came up in establishing the isolation protocol. The most difficult step was the cannulation of IVC and the subsequent *in situ* perfusion of the liver, which was often not precise enough. Consequently, the liver was not thoroughly digested from within. Another significant challenge was the *in vitro* digestion of the liver with pronase/collagenase and DNase on a heated magnetic stirrer. Although the protocol dictated a 25-minute stir time, we found this duration to be excessively long, resulting in over-digestion. Conversely, a shorter time duration proved inadequate for proper dissociation of the liver cells. Therefore, it was necessary to find a middle ground for optimal digestion. Furthermore, the density gradient centrifugation was considerably difficult. Despite the use of proper settings, the separation of different liver cells did not consistently yield the desired outcome. Amidst various layers, HSCs which are supposed to be visible in a distinct white ring, were difficult to identify given their small proportion. Despite troubleshooting at each stage, the isolation was successful only a handful of times with a moderate yield of cells. On a positive note, all of our isolations were pure without any contamination of other liver cells. Nevertheless, it is crucial to improvise and establish the protocol more thoroughly for conducting future experiments.

4.3.2 cGMP signalling in primary HSCs

After demonstrating the presence of the cGMP signalling pathway in HSCs of healthy and MASH livers on the expression level, we aimed to investigate its functional activity. The activity of NO-GC is susceptible to its environment. For instance, in conditions like MASH where oxidative stress is highly prevalent, oxidation of NO-GC leads to loss of function [24]. In platelets and VSMCs, the function of NO-GC was shown to be flow dependent [181]. Therefore, it is important to verify that the NO-GC/cGMP signalling in a given cell or tissue is functional. Due to technical limitations (e.g., tissue damage and focus drift) we could not perform cGMP/FRET measurements in liver sections. Therefore, we relied on our cell culture model with early (day 1 ''healthy'' liver) and late-stage (day 8 ''MASH'' liver) HSCs. Our cell culture model not only reflected the well-known features consistent with HSC activation during late-stages **(Figure 19A-C)**, but also the expression of NO-GC and cGKI in the cytosol **(Figure 20B-C)**. Desmin being an intermediate filament protein was observed in filamentous structures within the cell cytoplasm extending to the processes **(Figure 20A)**. Interestingly, the expression levels of NO-GC and cGKI were similar in day 1 and day 8 HSCs. This observation was in line with our hypothesis that the increase in NO-GC and cGKI expression in MASH development was based on expansion of HSCs in MASH livers rather than the altered expression levels over time. It is worth mentioning here that the specificity of cGKI expression in primary HSCs was confirmed in an HSC-specific cGKI knockout mouse model by a master's student in our lab **(Master thesis-Miriam Rupprecht)**.

Under physiological conditions, NO mediates its effects by stimulation of NO-GC, leading to the production of cGMP and the subsequent activation of cGKI. Consistent with the expression of NO-GC, we observed robust NO-induced cGMP signals in day 2 and day 8 HSCs isolated from cGi-L1 mice **(Figure 21B and F, black curve, peak 1)**. This finding confirmed that not only is NO-GC functional in early-stage HSCs but also that the expression of remains functional during the late-stage after HSC activation. The relative cGMP produced in response to NO during the time of measurement is depicted by the peak height, while the AUC reflects the total cGMP in the cell **(Figure 21C-D, first column)**. Unexpectedly, we observed a drop in the quality of cGMP/FRET signals (''noisy signals'') from day 2 to day 8 **(Figure 21F, black curve, peak 1)** together with a slight reduction in the relative and total cGMP in response to NO **(Figure 21G-H, first column)**. This reduced signal-to-noise ratio in day 8 HSCs rather reflected

technical problems than a reduced expression of functionally active NO-GC. The bad signal-to-noise ratio is most likely attributed to the drop in the sensor fluorescence due to the extensive spreading of HSCs on day 8 **(Figure 21E, YFP image)**. The strong autofluorescence of retinoids in HSCs could be excluded as a cause. The autofluorescence is primarily excited by wavelengths shorter than 400 nm [182, 183] whereas, the CFP of our FRET sensor was excited at 445 nm. Furthermore, most of the HSCs in culture lost their retinoids by day 8 **(Figure 21E, retinoids image)**. Despite these technical difficulties, we could demonstrate that the acute and total cGMP responses recorded in HSCs on day 2 and day 8 were nearly similar, indicating that cGMP generation in HSCs is independent of their activation state *in vitro*.

NO-induced cGMP generation in HSCs and the subsequent activation of cGKI has been shown to regulate a plethora of functions. For instance, the findings from Perri et al. indicated that increased cGMP generation in response to NO significantly attenuated serum-induced contraction of normal rat HSCs [184]. They also reported that *in vivo* activated HSCs isolated from bile duct ligated (BDL) rats and the immortalized HSC cell line LX2 failed to generate cGMP in response to NO. This could be true considering the fact that the NO/cGMP signalling is impaired during liver disease. However, it is worth noting that the cGMP levels in these experiments were measured using RIA. This technique could be less sensitive and reliable due to the need for incubating cells with a PDE inhibitor to prevent cGMP degradation overtime. Multiple studies utilizing the LX2 cell line have indicated that the activation of NO/cGMP signalling is involved in regulation of HSC migration [185] and adhesion [186]. While these findings highlight the importance of the cGMP pathway in influencing HSC dynamics, it is essential to note that the use of an immortalized cell line does not fully replicate the *in vivo* phenotype. In our model, we cultured primary HSCs and validated that they are able to closely mimic the *in vivo* setting. Furthermore, our model of in-culture activation of HSCs allowed us to compare cGMP signalling between HSCs from the same mouse, thereby removing the confounding factors present in other models. Together with high spatiotemporal resolution and sensitivity of our cGMP/FRET measurements, it is likely that we detected NO-dependent cGMP signalling that might not have been noticed by other approaches.

While early and late-stage HSCs can respond to NO in general, one must consider that in diseases like MASH, there is often a reduced availability of eNOS derived NO and a significant increase in iNOS derived NO. This iNOS derived NO supports oxidative burst and is the main

source of reactive nitrogen species [6]. Under such oxidative stress conditions, the NO-GC gets oxidized and the NO-signalling as well as the affinity of NO-GC to NO is disturbed, which contributes to disease progression. Thus, enhancing NO-GC activity independent of NO represents a potential treatment target for MASH. While NO-GC stimulators primarily sensitize NO-GC towards NO, NO-GC activators are thought to activate the NO-insensitive oxidized form of NO-GC [45]. In the present study, we investigated the effect of a novel NO-GC activator tool compound from Bayer on MASH progression as well as on HSCs *in vitro*.

Using real-time cGMP/FRET imaging, we tested the ability of the activator to induce cGMP generation in HSCs without prior oxidation of NO-GC. Interestingly, we observed similar cGMP responses to increasing concentrations of the activator in both day 2 **(Figure 21B, black curve, peaks 2-5)** and day 8 HSCs **(Figure 21F, black curve, peaks 2-5)**. These responses were concentration dependent, with notably robust signals detected at 50 nM and 100 nM. Although we did not see an increase in the maximum cGMP levels after 50 nM **(Figure 21C)**, the total cGMP was increased **(Figure 21D)** which might be a sign of sensor saturation. The activators are known to work under oxidative stress conditions, binding specifically to the heme-free oxidized form of NO-GC [26]. Part of the observed cGMP responses might be explained by the presence of oxidative stress under cell culture conditions, leading to the oxidation of NO-GC in HSCs. *In vivo* during MASLD development, HSC activation is one of the consequences of oxidative stress [187]. In our *in vitro* model, HSCs got activated by culturing them for a longer duration on plastic dishes. While it is still unclear how this leads to activation of HSCs, it is tempting to speculate that oxidative stress under cell culture conditions might be involved. It is said that *in vitro* cell culture under ambient atmospheric O_2 levels can contribute to oxidative stress in both primary and immortalized cells. Also, the pro-oxidant nature of the cell culture medium and the reduced availability of antioxidants can lead to a net increase in ROS [188].

In this way, the NO-GC in HSCs could have been oxidized causing the activator to elicit a cGMP response. But it is also possible that the activator is capable of acting on physiological NO-GC in its reduced heme state. In support of this, Stasch et al. conducted a study on the effects of an activator compound BAY 58-2667 on NO-GC activity, both alone and in the presence of ODQ [189], a substance that is said to oxidize NO-GC and lower its sensitivity to NO [190]. Their findings indicate that the activator alone exhibited concentration-dependent NO-GC

activation, which was further enhanced upon treatment with ODQ. Indeed, we observed that HSCs on day 2 and day 8 showed robust cGMP responses to the activator after ODQ application (data not shown). Another interesting aspect of our activator measurements was that the final NO application after activator treatment resulted in a weaker cGMP signal than the NO application before the activator treatment. This could be explained by the long duration of the measurements, possibly stressing the cells, and thereby impairing their NO-induced cGMP responses.

The findings presented here demonstrated that NO as well as the activator can induce cGMP responses in both early (day 2) and late-stage (day 8) HSCs in culture. To gain a more comprehensive understanding of how the activator can act on seemingly non-oxidized and oxidized NO-GC, further experiments are necessary. The findings presented here are based on a single measurement each from day 2 and day 8. Nonetheless, it can be concluded that whether under physiological conditions or otherwise, NO generated by endothelial cells regulates NO/cGMP/cGKI pathway through NO-GC in HSCs. In pathological conditions where NO might fail to do so, the activator should still be able to maintain cGMP levels by acting on oxidised NO-GC in aHSCs.

4.4 Pharmacological modulation of NO/cGMP pathway in MASH mice

Our data so far provides novel insights into the role of NO/cGMP/cGKI pathway in liver health and disease. In conjunction with these findings, we explored the therapeutic potential of a NO-GC modulating drug in MASH progression. In the context of MASLD spectrum, majority of the preclinical studies have focused on the therapeutic potential of NO-GC stimulators and PDE inhibitors. However, studies involving the role of NO-GC activators are sparse. Here, we investigated the hepatoprotective actions of a novel NO-GC activator on MASH progression in both male and female mice. The effect was analysed in ApoE KO mice fed a HFD mixed with the activator for 18-weeks (HFD+Act mice) and compared to ApoE KO mice on HFD alone (HFD mice). As far as we know, ours is the first study assessing the pharmacological modulation of NO-GC in an ApoE KO with HFD model of MASH which simultaneously develops atherosclerosis.

Our findings suggest that the activator has the potential to impact all four aspects of MASH pathophysiology: steatosis, hepatocyte damage, inflammation, and fibrosis. Elaborating on

the first aspect, treatment with activator improved the ballooning phenotype of hepatocytes and exhibited an anti-steatotic effect by reducing the accumulation of lipid vacuoles in the liver **(Figure 22A-C)**. As described in section 4.1.2, ApoE KO mice on HFD demonstrate an impaired lipid metabolism, leading to oxidative stress and eventual cellular dysfunction and cell death. The mechanism by which the activator reduces ballooning and lipid accumulation remains unclear. Our findings suggest that the activator is unlikely to directly act upon the hepatocytes since they did not express NO-GC and cGKI. However, this positive effect of the activator may be mediated extrahepatically. Several extrahepatic factors, mainly those derived from white adipose tissue (WAT) and brown adipose tissue (BAT) also influence the development of steatosis during fatty liver disease. These tissues also regulate both metabolism and energy expenditure [191].

Using the NO-GC stimulator IW-1973, Flores Costa et al. demonstrated an amelioration of hepatic steatosis in mice fed a CDHFD [13]. They showed that the treatment with IW-1973 reduced the size of adipocytes in WAT via increased autophagy mediated lipolysis, thus influencing the systemic metabolism, and improving the steatosis phenotype. In a diet-induced obesity model, Hoffmann et al. showed that BAY 41-8543, a NO-GC stimulator, enhanced lipid uptake in BAT and increased whole-body energy expenditure, leading to an improvement in the steatosis phenotype [192]. Considering these findings, it is plausible that, similar to the stimulator, the activator also affects lipid metabolism through adipose tissue. In line with this, male activator treated mice exhibited a trend towards decreased hepatic triglyceride content (data not shown). However, this effect was not observed in females, rendering this assumption unlikely. Therefore, further investigation is required to elucidate the role of activator in regulating lipid metabolism, both within and outside the liver.

Next, we assessed the effect of activator treatment on liver function by checking the serum levels of AST and ALT. AST and ALT are enzymes normally found in the liver and play a crucial role in various biochemical processes. Upon liver injury, the cell membrane of the liver cells particularly of hepatocytes can be compromised in addition to cell death. As a result, AST and ALT which are normally contained within the cells can be released into the bloodstream [193]. The activator-treated male mice displayed significantly lower levels of ALT, with AST showing a tendency towards reduction **(Figure 22D-E)**. A similar trend was observed in female AST and ALT levels **(Figure 22F-G)**. This could be because the AST and ALT values in female HFD animals

were generally lower compared to those in males. Hence, although the activator treatment indicated a tendency towards reduction, it is possible that this change is not significant due to the lower enzyme levels in females. Another reason could be due to a high variation of samples within each group. Additional serum analysis with a greater number of animals is planned to obtain clear results. Nevertheless, our findings on increased liver enzyme levels within the HFD group align with previous studies which used these two parameters to assess liver health and function [84, 92, 113]. The trend observed in HFD+Act group suggests that the treatment with the activator seemed to have improve the liver function, which is also clearly evident by reduced hepatocellular ballooning.

Inflammation in MASH is a consequence of lipotoxicity and is characterized infiltration and activation of Kupffer cells (KCs) and several pro-inflammatory cytokines. Studies in preclinical models of MASH have shown that chronic inflammation follows steatosis and hepatocyte injury observed by increased infiltration of F4/80 positive macrophages and levels of pro-inflammatory markers [84, 113, 117]. Similarly, our HFD mice showed enhanced Mac-2 and F4/80 staining followed by an increase in the transcript levels of several proinflammatory markers **(Figure 23A-E, labelled as HFD)**. In addition to the classical macrophage marker F4/80, Mac-2 (galectin-3) is also known to be constitutively expressed on macrophages. An upregulation in the expression of galectin-3 was temporally and spatially associated with the induction of liver fibrosis and its disruption blocked HSC activation and procollagen-I expression [90]. Further confirmation of increased galectin-3 expression has been observed in other preclinical models of liver fibrosis [91] and MASH [194]. In line with these findings, the activation of HSCs and the subsequent development of fibrosis in our HFD model suggests a possible involvement of inflammation and Mac2 upregulation.

Interestingly, treatment with the activator caused a significant decrease in the Mac-2 positive area **(Figure 23A-B, labelled as HFD+Act)**. The expression levels of F4/80 and most proinflammatory markers exhibited a tendency towards reduction, with the exception of CCL2 **(Figure 23C-E)**. CCL2 is one of the many chemokines involved in the recruitment of certain immune cells, particularly monocytes to the sites of inflammation and injury. The expression of CCL2 is regulated by the transcription factor NF-κB. These CCL2 recruited monocytes differentiate into infiltrating macrophages with proinflammatory and fibrogenic properties

[195]. This could explain the increase in inflammation and fibrosis in the livers of HFD animals. Indeed, pharmacological inhibition of monocyte infiltration using a CCL2-inhibitor has been shown to alleviate steatohepatitis and liver fibrosis [196, 197]. It is possible that the treatment with activator in our model might have potentially inhibited NF-κB activity, subsequently leading to a decrease in the expression of CCL2.

The pharmacological effects of cGMP on MASH inflammation has so far only been described using NO-GC stimulators. Using the CDHFD model of MASH, Flores-Costa et al. have nicely demonstrated the anti-inflammatory actions associated with the stimulation of NO-GC using praliciguat [109]. Praliciguat mediated its anti-inflammatory effects via down regulation of IL-1β and NLRP3 expression in KC which resulted in NF-κB inhibition. This inhibition was associated with increased VASP Ser239 phosphorylation, a well-established downstream target of cGKI. Using a similar mouse model, the same authors have also demonstrated the anti-inflammatory effects of NO-GC stimulator IW-1973 mediated via an amelioration WAT inflammation [13]. Hall et al. have also reported a reduction in local and systemic inflammation upon praliciguat treatment associated with a decrease in the protein levels of NF-κB in CCl_4 induced liver fibrosis [14]. All of these findings shed light on the fact that there are several possibilities through which cGMP enhancing drugs can act and attenuate liver inflammation. However, the lack of studies on the role of NO-GC activator in attenuating liver inflammation and the absence of NO-GC expression in liver resident macrophages renders it challenging to explain the effect observed in our model. In this case, one can only speculate that the activator does not act directly via NO-GC but on one of the many inflammatory signalling pathways within the liver.

Last but not least, treatment with the activator significantly diminished HSC activation and liver fibrosis. Our data shows that in comparison to the non-treated HFD group, activator treated mice showed a significant reduction in α-SMA positive area and the appearance of aHSCs within the liver parenchyma **(Figure 24A-C)**. This was further validated by reduced mRNA levels of ACTA2 in HFD+Act group **(Figure 24D)**. This suggests that the treatment with activator prevented HSC activation by acting on the NO-GC that is still expressed in aHSCs of MASH liver. As mentioned earlier, in diseases like MASH, cGMP production is downregulated due to reduced activity of eNOS derived NO and oxidation the of NO-GC which renders the

enzyme unresponsive to NO. Therefore, it is likely that in our MASH model there is a deficiency of NO and the NO-GC expressed by HSCs is oxidized due to oxidative stress. This explanation aligns well with the described mode of action for NO-GC activators [26]. The activation of NO-GC followed by an increase in intracellular cGMP has been shown to reduce HSC activation [180]. However, tracing back to our cell culture data it is also possible that the activator could have acted upon the non-oxidized form of NO-GC in HSCs while they are still quiescent before the onset of MASH, thereby preventing them from being activated during the course of disease progression.

Consistent with our observation of less aHSCs, male mice treated with the activator exhibited a significant decrease in periportal fibrosis compared to the HFD group **(Figure 24E-G)**. The female activator treated mice however, displayed a tendency towards reduction in periportal fibrosis **(Figure 24H)**. This could be attributed to milder fibrosis development in the female HFD mice in comparison to the males **(Figure 15D, blue and pink columns)**. Additionally, the reduction in hepatic fibrosis was reflected in a diminished collagen IV accumulation in the livers of activator treated mice **(Figure 24I-J)**. A similar antifibrotic effect of a NO-GC activator was demonstrated by Knorr et al. [108]. In two rat models of liver fibrosis induced by pig serum and CCl_4, treatment with the NO-GC activator BAY 60-2770 attenuated fibrosis as seen by a reduction in PSR-positive area and in hepatic collagen levels. Recently, the antifibrotic effect of another NO-GC activator BI 685509 was analysed both chronically and acutely in a rat model of thioacetamide (TAA) induced liver cirrhosis [111]. In this study, the administration of BI 685509 showed a dose-dependent increase in hepatic cGMP levels. Additionally, they observed a reduction in Sirius Red morphometry and α-SMA positive area together with a drop in the portal venous pressure and portosystemic shunting [111]. This suggests that in liver cirrhosis and portal hypertension, therapeutically restoring hepatic cGMP levels by modulating NO-GC holds promise, as it addresses both vasoactive and antifibrotic mechanisms.

Taken together, the findings reported by us and others share one thing in common, i.e. elevation of hepatic cGMP levels either by using NO-GC activators or stimulators improves the phenotype of MASH in several preclinical mouse models. We are confident that with the

increasing amount of such preclinical evidence, very soon cGMP enhancing drugs targeted towards treating chronic liver diseases like MASLD and MASH will enter clinical trials.

5 Conclusion and outlook

In summary, we successfully established and characterized a mouse model which recapitulated the pathogenesis of human MASH including steatosis, ballooning, inflammation, and hepatic fibrosis together with its comorbidity atherosclerosis. By exploiting this model, we discovered a pivotal role of the NO/cGMP signalling pathway in healthy and MASH livers. Combination of our *in vivo* model with real-time cGMP/FRET imaging in cultured HSCs demonstrated that NO-GC-dependent cGMP signalling in early (day 2) and late-stage (day 8) HSCs is functionally active and is susceptible to pharmacological manipulation by a recently developed NO-GC activator.

Our histological analysis verified MASH development in male and female mice with some of its features being slightly less severe in females (hepatocyte ballooning and fibrosis). Furthermore, the development of MASH was associated with the activation and massive expansion of HSCs in our *in vivo* model. These aHSCs adopted a myofibroblast-like phenotype, marked by enhanced expression of activated HSC markers like SM22 and α-SMA. Interestingly, qHSCs (healthy livers) retained robust expression of the key components of the cGMP signalling pathway (NO-GC, cGKI) even upon activation into aHSCs, observed in advanced stages of MASH-afflicted livers. *In vitro*, our cell culture model with primary murine HSCs faithfully mimicked our *in vivo* findings with regard to phenotypical changes during activation and the expression of cGMP pathway components (NO-GC, cGKI). Using this cell culture model, we could verify that both early and late-stage HSCs in culture generated cGMP not only in response to NO (targeting ''physiological NO-GC'') but to a novel NO-GC activator (targeting ''pathologically inactivated NO-GC''). Based on these results, we tested the therapeutic potential of the aforementioned NO-GC activator as a novel treatment for MASH. Interestingly, we observed an improvement of MASH phenotype (reduced hepatocyte ballooning, HSC activation, fibrosis and a trend towards reduced inflammation and liver enzymes) in mice treated with the NO-GC activator compared to the non-treated HFD group.

Despite these interesting insights on the functional relevance of the cGMP signalling pathway in liver health and disease, much work remains to be done. For instance, it is still unclear how

cGMP signalling protects against MASH. (1) To verify that NO-dependent cGMP signalling in HSCs is responsible for the protective effects, one could generate atherosclerotic, HSC-specific NO-GC knockout mice (e.g., via Cre lox mediated recombination in HSCs by crossing the Lrat-Cre to a floxed NO-GC or cGKI mouse line). These mice should be treated with the NO-GC activator and MASH development should be analysed. (2) HSCs in culture should be treated with cGMP modulating drugs (e.g, NO releasing compounds, NO-GC activator) over several days to test whether this affects activation and/or proliferation of HSCs. (3) As the cell culture model insufficiently mimics oxidative stress, it would be interesting to investigate whether HSCs isolated from MASH livers are still responsive to NO in culture. (4) As NO-GC activators, in contrast to NO-GC stimulators, can target the inactive/oxidized form of NO-GC, one should investigate the potential of NO-GC activators in reversing late-stages of MASH. (5) An important finding of our activator study was the difference in the treatment outcome in two disease conditions analysed within the same mice. While the activator displayed hepatoprotective effects against MASH, it exhibited athero-promoting effects in atherosclerosis **(PhD thesis- Malte Roeßing)**. Hence, it is crucial to investigate the potential of co-administering the NO-GC activator along with athero-protective medications in our MASH mice, aiming to reduce the severe impact on the co-existing condition of atherosclerosis.

In conclusion, we hypothesize that NO-GC and cGKI retained by the aHSCs could play a preventive role in MASH progression. This may occur either by shifting the aHSCs back to a quiescent state or by limiting their expansion during disease progression. This hypothesis also supports our assumption that the activator mediates its MASH-protective effects via NO-GC in HSCs, potentially elevating the hepatic cGMP levels under conditions of impaired cGMP signalling due to oxidative stress and reduced NO availability. Consequently, NO-GC activators hold promise as potent hepatoprotective agents targeting MASH at its core **(Figure 25)**.

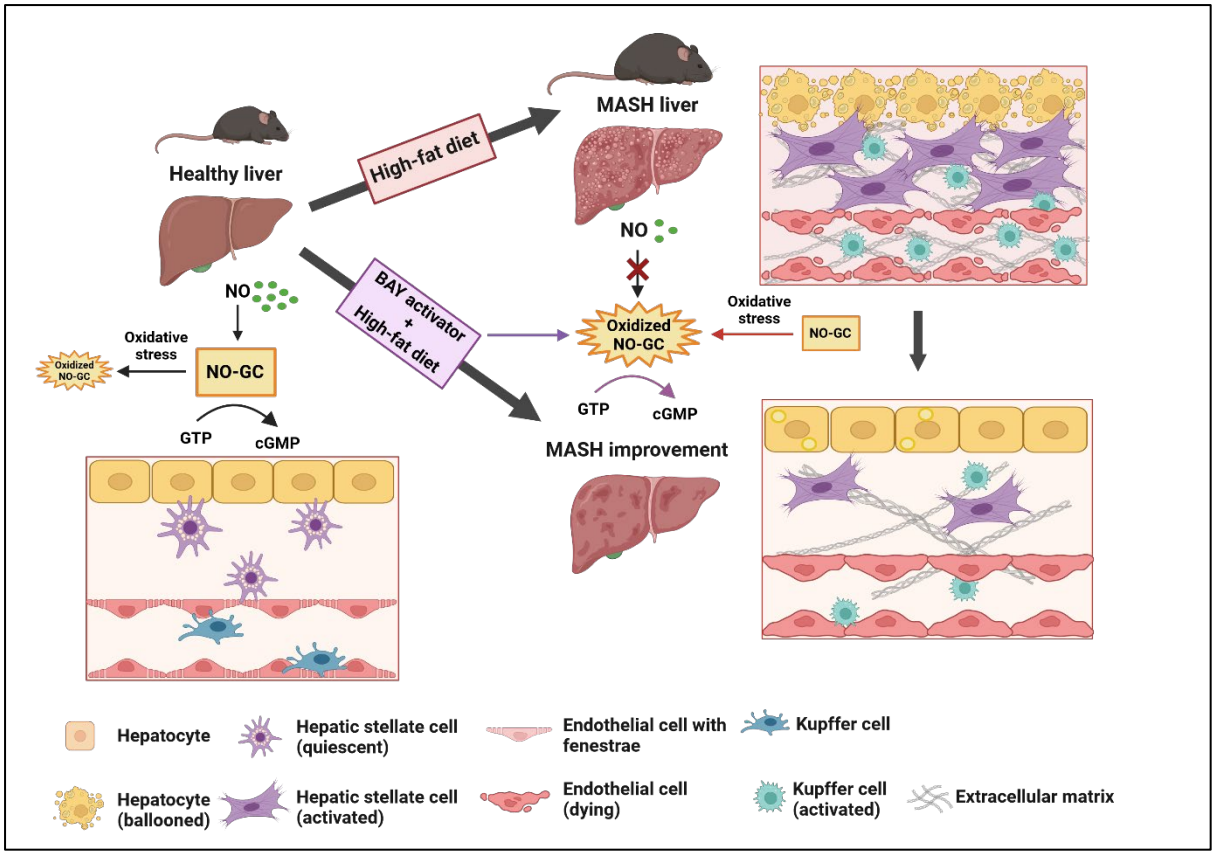

Figure 25: Summary of cGMP signalling in healthy and in MASH livers. In a healthy liver, quiescent HSCs within the space of Disse express NO-GC in its native form, which is activated by NO, resulting in cGMP generation. Under physiological conditions, a small amount of this native NO-GC may also undergo oxidation. Feeding mice with HFD leads to the development of MASH, characterized by hepatocellular ballooning, proliferation, and activation of HSCs and Kupffer cells. These events lead to steatosis, fibrosis, and inflammation. Within the MASH liver, NO-GC that is retained by activated HSCs is thought to exist in its oxidized form owing to increased oxidative stress. This oxidized NO-GC can no longer respond to NO, which potentially impairs cGMP signalling. BAY activator can act on oxidized form of NO-GC, resulting in cGMP production. In our model, the treatment with BAY activator improved MASH features by limiting the expansion of activated HSCs and KCs as well as lipid accumulation. This led to a reduction in fibrosis, hepatocellular ballooning, inflammation, and liver enzyme levels. This mode of action likely enhances the hepatic cGMP levels, potentially impacting the overall liver health. The figure is created using Biorender.com.

6 References

1. Hofmann, F., The cGMP system: components and function. Biol Chem, 2020. 401(4): p. 447-469.
2. Lincoln, T.M., N. Dey, and H. Sellak, Invited review: cGMP-dependent protein kinase signaling mechanisms in smooth muscle: from the regulation of tone to gene expression. J Appl Physiol (1985), 2001. 91(3): p. 1421-30.
3. Wolfsgruber, W., et al., A proatherogenic role for cGMP-dependent protein kinase in vascular smooth muscle cells. Proc Natl Acad Sci U S A, 2003. 100(23): p. 13519-24.
4. Dhayade, S., et al., Sildenafil potentiates a cGMP-dependent pathway to promote melanoma growth. Cell Rep, 2016. 14(11): p. 2599-610.
5. Kreisel, W., et al., Cyclic GMP in liver cirrhosis-role in pathophysiology of portal hypertension and therapeutic implications. Int J Mol Sci, 2021. 22(19).
6. Iwakiri, Y. and M.Y. Kim, Nitric oxide in liver diseases. Trends Pharmacol Sci, 2015. 36(8): p. 524-36.
7. Ksenia Brusilovskaya, P.K., Philipp Schwabl, Thomas Reiberger, Vascular targets for the treatment of portal hypertension. Seminars in Liver Disease, 2019: p. 483-501.
8. Feil, R. and B. Kemp-Harper, cGMP signalling: from bench to bedside. Conference on cGMP generators, effectors and therapeutic implications. EMBO Rep, 2006. 7(2): p. 149-53.
9. Schlossmann, J. and E. Schinner, cGMP becomes a drug target. Naunyn Schmiedebergs Arch Pharmacol, 2012. 385(3): p. 243-52.
10. Watanabe, H., Treatment selection in pulmonary arterial hypertension: phosphodiesterase type 5 inhibitors versus soluble guanylate cyclase stimulator. Eur Cardiol, 2018. 13(1): p. 35-37.
11. Sandner, P. and J.P. Stasch, Anti-fibrotic effects of soluble guanylate cyclase stimulators and activators: A review of the preclinical evidence. Respir Med, 2017. 122 Suppl 1: p. S1-S9.
12. Hohenstein, B., et al., Stimulation of soluble guanylyl cyclase inhibits mesangial cell proliferation and matrix accumulation in experimental glomerulonephritis. Am J Physiol Renal Physiol, 2005. 288(4): p. F685-93.
13. Flores-Costa, R., et al., The soluble guanylate cyclase stimulator IW-1973 prevents inflammation and fibrosis in experimental non-alcoholic steatohepatitis. Br J Pharmacol, 2018. 175(6): p. 953-967.
14. Hall, K.C., et al., sGC stimulator praliciguat suppresses stellate cell fibrotic transformation and inhibits fibrosis and inflammation in models of NASH. Proc Natl Acad Sci U S A, 2019. 116(22): p. 11057-11062.
15. Brusilovskaya, K., et al., Soluble guanylyl cyclase stimulation and phosphodiesterase-5 inhibition improve portal hypertension and reduce liver fibrosis in bile duct-ligated rats. United European Gastroenterol J, 2020. 8(10): p. 1174-1185.
16. Mintz, J., et al., Current advances of nitric oxide in cancer and anticancer therapeutics. Vaccines (Basel), 2021. 9(2).
17. Potter, L.R., Guanylyl cyclase structure, function and regulation. Cell Signal, 2011. 23(12): p. 1921-6.
18. Derbyshire, E.R. and M.A. Marletta, Structure and regulation of soluble guanylate cyclase. Annu Rev Biochem, 2012. 81: p. 533-59.
19. Russwurm, M., et al., Functional properties of a naturally occurring isoform of soluble guanylyl cyclase. Biochem J, 1998. 335 (Pt 1)(Pt 1): p. 125-30.

20. Friebe, A. and D. Koesling, The function of NO-sensitive guanylyl cyclase: what we can learn from genetic mouse models. Nitric Oxide, 2009. 21(3-4): p. 149-56.
21. Horst, B.G., et al., Allosteric activation of the nitric oxide receptor soluble guanylate cyclase mapped by cryo-electron microscopy. Elife, 2019. 8.
22. Zhao, Y., et al., Identification of histidine 105 in the beta1 subunit of soluble guanylate cyclase as the heme proximal ligand. Biochemistry, 1998. 37(13): p. 4502-9.
23. Kang, Y., et al., Structural insights into the mechanism of human soluble guanylate cyclase. Nature, 2019. 574(7777): p. 206-210.
24. Krishnan, S.M., et al., The impact of the nitric oxide (NO)/soluble guanylyl cyclase (sGC) signaling cascade on kidney health and disease: a preclinical perspective. Int J Mol Sci, 2018. 19(6).
25. Kemp-Harper, B. and R. Feil, Meeting report: cGMP matters. Sci Signal, 2008. 1(9): p. pe12.
26. Sandner, P., et al., Soluble guanylate cyclase stimulators and activators. Handb Exp Pharmacol, 2021. 264: p. 355-394.
27. Forstermann, U. and W.C. Sessa, Nitric oxide synthases: regulation and function. Eur Heart J, 2012. 33(7): p. 829-37, 837a-837d.
28. Forstermann, U. and H. Kleinert, Nitric oxide synthase: expression and expressional control of the three isoforms. Naunyn Schmiedebergs Arch Pharmacol, 1995. 352(4): p. 351-64.
29. Potter, L.R., et al., Natriuretic peptides: their structures, receptors, physiologic functions and therapeutic applications. Handb Exp Pharmacol, 2009(191): p. 341-66.
30. Kuhn, M., Structure, regulation, and function of mammalian membrane guanylyl cyclase receptors, with a focus on guanylyl cyclase-A. Circ Res, 2003. 93(8): p. 700-9.
31. Fesenko, E.E., S.S. Kolesnikov, and A.L. Lyubarsky, Induction by cyclic GMP of cationic conductance in plasma membrane of retinal rod outer segment. Nature, 1985. 313(6000): p. 310-3.
32. Kaupp, U.B. and R. Seifert, Cyclic nucleotide-gated ion channels. Physiol Rev, 2002. 82(3): p. 769-824.
33. Matulef, K. and W.N. Zagotta, Cyclic nucleotide-gated ion channels. Annu Rev Cell Dev Biol, 2003. 19: p. 23-44.
34. Kramer, R.H. and E. Molokanova, Modulation of cyclic-nucleotide-gated channels and regulation of vertebrate phototransduction. J Exp Biol, 2001. 204(Pt 17): p. 2921-31.
35. Biel, M. and S. Michalakis, Cyclic nucleotide-gated channels. Handb Exp Pharmacol, 2009(191): p. 111-36.
36. Pfeifer, A., et al., Structure and function of cGMP-dependent protein kinases. Rev Physiol Biochem Pharmacol, 1999. 135: p. 105-49.
37. Hofmann, F., et al., Function of cGMP-dependent protein kinases as revealed by gene deletion. Physiol Rev, 2006. 86(1): p. 1-23.
38. Bender, A.T. and J.A. Beavo, Cyclic nucleotide phosphodiesterases: molecular regulation to clinical use. Pharmacol Rev, 2006. 58(3): p. 488-520.
39. Gomez, L. and J.G. Breitenbucher, PDE2 inhibition: potential for the treatment of cognitive disorders. Bioorg Med Chem Lett, 2013. 23(24): p. 6522-7.
40. Cartledge, J. and I. Eardley, Sildenafil. Expert Opin Pharmacother, 1999. 1(1): p. 137-47.

41. Ala, M., R. Mohammad Jafari, and A.R. Dehpour, Sildenafil beyond erectile dysfunction and pulmonary arterial hypertension: Thinking about new indications. Fundam Clin Pharmacol, 2021. 35(2): p. 235-259.
42. Singh, J.S.S., et al., Sacubitril/valsartan: beyond natriuretic peptides. Heart, 2017. 103(20): p. 1569-1577.
43. McMurray, J.J., et al., Angiotensin-neprilysin inhibition versus enalapril in heart failure. N Engl J Med, 2014. 371(11): p. 993-1004.
44. Docherty, K.F., et al., Sacubitril/Valsartan: Neprilysin inhibition 5 years after PARADIGM-HF. JACC Heart Fail, 2020. 8(10): p. 800-810.
45. Sandner, P., et al., Soluble GC stimulators and activators: past, present and future. Br J Pharmacol, 2021.
46. Stasch, J.P. and A.J. Hobbs, NO-independent, haem-dependent soluble guanylate cyclase stimulators. Handb Exp Pharmacol, 2009(191): p. 277-308.
47. Ko, F.N., et al., YC-1, a novel activator of platelet guanylate cyclase. Blood, 1994. 84(12): p. 4226-33.
48. Liu, R., Y. Kang, and L. Chen, Activation mechanism of human soluble guanylate cyclase by stimulators and activators. Nat Commun, 2021. 12(1): p. 5492.
49. Evgenov, O.V., et al., NO-independent stimulators and activators of soluble guanylate cyclase: discovery and therapeutic potential. Nat Rev Drug Discov, 2006. 5(9): p. 755-68.
50. Feil, R., et al., Visualising and understanding cGMP signals in the cardiovascular system. Br J Pharmacol, 2022. 179(11): p. 2394-2412.
51. Sekar, R.B. and A. Periasamy, Fluorescence resonance energy transfer (FRET) microscopy imaging of live cell protein localizations. J Cell Biol, 2003. 160(5): p. 629-33.
52. Thunemann, M., et al., Transgenic mice for cGMP imaging. Circ Res, 2013. 113(4): p. 365-71.
53. Russwurm, M., et al., Design of fluorescence resonance energy transfer (FRET)-based cGMP indicators: a systematic approach. Biochem J, 2007. 407(1): p. 69-77.
54. Juza, R.M. and E.M. Pauli, Clinical and surgical anatomy of the liver: a review for clinicians. Clin Anat, 2014. 27(5): p. 764-9.
55. Trefts, E., M. Gannon, and D.H. Wasserman, The liver. Curr Biol, 2017. 27(21): p. R1147-R1151.
56. Schulze, R.J., et al., The cell biology of the hepatocyte: A membrane trafficking machine. J Cell Biol, 2019. 218(7): p. 2096-2112.
57. Kmiec, Z., Cooperation of liver cells in health and disease. Adv Anat Embryol Cell Biol, 2001. 161: p. III-XIII, 1-151.
58. Banales, J.M., et al., Cholangiocyte pathobiology. Nat Rev Gastroenterol Hepatol, 2019. 16(5): p. 269-281.
59. Ramachandran, P., et al., Single-cell technologies in hepatology: new insights into liver biology and disease pathogenesis. Nat Rev Gastroenterol Hepatol, 2020. 17(8): p. 457-472.
60. Poisson, J., et al., Liver sinusoidal endothelial cells: physiology and role in liver diseases. J Hepatol, 2017. 66(1): p. 212-227.
61. Dixon, L.J., et al., Kupffer cells in the liver. Compr Physiol, 2013. 3(2): p. 785-97.
62. Hellerbrand, C., Hepatic stellate cells--the pericytes in the liver. Pflugers Arch, 2013. 465(6): p. 775-8.

63. Senoo, H., Structure and function of hepatic stellate cells. Med Electron Microsc, 2004. 37(1): p. 3-15.
64. Blomhoff, R. and H.K. Blomhoff, Overview of retinoid metabolism and function. J Neurobiol, 2006. 66(7): p. 606-30.
65. Mederacke, I., et al., High-yield and high-purity isolation of hepatic stellate cells from normal and fibrotic mouse livers. Nat Protoc, 2015. 10(2): p. 305-15.
66. Tacke, F. and R. Weiskirchen, Update on hepatic stellate cells: pathogenic role in liver fibrosis and novel isolation techniques. Expert Rev Gastroenterol Hepatol, 2012. 6(1): p. 67-80.
67. Bataller, R. and D.A. Brenner, Liver fibrosis. J Clin Invest, 2005. 115(2): p. 209-18.
68. Tsuchida, T. and S.L. Friedman, Mechanisms of hepatic stellate cell activation. Nat Rev Gastroenterol Hepatol, 2017. 14(7): p. 397-411.
69. Mederacke, I., et al., Fate tracing reveals hepatic stellate cells as dominant contributors to liver fibrosis independent of its aetiology. Nat Commun, 2013. 4: p. 2823.
70. Li, D., et al., Targeting activated hepatic stellate cells (aHSCs) for liver fibrosis imaging. EJNMMI Res, 2015. 5(1): p. 71.
71. Tateya, S., et al., Endothelial NO/cGMP/VASP signaling attenuates Kupffer cell activation and hepatic insulin resistance induced by high-fat feeding. Diabetes, 2011. 60(11): p. 2792-801.
72. Yang, W., et al., Single-cell transcriptomic analysis reveals a hepatic stellate cell-activation roadmap and myofibroblast origin during liver fibrosis in mice. Hepatology, 2021. 74(5): p. 2774-2790.
73. Lutz, S.Z., et al., Genetic ablation of cGMP-dependent protein kinase type I causes liver inflammation and fasting hyperglycemia. Diabetes, 2011. 60(5): p. 1566-76.
74. Franko, A., et al., cGMP-dependent protein kinase I (cGKI) modulates human hepatic stellate cell activation. Metabolism, 2018. 88: p. 22-30.
75. Younossi, Z.M., et al., The global epidemiology of nonalcoholic fatty liver disease (NAFLD) and nonalcoholic steatohepatitis (NASH): a systematic review. Hepatology, 2023. 77(4): p. 1335-1347.
76. Riazi, K., et al., The prevalence and incidence of NAFLD worldwide: a systematic review and meta-analysis. Lancet Gastroenterol Hepatol, 2022. 7(9): p. 851-861.
77. Manikat, R. and M.H. Nguyen, Nonalcoholic fatty liver disease and non-liver comorbidities. Clin Mol Hepatol, 2023. 29(Suppl): p. s86-s102.
78. Rinella, M.E., et al., A multisociety Delphi consensus statement on new fatty liver disease nomenclature. Hepatology, 2023. 78(6): p. 1966-1986.
79. Multinational liver societies announce new ''Fatty'' liver disease nomenclature that is affirmative and non-stigmatising. 2023.
80. Anstee, Q.M., et al., From NASH to HCC: current concepts and future challenges. Nat Rev Gastroenterol Hepatol, 2019. 16(7): p. 411-428.
81. Day, C.P. and O.F. James, Steatohepatitis: a tale of two "hits"? Gastroenterology, 1998. 114(4): p. 842-5.
82. Buzzetti, E., M. Pinzani, and E.A. Tsochatzis, The multiple-hit pathogenesis of non-alcoholic fatty liver disease (NAFLD). Metabolism, 2016. 65(8): p. 1038-48.
83. Noureddin, M. and A.J. Sanyal, Pathogenesis of NASH: The Impact of Multiple Pathways. Curr Hepatol Rep, 2018. 17(4): p. 350-360.

84. Schierwagen, R., et al., Seven weeks of western diet in apolipoprotein-E-deficient mice induce metabolic syndrome and non-alcoholic steatohepatitis with liver fibrosis. Sci Rep, 2015. 5: p. 12931.
85. Tsuchida, T., et al., A simple diet- and chemical-induced murine NASH model with rapid progression of steatohepatitis, fibrosis and liver cancer. J Hepatol, 2018. 69(2): p. 385-395.
86. Alves-Bezerra, M. and D.E. Cohen, Triglyceride metabolism in the liver. Compr Physiol, 2017. 8(1): p. 1-8.
87. Nassir, F., et al., Pathogenesis and prevention of hepatic steatosis. Gastroenterol Hepatol (N Y), 2015. 11(3): p. 167-75.
88. Kim, K.H. and M.S. Lee, Pathogenesis of nonalcoholic steatohepatitis and hormone-based therapeutic approaches. Front Endocrinol (Lausanne), 2018. 9: p. 485.
89. Liu, C., et al., Kupffer cells are associated with apoptosis, inflammation and fibrotic effects in hepatic fibrosis in rats. Lab Invest, 2010. 90(12): p. 1805-16.
90. Henderson, N.C., et al., Galectin-3 regulates myofibroblast activation and hepatic fibrosis. Proc Natl Acad Sci U S A, 2006. 103(13): p. 5060-5.
91. Jeftic, I., et al., Galectin-3 ablation enhances liver steatosis, but attenuates inflammation and IL-33-dependent fibrosis in obesogenic mouse model of nonalcoholic steatohepatitis. Mol Med, 2015. 21(1): p. 453-65.
92. Hoffmann, C., et al., Hepatic stellate cell hypertrophy is associated with metabolic liver fibrosis. Sci Rep, 2020. 10(1): p. 3850.
93. Heyens, L.J.M., et al., Liver fibrosis in non-alcoholic fatty liver disease: from liver biopsy to non-invasive biomarkers in diagnosis and treatment. Front Med (Lausanne), 2021. 8: p. 615978.
94. Llovet, J.M., et al., Hepatocellular carcinoma. Nat Rev Dis Primers, 2021. 7(1): p. 6.
95. Chalasani, N., et al., The diagnosis and management of nonalcoholic fatty liver disease: Practice guidance from the American Association for the Study of Liver Diseases. Hepatology, 2018. 67(1): p. 328-357.
96. European Association for the Study of the, L., D. European Association for the Study of, and O. European Association for the Study of, EASL-EASD-EASO clinical practice guidelines for the management of non-alcoholic fatty liver disease. J Hepatol, 2016. 64(6): p. 1388-402.
97. Ryan, M.C., et al., The Mediterranean diet improves hepatic steatosis and insulin sensitivity in individuals with non-alcoholic fatty liver disease. J Hepatol, 2013. 59(1): p. 138-43.
98. Yaskolka Meir, A., et al., Effect of green-Mediterranean diet on intrahepatic fat: the DIRECT PLUS randomised controlled trial. Gut, 2021. 70(11): p. 2085-2095.
99. Hassani Zadeh, S., A. Mansoori, and M. Hosseinzadeh, Relationship between dietary patterns and non-alcoholic fatty liver disease: A systematic review and meta-analysis. J Gastroenterol Hepatol, 2021. 36(6): p. 1470-1478.
100. Armstrong, M.J., et al., Liraglutide safety and efficacy in patients with non-alcoholic steatohepatitis (LEAN): a multicentre, double-blind, randomised, placebo-controlled phase 2 study. Lancet, 2016. 387(10019): p. 679-690.
101. Harrison, S.A., et al., Semaglutide for the treatment of non-alcoholic steatohepatitis: Trial design and comparison of non-invasive biomarkers. Contemp Clin Trials, 2020. 97: p. 106174.

102. Newsome, P.N., et al., A placebo-controlled trial of subcutaneous semaglutide in nonalcoholic steatohepatitis. N Engl J Med, 2021. 384(12): p. 1113-1124.
103. Neuschwander-Tetri, B.A., et al., Farnesoid X nuclear receptor ligand obeticholic acid for non-cirrhotic, non-alcoholic steatohepatitis (FLINT): a multicentre, randomised, placebo-controlled trial. Lancet, 2015. 385(9972): p. 956-65.
104. Friedman, S.L., et al., A randomized, placebo-controlled trial of cenicriviroc for treatment of nonalcoholic steatohepatitis with fibrosis. Hepatology, 2018. 67(5): p. 1754-1767.
105. Chalasani, N., et al., Effects of Belapectin, an inhibitor of Galectin-3, in patients with nonalcoholic steatohepatitis with cirrhosis and portal hypertension. Gastroenterology, 2020. 158(5): p. 1334-1345 e5.
106. Singh, G., M. Krauthamer, and M. Bjalme-Evans, Wegovy (semaglutide): a new weight loss drug for chronic weight management. J Investig Med, 2022. 70(1): p. 5-13.
107. Mantovani, A. and A. Dalbeni, Treatments for NAFLD: state of art. Int J Mol Sci, 2021. 22(5).
108. Knorr, A., et al., Nitric oxide-independent activation of soluble guanylate cyclase by BAY 60-2770 in experimental liver fibrosis. Arzneimittelforschung, 2008. 58(2): p. 71-80.
109. Flores-Costa, R., et al., Stimulation of soluble guanylate cyclase exerts antiinflammatory actions in the liver through a VASP/NF-kappaB/NLRP3 inflammasome circuit. Proc Natl Acad Sci U S A, 2020. 117(45): p. 28263-28274.
110. Schwabl, P., et al., The soluble guanylate cyclase stimulator riociguat reduces fibrogenesis and portal pressure in cirrhotic rats. Sci Rep, 2018. 8(1): p. 9372.
111. Jones, A.K., et al., Soluble guanylyl cyclase activator BI 685509 reduces portal hypertension and portosystemic shunting in a rat thioacetamide-induced cirrhosis model. J Pharmacol Exp Ther, 2023. 386(1): p. 70-79.
112. Gallage, S., et al., A researcher's guide to preclinical mouse NASH models. Nat Metab, 2022. 4(12): p. 1632-1649.
113. Camargo, F.N., et al., Western diet-fed ApoE knockout male mice as an experimental model of non-alcoholic steatohepatitis. Curr Issues Mol Biol, 2022. 44(10): p. 4692-4703.
114. Asgharpour, A., et al., A diet-induced animal model of non-alcoholic fatty liver disease and hepatocellular cancer. J Hepatol, 2016. 65(3): p. 579-88.
115. Ganguly, S., et al., Nonalcoholic steatohepatitis and HCC in a hyperphagic mouse accelerated by western diet. Cell Mol Gastroenterol Hepatol, 2021. 12(3): p. 891-920.
116. Clapper, J.R., et al., Diet-induced mouse model of fatty liver disease and nonalcoholic steatohepatitis reflecting clinical disease progression and methods of assessment. Am J Physiol Gastrointest Liver Physiol, 2013. 305(7): p. G483-95.
117. Wolf, M.J., et al., Metabolic activation of intrahepatic CD8+ T cells and NKT cells causes nonalcoholic steatohepatitis and liver cancer via cross-talk with hepatocytes. Cancer Cell, 2014. 26(4): p. 549-64.
118. Rizki, G., et al., Mice fed a lipogenic methionine-choline-deficient diet develop hypermetabolism coincident with hepatic suppression of SCD-1. J Lipid Res, 2006. 47(10): p. 2280-90.
119. Ibrahim, S.H., et al., Animal models of nonalcoholic steatohepatitis: eat, delete, and inflame. Dig Dis Sci, 2016. 61(5): p. 1325-36.

120. Farrell, G., et al., Mouse models of nonalcoholic steatohepatitis: toward optimization of their relevance to human nonalcoholic steatohepatitis. Hepatology, 2019. 69(5): p. 2241-2257.
121. Piedrahita, J.A., et al., Generation of mice carrying a mutant apolipoprotein E gene inactivated by gene targeting in embryonic stem cells. Proc Natl Acad Sci U S A, 1992. 89(10): p. 4471-5.
122. Sadeghipour, A. and P. Babaheidarian, Making formalin-fixed, paraffin embedded blocks. Methods Mol Biol, 2019. 1897: p. 253-268.
123. Mehlem, A., et al., Imaging of neutral lipids by oil red O for analyzing the metabolic status in health and disease. Nat Protoc, 2013. 8(6): p. 1149-54.
124. Koehler, A., Ein neues beleuchtungsverfahren für mikrophotographische zwecke. Zeitschrift für wissenschaftliche Mikroskopie und für Mikroskopische Technik, 1893. 10(4): p. 433-440.
125. Wilson, M. Koehler illumination: A brief history and a practical set up in five easy steps. 2017; Available from: https://www.leica-microsystems.com/science-lab/microscopy-basics/koehler-illumination-a-brief-history-and-a-practical-set-up-in-five-easy-steps/.
126. Junqueira, L.C., G. Bignolas, and R.R. Brentani, Picrosirius staining plus polarization microscopy, a specific method for collagen detection in tissue sections. Histochem J, 1979. 11(4): p. 447-55.
127. Segnani, C., et al., Histochemical detection of collagen fibers by Sirius Red/Fast Green is more sensitive than van Gieson or Sirius Red alone in normal and inflamed rat colon. PLoS One, 2015. 10(12): p. e0144630.
128. Strept(avidin)-biotin complex method for IHC detection. Available from: https://www.thermofisher.com/de/de/home/life-science/protein-biology/protein-biology-learning-center/protein-biology-resource-library/pierce-protein-methods/avidin-biotin-complex-method-ihc-detection.html.
129. Im, K., et al., An introduction to performing immunofluorescence staining. Methods Mol Biol, 2019. 1897: p. 299-311.
130. Bankhead, P., et al., QuPath: Open source software for digital pathology image analysis. Sci Rep, 2017. 7(1): p. 16878.
131. Smith, P.K., et al., Measurement of protein using bicinchoninic acid. Anal Biochem, 1985. 150(1): p. 76-85.
132. Schindelin, J., et al., Fiji: an open-source platform for biological-image analysis. Nat Methods, 2012. 9(7): p. 676-82.
133. Parthasarathy, G., X. Revelo, and H. Malhi, Pathogenesis of nonalcoholic steatohepatitis: an overview. Hepatol Commun, 2020. 4(4): p. 478-492.
134. Wojcik-Cichy, K., E. Koslinska-Berkan, and A. Piekarska, The influence of NAFLD on the risk of atherosclerosis and cardiovascular diseases. Clin Exp Hepatol, 2018. 4(1): p. 1-6.
135. Plump, A.S., et al., Severe hypercholesterolemia and atherosclerosis in apolipoprotein E-deficient mice created by homologous recombination in ES cells. Cell, 1992. 71(2): p. 343-53.
136. Nakashima, Y., et al., ApoE-deficient mice develop lesions of all phases of atherosclerosis throughout the arterial tree. Arterioscler Thromb, 1994. 14(1): p. 133-40.
137. Emini Veseli, B., et al., Animal models of atherosclerosis. Eur J Pharmacol, 2017. 816: p. 3-13.

138. Mahley, R.W., Apolipoprotein E: cholesterol transport protein with expanding role in cell biology. Science, 1988. 240(4852): p. 622-30.
139. Mahley, R.W. and Y. Huang, Apolipoprotein E: from atherosclerosis to Alzheimer's disease and beyond. Curr Opin Lipidol, 1999. 10(3): p. 207-17.
140. Mahley, R.W. and Z.S. Ji, Remnant lipoprotein metabolism: key pathways involving cell-surface heparan sulfate proteoglycans and apolipoprotein E. J Lipid Res, 1999. 40(1): p. 1-16.
141. Poretsky, L., Looking beyond overnutrition for causes of epidemic metabolic disease. Proc Natl Acad Sci U S A, 2012. 109(39): p. 15537-8.
142. Younossi, Z., et al., Global burden of NAFLD and NASH: trends, predictions, risk factors and prevention. Nat Rev Gastroenterol Hepatol, 2018. 15(1): p. 11-20.
143. Godoy-Matos, A.F., W.S. Silva Junior, and C.M. Valerio, NAFLD as a continuum: from obesity to metabolic syndrome and diabetes. Diabetol Metab Syndr, 2020. 12: p. 60.
144. Caldwell, S., et al., Hepatocellular ballooning in NASH. J Hepatol, 2010. 53(4): p. 719-23.
145. Hernandez-Gea, V. and S.L. Friedman, Pathogenesis of liver fibrosis. Annu Rev Pathol, 2011. 6: p. 425-56.
146. Friedman, S.L., Liver fibrosis -- from bench to bedside. J Hepatol, 2003. 38 Suppl 1: p. S38-53.
147. Zisser, A., D.H. Ipsen, and P. Tveden-Nyborg, Hepatic stellate cell activation and inactivation in NASH-fibrosis-roles as putative treatment targets. Biomedicines, 2021. 9(4).
148. Niki, T., et al., Comparison of glial fibrillary acidic protein and desmin staining in normal and CCl4-induced fibrotic rat livers. Hepatology, 1996. 23(6): p. 1538-45.
149. Nouchi, T., et al., Appearance of alpha-smooth-muscle-actin-positive cells in hepatic fibrosis. Liver, 1991. 11(2): p. 100-5.
150. Carpino, G., et al., Alpha-SMA expression in hepatic stellate cells and quantitative analysis of hepatic fibrosis in cirrhosis and in recurrent chronic hepatitis after liver transplantation. Dig Liver Dis, 2005. 37(5): p. 349-56.
151. Akpolat, N., et al., The value of alpha-SMA in the evaluation of hepatic fibrosis severity in hepatitis B infection and cirrhosis development: a histopathological and immunohistochemical study. Histopathology, 2005. 47(3): p. 276-80.
152. Krenkel, O., et al., Single cell RNA sequencing identifies subsets of hepatic stellate cells and myofibroblasts in liver fibrosis. Cells, 2019. 8(5).
153. Wang, H., et al., Single-cell transcriptomic analysis reveals a novel cell state and switching genes during hepatic stellate cell activation in vitro. J Transl Med, 2022. 20(1): p. 53.
154. Segura-Puimedon, M., et al., Proatherosclerotic effect of the alpha1-Subunit of solubleguanylyl cyclase by promoting smooth muscle phenotypic switching. Am J Pathol, 2016. 186(8): p. 2220-2231.
155. Mauersberger, C., et al., Loss of soluble guanylyl cyclase in platelets contributes to atherosclerotic plaque formation and vascular inflammation. Nat Cardiovasc Res, 2022. 1(12): p. 1174-1186.
156. Schaffner, D., et al., Analysis of the nitric oxide-cyclic guanosine monophosphate pathway in experimental liver cirrhosis suggests phosphodiesterase-5 as potential target to treat portal hypertension. World J Gastroenterol, 2018. 24(38): p. 4356-4368.

157. Weiskirchen, S., et al., Isolation and culture of primary murine hepatic stellate cells. Methods Mol Biol, 2017. 1627: p. 165-191.
158. Bartneck, M., et al., Isolation and time lapse microscopy of highly pure hepatic stellate cells. Anal Cell Pathol (Amst), 2015. 2015: p. 417023.
159. van Dijk, F., et al., Design of a Gene Panel to Expose the Versatile Role of Hepatic Stellate Cells in Human Liver Fibrosis. Pharmaceutics, 2020. 12(3).
160. Meurer, S.K., et al., Isolation, purification, and culture of primary murine hepatic stellate cells: an update. Methods Mol Biol, 2023. 2669: p. 1-32.
161. Schuster, S., et al., Triggering and resolution of inflammation in NASH. Nat Rev Gastroenterol Hepatol, 2018. 15(6): p. 349-364.
162. Marais, A.D., Apolipoprotein E in lipoprotein metabolism, health and cardiovascular disease. Pathology, 2019. 51(2): p. 165-176.
163. Getz, G.S. and C.A. Reardon, Apoprotein E as a lipid transport and signaling protein in the blood, liver, and artery wall. J Lipid Res, 2009. 50 Suppl(Suppl): p. S156-61.
164. Cho, E.J., et al., Body weight gain rather than body weight variability associated with increased risk of nonalcoholic fatty liver disease. Sci Rep, 2021. 11(1): p. 14428.
165. Arroyave-Ospina, J.C., et al., Role of oxidative stress in the pathogenesis of non-alcoholic fatty liver disease: implications for prevention and therapy. Antioxidants (Basel), 2021. 10(2).
166. King, V.L., et al., A murine model of obesity with accelerated atherosclerosis. Obesity (Silver Spring), 2010. 18(1): p. 35-41.
167. Liu, J., et al., Free fatty acids, not triglycerides, are associated with non-alcoholic liver injury progression in high fat diet induced obese rats. Lipids Health Dis, 2016. 15: p. 27.
168. Kampschulte, M., et al., Western diet in ApoE-LDLR double-deficient mouse model of atherosclerosis leads to hepatic steatosis, fibrosis, and tumorigenesis. Lab Invest, 2014. 94(11): p. 1273-82.
169. Zhang, Q., et al., A high-trans fat, high-carbohydrate, high-cholesterol, high-cholate diet-induced nonalcoholic steatohepatitis mouse model and its hepatic immune response. Nutr Metab (Lond), 2023. 20(1): p. 28.
170. Simonen, M., et al., Desmosterol in human nonalcoholic steatohepatitis. Hepatology, 2013. 58(3): p. 976-82.
171. Denk, H., C. Stumptner, and K. Zatloukal, Mallory bodies revisited. J Hepatol, 2000. 32(4): p. 689-702.
172. Mannery, Y.O., C.J. McClain, and M.B. Vos, Keratin 18, apoptosis, and liver disease in children. Curr Pediatr Rev, 2011. 7(4): p. 310-315.
173. Jiang, J.X. and N.J. Torok, Liver injury and the activation of the hepatic myofibroblasts. Curr Pathobiol Rep, 2013. 1(3): p. 215-223.
174. Zhang, G., et al., Carbon tetrachloride (CCl(4)) accelerated development of non-alcoholic fatty liver disease (NAFLD)/steatohepatitis (NASH) in MS-NASH mice fed western diet supplemented with fructose (WDF). BMC Gastroenterol, 2020. 20(1): p. 339.
175. Lehners, M., et al., cGMP Signaling and vascular smooth muscle cell plasticity. J Cardiovasc Dev Dis, 2018. 5(2).
176. Brusilovskaya, K., et al., Vascular targets for the treatment of portal hypertension. Semin Liver Dis, 2019. 39(4): p. 483-501.

177. Zhang, Q.D., et al., Myofibroblastic transformation of rat hepatic stellate cells: the role of Notch signaling and epithelial-mesenchymal transition regulation. Eur Rev Med Pharmacol Sci, 2015. 19(21): p. 4130-8.
178. Dang, T.M., et al., Optimization of the isolation procedure and culturing conditions for hepatic stellate cells obtained from mouse. Biosci Rep, 2021. 41(1).
179. Shang, L., et al., Human hepatic stellate cell isolation and characterization. J Gastroenterol, 2018. 53(1): p. 6-17.
180. Kawada, N., et al., Smooth muscle alpha-actin expression in rat hepatic stellate cell is regulated by nitric oxide and cGMP production. Biochem Biophys Res Commun, 1996. 229(1): p. 238-42.
181. Wen, L., et al., A shear-dependent NO-cGMP-cGKI cascade in platelets acts as an auto-regulatory brake of thrombosis. Nat Commun, 2018. 9(1): p. 4301.
182. Per A.Peterson, L.R., Studies on the fluorescence of the human vitamin A-transporting plasma protein complex and its individual components. J Biol Chem, 1971. 246(24): p. 7544-7550.
183. Thompson, J.N., et al., Fluorometric determination of vitamin A in human blood and liver. Biochem Med, 1971. 5(1): p. 67-89.
184. Perri, R.E., et al., Defects in cGMP-PKG pathway contribute to impaired NO-dependent responses in hepatic stellate cells upon activation. Am J Physiol Gastrointest Liver Physiol, 2006. 290(3): p. G535-42.
185. Lee, J.S., et al., Mechanisms of nitric oxide interplay with Rho GTPase family members in modulation of actin membrane dynamics in pericytes and fibroblasts. Am J Pathol, 2005. 166(6): p. 1861-70.
186. Routray, C., et al., Protein kinase G signaling disrupts Rac1-dependent focal adhesion assembly in liver specific pericytes. Am J Physiol Cell Physiol, 2011. 301(1): p. C66-74.
187. Ma, Y., et al., Oxidative stress is a key modulator in the development of nonalcoholic fatty liver disease. Antioxidants (Basel), 2021. 11(1).
188. Jagannathan, L., S. Cuddapah, and M. Costa, Oxidative stress under ambient and physiological oxygen tension in tissue culture. Curr Pharmacol Rep, 2016. 2(2): p. 64-72.
189. Stasch, J.P., et al., NO- and haem-independent activation of soluble guanylyl cyclase: molecular basis and cardiovascular implications of a new pharmacological principle. Br J Pharmacol, 2002. 136(5): p. 773-83.
190. Zhao, Y., et al., Inhibition of soluble guanylate cyclase by ODQ. Biochemistry, 2000. 39(35): p. 10848-54.
191. Trayhurn, P., Endocrine and signalling role of adipose tissue: new perspectives on fat. Acta Physiol Scand, 2005. 184(4): p. 285-93.
192. Hoffmann, L.S., et al., Stimulation of soluble guanylyl cyclase protects against obesity by recruiting brown adipose tissue. Nat Commun, 2015. 6: p. 7235.
193. Lala, V., M. Zubair, and D.A. Minter, Liver Function Tests, in StatPearls. 2024: Treasure Island (FL).
194. Pejnovic, N., et al., Galectin-3 and IL-33/ST2 axis roles and interplay in diet-induced steatohepatitis. World J Gastroenterol, 2016. 22(44): p. 9706-9717.
195. She, S., et al., Functional roles of chemokine receptor CCR2 and its ligands in liver disease. Front Immunol, 2022. 13: p. 812431.

196. Baeck, C., et al., Pharmacological inhibition of the chemokine CCL2 (MCP-1) diminishes liver macrophage infiltration and steatohepatitis in chronic hepatic injury. Gut, 2012. 61(3): p. 416-26.
197. Baeck, C., et al., Pharmacological inhibition of the chemokine C-C motif chemokine ligand 2 (monocyte chemoattractant protein 1) accelerates liver fibrosis regression by suppressing Ly-6C(+) macrophage infiltration in mice. Hepatology, 2014. 59(3): p. 1060-72.

7 Appendix

7.1 Supplementary tables

Supplementary table I: Equipment for HSC isolation.

Equipment	Company
Blood vessel clamp	FST, Lot 1208992A
Hot plate with a stirrer	Neo Lab MR3002
Needle (22 G)	100 Sterican® 0.70 x 30 mm 229 x $1^{1/4''}$, B BRAUN
Petri dishes	Griner BIO-ONE
Perfusion pump	Pharmacia Fine Chemicals
Syringe (3 ml, 20 ml)	B BRAUN

Supplementary table II: Reagents for EGTA solution.

Reagent	Final concentration
NaCl	8000 mg/L
KCl	400 mg/L
$NaH_2PO_4.H_2O$	88.17 mg/L
Na_2HPO_4	120.45 mg/L
HEPES	2380 mg/L
$NaHCO_3$	350 mg/L
EGTA	190 mg/L
D- Glucose	900 mg/L

Supplementary table III: Reagents for enzyme buffer solution.

Reagent	Final concentration
NaCl	8000 mg/L
KCl	400 mg/L
$NaH_2PO_4.H_2O$	88.17 mg/L
Na_2HPO_4	120.45 mg/L
HEPES	2380 mg/L
$NaHCO_3$	350 mg/L
$CaCl_2.2H_2O$	560 mg/L

Supplementary table IV: Reagents for GBSS/A solution.

Reagent	Final concentration
KCl	370 mg/L
$MgCl_2.6H_2O$	210 mg/L
$MgSO_4.7H_2O$	70 mg/L
Na_2HPO_4	59.6 mg/L
KH_2PO_4	30 mg/L
Glucose	991 mg/L
$NaHCO_3$	227 mg/L
$CaCl_2.2H_2O$	225 mg/L

Supplementary table V: Reagents for GBSS/B solution.

Reagent	Final concentration
NaCl	8000 mg/L
KCl	370 mg/L
$MgCl_2.6H_2O$	210 mg/L

$MgSO_4.7H_2O$	70 mg/L
Na_2HPO_4	59.6 mg/L
KH_2PO_4	30 mg/L
Glucose	991 mg/L
$NaHCO_3$	227 mg/L
$CaCl_2.2H_2O$	225 mg/L

Supplementary table VI: Common antibodies and their dilutions. WB: Western blot; IHC: Immunohistochemistry; IF: Immunofluorescence

Antibody	Company	Dilution	Source
α-SMA	ab124964 Abcam	1:500 IF 1:1000 IHC 1:5000 WB	Rabbit
cGKI (DH)	AG Feil	1:500 IF 1:800 IHC 1:5000 WB	Rabbit
Collagen IV	ab6586 Abcam	1:500 IF	Rabbit
Desmin	MA5-33065 Thermo Fisher Scientific	1:1000 IF 1:5000 WB	Rabbit
F4/80	MF48000 Invitrogen	1:200 IF	Rat
GAPDH	2118 Cell Signalling	1:5000 WB	Rabbit
GUCY1B3 (NO-GC)	ab24824 Abcam	1:20 IF 1:200 WB	Rabbit
Mac-2	CI8942 Cedarlane	1:200 IHC 1:6000 WB	Rat
SM22α	ab14106 Abcam	1:500 IF 1:200 IHC 1:1000 WB	Rabbit
α-Desmin Alexa 488	ab185033 Abcam	1:50 IF	Rabbit
Anti α-SMA Cy3	C6198 Sigma-Aldrich	1:50 IF	Mouse
α-rabbit Alexa 488	A11008 Life Technologies	1:500 IF	Goat
α-rabbit Alexa 555	A21428 Life Technologies	1:500 IF	Goat
α-rat Alexa 488			
α-rabbit HRP	70749 Cell Signalling	1:5000 WB	Goat
α-rat HRP	SBA-3030-05 Biozol	1:5000 WB	Goat
α-rabbit biotinylated	BA-1000 Vector Labs	1:200 IHC	Goat
α-rat biotinylated	BA-4001 Vector Labs	1:200 IHC	Rabbit

Supplementary table VII: Antibodies tested but did not work in liver WB, IHC, IF.

Antibody	Company	Dilution	Source	Remarks
CRBP-I	Santa Cruz (not available anymore)	1:200 IF 1:200 IHC	Mouse	No staining
Collagen IV	ab6586 Abcam	1:5000 WB	Rabbit	Unclear bands
Desmin	MA5-33065 Thermo Fisher Scientific	1:500 IHC	Rabbit	No staining
GUCY1B3	ab24824 Abcam	1:20 IHC	Rabbit	No staining
GUCYB1	160897 Cayman	1:200 IHC, WB, IF	Rabbit	No staining
Ki67	ab15580 Abcam	1:500 IF	Rabbit	Unspecific staining
RBPI	ab154881 Abcam	1:500 IF	Rabbit	No staining
RGS5	ab196799 Abcam	1:500 IF 1:500 IHC	Rabbit	No staining

VASP	3132 Cell Signalling	1:1000 WB	Rabbit	No bands
p-VASP Ser239	3114 Cell Signalling	1:1000 WB	Rabbit	No bands

Supplementary table VIII: Cells stained positive for common antibodies. The total number of cells represent the number of nuclei counted. Positive cells represent the cells stained positive for the respective antibodies. The analysis was performed using QuPath.

Mouse group	Antibody	Total number of cells (average of 3 mice/group)	Positive-stained cells (average of 3 mice/group)
ND	Desmin	1694	269
HFD		1624	629
ND	SM22	1522	21
HFD		1151	87
ND	NO-GC	1751	132
HFD		1513	275
ND	cGKI	1582	67
HFD		1576	340
HFD	F4/80	1356	56
HFD+Act		844	40

Supplementary table IX: Plasma LDL and tissue triglyceride and cholesterol values. LDL levels were measured in plasma while, triglyceride and cholesterol levels were measured in liver tissues. The table shows the average levels of LDL, triglyceride and cholesterol in each group. Data are shown as mean ± SEM. LDL: low density lipoprotein.

Parameter	ND males	HFD males	HFD females
Number of mice	**9**	**8**	**15**
LDL (mg/dl)	8 ± 2	231 ± 24	260 ± 8
Triglycerides (mg/100 mg tissue)	1.3 ± 0.1	21 ± 2.7	15 ± 1.5
Cholesterol mg/100 mg tissue)	0.2 ± 0.02	2.5 ± 0.4	2.3 ± 0.2

Supplementary table X: Brand names and the companies they belong to.

Brand name	Company
A.Hartenstein	A.Hartenstein GmbH, Würzburg, Germany
Abcam	Abcam plc, Cambridge, MA, USA
AHF	AHF analysentechnik AG, Tübingen, Germany
Allied Vision	Allied Vision Technologies GmbH, Stadtroda, Germany
Altromin	Altromin Spezialfutter GmbH & Co. KG, Lage, Germany
Avantor	VWR International GmbH, Darmstadt, Germany
Axxora	Enzo Biochem Inc., Farmingdale, NY, USA
B. Braun	B. Braun Melsungen AG, Melsungen, Germany
Bio-Rad	Bio-Rad Laboratories Inc., Hercules, CA, USA
Biologix	Biologix Group Ltd., Jinan, Shandong, China
Biometra	Analytik Jena AG, Jena, Germany
Bioron	Bioron GmbH, Römerberg, Germany
Biozym	Biozym Scientific GmbH, Hessisch Oldendorf, Germany
Canon	Canon Deutschland GmbH, Krefeld, Germany
Cedarlane	Cedarlane, Burlington, ON, Canada
Cell Signalling	Cell Signalling Technology Inc., Danvers, MA, USA
ChemSolute	Th. Geyer GmbH & Co. KG, Renningen, Germany
Chroma	Chroma Technology Corp., Bellow Falls, VT, USA

Dianova	Biozol Dioagnostica Vertrieb GmbH, Eching, Germany
Dow	Dow Europe GmbH, Wiesbaden, Germany
Dunnlab	Dunn Labortechnik GmbH, Asbach, Germany
Entosphinx	Ento sphinx s.r.o., Pardubice, Czech Republic
F.S.T	Fine Scientific Tools Inc., Foster City, CA, USA
Fisher	Thero Fisher Scientifc Inc., Waltham, MA, USA
GE Healthcare	General Electric Corp., Chicago, IL, USA
Genaxxon	Genaxxon biscience GmbH, Ulm, Germany
Gibco	Thermo Fisher Scientific Inc., Waltham, MA, USA
Invirtogen	Thermo Fisher Scientific Inc., Waltham, MA, USA
KNF Neuberger	KNF Neuberger GmbH, Freiburg im Briesgau, Germany
Leica	Leica Biosystems GmbH, Wetzlar, Germany
Life Technologies	Thermo Fisher Scientific Inc., Waltham, MA, USA
Obermeier	Kurt Obermeier GmbH & Co. KG, Bad-Berleburg, Germany
Macherey-Nagel	Macherey-Nagel GmbH & Co. KG, Düren, Germany
Menzel	Thermo Fisher Scientific Inc., Waltham, MA, USA
Merck	Merck KGaA, Darmstadt, Germany
Microm	PHC Holding Corp., Dreieich, Germany
Millipore	Merck KGaA, Darmstadt, Germany
MP Biomedicals	MP Biomedicals LLC, Santa Ana, CA, USA
Nippon Genetics	Nippon Genetics Co. Ltd., Bunkyo-Ku, Tokyo, Japan
Photometrics	Teledyne Photometrics Inc., Tucson, AZ, USA
QImaging	QImaging Corp., Surrey, BC, Canada
Roche	F. Hoffmann-La Roche AG, Basel, Switzerland
Roth	Carl Roth GmbH & Co. KG, Karlsruhe, Germany
Saint-Gobain	Compagnie de Saint-Gobain, Courbevoie, France
Schott	Schott AG, Mainz, Germany
Sigma-Aldrich	Merck KGaA, Darmstadt, Germany
Science Services	Science Services GmbH, München, Germany
Simport	Simport Scientific Inc., Bernard-Pilon Beloeil, QC, Canada
SPOT Imaging	Diagnostic Instruments Inc., Sterling Heights, MI, USA
ssniff	ssniff Spezialdiäten GmbH, Soest, Germany
Thermo	Thermo Fisher Scientific Inc., Waltham, MA, USA
TILL Photonics	TILL Photonics GmbH, Gräfeling, Germany
Tocris	Bio-Techne Corp., Minneapolis, MN, USA
Ushio	Ushio Europe B.V., BD Oude Meer, The Netherlands
Vector Labs	Vector Laboratories Inc., Burlingame, CA, USA
Visitron	Visitron Systems GmbH, Puchheim, Germany
Warner Instruments	Harvard Bioscience Inc., Hamden, CT, USA
Yokogawa	Yokogawa Electric Corp., Musashino, Tokyo, Japan
ZEISS	Carl Zeiss AG, Oberkochen, Germany

7.2 Extended method- QuPath image analysis

QuPath image analysis was adapted from a YouTube tutorial titled ''Introduction to QuPath for Multiplexed Fluorescence Microscopy'' by Bioimage Informatics Facility. QuPath creates the scripting protocol when the tutorial is followed stepwise.

1. Open QuPath and create an empty folder. Import images by dragging them onto QuPath and set image type as fluorescence and click import.
2. To change channel names: Open brightness/contrast -> automate -> show script editor -> file -> open -> SetChannel.groovy -> run for project
3. Adjust background on brightness/contrast window (Keep settings should always be check marked).
4. Open the analysis script via automate -> show script editor -> file -> open. Choose the script for the specific antibody you want to analyse.
5. Under annotations, add class for the marker you are analyzing by right click -> add class -> NO-GC, cGKI...
6. Create thresholder:
    - Classify -> pixel classification -> create thresholder
    - Resolution: Full
    - Channel: select the marker channel you are analyzing (For eg: NO-GC)
    - Prefilter: Gaussian
    - Smoothing sigma: 0-0-5 or 1
    - Threshold: play around between 50 – 100
    - Above threshold: none
    - Region: Everywhere
    - Classifier name: NO-GC cells
    - Click save
7. Copy FOV.json into pixel classifier folder
8. Run commands 1-7 on one image first. Select commands 1-7 -> run -> run selected
9. Object classification: Classify-> object classification -> create single measurement classifier
    - Check mark live preview
    - Object filter: Detections(all)
    - Channel filter: No-GC
    - Measurement: Cell: NO-GC mean
    - Threshold: find the best fit
    - Above threshold: NO-GC +cells
    - Below threshold: none
    - Classifier name: NO-GC
    - Click save and close window
10. Run commands 8-13
11. Once everything works, Run script for the entire project
12. Save project
13. Export measurements: Measure -> export measurements -> Choose folder to save and give a name for the measurement.

- Export type: Annotations
- Separator: comma(.csv)
- Click export

Own publications

Krithika Rajeeth [1] Malte Roessing [1] Peter Sandner [2,3] Anja Schmitt [4] Andreas Peter [5,6,7] Robert Feil [1] and Susanne Feil [1] Activation of NO/cGMP signaling as a potential therapy for metabolic dysfunction-associated steatohepatitis. *In preparation*.

The author has also presented her work in the following conferences:

Rajeeth, K., Rupprecht, M., Feil, R., Feil, S. Investigating the role of NO/cGMP signaling in hepatic stellate cells. CanCaN 2021- GRK2381 PhD Conference.

Rajeeth, K., Roessing, M., Rupprecht, M., Sandner, P., Feil, R., Feil, S. NO/cGMP signaling is a marker for hepatic stellate cells and a therapeutic target for NASH. 6th Global NASH Congress 2023, London

Acknowledgements

First and foremost, I extend my deepest gratitude to Prof. Dr. Robert Feil for providing me with the opportunity to conduct my doctoral thesis in his laboratory. I am equally thankful to Dr. Susanne Feil for being my mentor and supervisor the last four years. I am very grateful to both of you for your compassion, long-lasting support and for shaping my academic career as a scientist. I thank PD Dr. Hannes Schmidt for his guidance on a side project and for the engaging conversations during lunch breaks.

Special thanks to Malte Roessing for the excellent collaboration and for breeding the mice. This project would not have been possible otherwise. Thank you, Dr. Peter Sandner (Bayer) for providing us with the drugs. Many thanks to Miriam Rupprecht for introducing me to cell isolation and some of the basic techniques in the lab. I acknowledge Dr. Anja Schmitt (Universitätsklinikum Münster), Prof. Dr. med. Andreas Peter, Ann Kathrin Horlacher (Universitätsklinikum Tübingen), and Aylin Heinrich (Technician, KSO lab) for the RT-PCR and liver enzyme analysis. For the technical assistance, I thank Barbara Birk. A special thanks to Astrid, Ines, and Jana for being excellent animal care takers.

I deeply appreciate Dr. Moritz Lehners for his invaluable support and guidance during writing my thesis. I thank Dr. Michael Krämer for being my first ever friend in the lab and for helping me improve my slide preparation and presentation skills. To Timo, Daniel, and Shahzad for being wonderful companions on this incredible journey. I am immensely grateful to the three of you for your kindness, support and all the fun memories in Tübingen. I am happy to have made some new friendships with Dr. Nisha Mohd Rafiq, Kristian, and Dr. med. Julian Jedl towards the end of my PhD time in the lab. I thank Morgan Hess for my first ever adventurous hike which marked the beginning of a beautiful friendship.

To my dearest friends Nidhi, Sharat, and Preethi, thank you for the unconditional love and support through every phase of my life. To both of my grandfathers for being a great source of inspiration and for encouraging me to pursue my dreams. I will be ever grateful to amma, nanna, Satya, and Yuka for being the pillars of strength in my life. Finally, thank you God for this blessed life.

Declaration of contributions

This work was written entirely by the author. The use of artificial intelligence (e.g., ChatGPT) was limited to grammatical assistance and proofreading some paragraphs of the thesis. The experiments and results presented here were planned, executed, and analysed by the author with the following exceptions:

- The NO-GC activator was provided by Bayer.
- Breeding of NASH and NO-GC activator treated mice was carried out by Malte Roessing.
- Analysis of liver tissue and plasma samples from control, NASH, and activator treated animals were performed by Ann Kathrin Horlacher from the laboratory of Prof. Dr. med. Andreas Peter at the Zentrallabor des Universitätsklinikums Tübingen.
- RT-PCR analysis of inflammatory cytokines in control, NASH, and activator treated animals was performed by Dr. Anja Schmitt from the group of Prof. Dr. Stephan Hailfinger at the Universitätsklinikum Münster.